FEEDBACK CONTROL OF PLANAR MECHANISMS WITH STRUCTURALLY-FLEXIBLE LINKS: THEORY AND EXPERIMENTS

Kyung-Sang Cho

B.Eng. (Sung Kyun Kwan University), 1988

M.Eng. (McGill University), 1991

Department of Mechanical Engineering

McGill University

Montreal, Quebec, Canada

A thesis submitted to the Faculty of Graduate Studies and Research

in partial fulfilment of the requirements for the degree of

Doctor of Philosophy

September 1995

ISBN 0-612-08086-2

McGill

Memorandum

Roman page i does not exist. The thesis starts from page ii after the cover.

Contents

List of Figures

List of Tables

Abstract

The motion control of mechanical systems with flexible links is investigated. Issues addressed are the modelling and simulation of such systems, the design of a feedback control scheme and its implementation on an actual system. The modelling method used is a combination of a spline-based spatial discretization technique, which allows a definition of the state-variable vector as the set of curvature values at the supporting points of the spline and their time-rates of change, and the natural orthogonal complement of the kinematic constraints that eliminates the constraint forces and moments from the mathematical model. The control algorithm consists of two parts, namely, the decoupling of nonlinear equations of motion and the filtering of non-working constraint forces. The former is achieved using the unconstrained equations of motion, expressed in terms of extended generalized coordinates with which the motion of each separate link is defined. The latter is accomplished using the fact that the constraint forces thus introduced indeed lie in the nullspace of the transpose of the NOC. This control scheme is implemented on a prototype four-bar flexible mechanism. Strain gauges are used to measure link curvature at the supporting points of the spline, while the time-rate of change of curvature is estimated with a Kalman filter. Moreover, the angle of rotation of the input link and its time-rate of change are measured and then used to infer the rest of the rigid-body motions. Results show that the proposed control scheme provides successful trajectory tracking while suppressing the vibration triggered by a doublet-type of disturbance. This disturbance is induced by the singularities of the mechanism coupled with the rapid inertia changes. While the main

motivation of this study is the control of robotic manipulators with long and slender links, typically found in space applications, the results presented are applicable to the control of a much broader class of mechanical systems such as high-speed machinery at large.

Résumé

La présente thèse a pour sujet l'étude de la commande du mouvement des systèmes mécanique à maillons flexibles. Plus spécifiquement, nous abordons les problèmes de modélisation et simulation de ces systèmes, la conception d'une commande par asservissement et son application aux systèmes physiques. La méthode de modélisation utilisée est une combinaison d'une technique de discrétisation spatiale à l'aide de fonctions spline, ce qui permet une définition du vecteur des variables d'état en tant que valeurs de courbure aux points d'appui de la spline ainsi que leurs dérivées temporaires, et le complément orthogonal naturel des contraintes cinématiques, qui élimine les forces et les couples de contrainte du modèle mathématique. L'algorithme de commande se compose de deux parties, soit le découplage des équations non-linéaires de mouvement et le filtrage des forces de contraintes inactives. Le premier est obtenu en se servant des équations de mouvement non-contraint comme coordonnées généralisées avec lesquelles le mouvement de chaque maillon est défini. Le second est réalisé en utilisant le fait que les forces de contrainte ainsi introduites se trouvent dans le noyau de la matrice transposée dudit complément orthogonal. Cette stratégie de commande est implantée dans un prototype de mécanisme flexible à quatre barres. Des jauges extensométriques sont utilisés pour mesurer la courbure du maillon aux points d'appui de la spline, tandis que l'estimation de la dérivée temporaire de la courbure est obtenue à l'aide d'un filtre de Kalman. En outre, l'angle de rotation du maillon d'entraînement et sa vitesse angulaire sont mesurés et servent ensuite pour estimer les variables restantes des mouvements de corps rigide. Les résultats démontrent que

la stratégie de commande proposée permet un dépistage de trajectoire fructueux tout en supprimant la vibration provoquée par une perturbation de type doublet. Cette perturbation est produite par les singularités du mécanisme couplées aux changements rapides d'inertie. Bien que le but principal de la recherche soit la commande de robots manipulateurs à maillons longs et minces, un cas typique en application spatiale, les résultats peuvent s'appliquer à la commande d'une plus grande catégorie de systèmes mécaniques, tels que les machines à haute vitesse en général.

Claim of Originality

The author claims the originality of the basic ideas and research results presented in this thesis, the following being the most significant:

1. Robustness analysis of linear-quadratic-Gaussian (LQG) compensators designed with two different spatial discretization methods, i.e., the normal-mode and the cubic spline methods, in terms of the observation spillover due to estimation errors and the control spillover due to modelling errors.

2. Integration of the two techniques to obtain the governing equations for a planar mechanism with a chain of flexible elements, namely, the natural orthogonal complement (NOC) coupled with Lagrange's equations and the cubic-spline discretization of the flexible elements, modelled as linearly elastic beams.

3. Use of the NOC to filter out the nonworking constraint forces while producing the applied torques, and the design of a linear-quadratic Gaussian compensator based on the unconstrained equations of motion with which the motion of each separate link is defined.

4. Quantitative measure of the allowable bound in nonlinear perturbations to assess the robustness of the discrete-time LQ state feedback using two different discrete representations, i.e., the shift and the Euler operators.

These contributions have been partly reported in a preliminary form in (Cho, Angeles and Hori 1991) and (Cho, Angeles and Hori 1994).

Acknowledgements

I would like to thank Professors Jorge Angeles and Noriyuki Hori for their excellent guidance, encouragement and support during this work. I owe them my deepest gratitude for their invaluable suggestions and advice, which led to clarifying many obscure ideas.

I would like to thank my colleagues and friends in the Department of Mechanical Engineering and in the McGill Centre for Intelligent Machines, especially Farzam Ranjbaran, Ferhan Bulca, Kourosh Etemadi Zanganeh and Robert Lucyshyn, for their many years of generous help and advice concerning the subject of this research work. Special thanks are due to John Darcovich and Brian Roy who have given much constructive criticism on the draft of this thesis. I also wish to thank Iréne Cartier who translated the abstract into French. Finally, I wish to extend my appreciation and thanks to Karim Shafik, George Dedic and George Tewfik, who helped and contributed in completing the experimental component of this work.

I am most grateful to my wife, who has given me her precious support and encouragement without which this work would have not been possible. I am also deeply indebted to my grandfather for his spiritual support throughout my life.

Finally, I would like to acknowledge the financial support from NSERC (Natural Sciences and Engineering Research Council of Canada) and IRIS (Institute for Robotics and Intelligent Systems, a network of Canadian centres of excellence).

Chapter 1

Introduction

1.1 Definition of the Flexible-Body System

In dealing with a mechanical system consisting of bodies, springs and dashpots, a certain classification of the system is needed, depending on the purposes and design consideration of the problem at hand. Such classifications will greatly simplify the problem and reduce efforts in forming the governing equations. For example, a massless spring and a dashpot and mass without compliance are common expressions in engineering terminology as far as a *rigid-body* system is concerned. In the rigid-body system, the small deformations associated with body flexibility are ignored so that the distance between any two of its particles remains constant for all time and for all configurations (D'Souza and Garg, 1984).

While all mechanical systems are intended to be as rigid as possible in order to achieve the required order of precision, however, such a property is not conceivable when it conflicts with other design considerations such as cost and weight. For example, weight takes a first priority in designing a robotic manipulator that finds its application in space to perform such specialized tasks as space-structure construction and satellite manoeuvring. Apart from the fact that the use of heavy and bulky conventional robots requires a high driving power, the cost required to put extra weight in orbit is tremendous. The use of lightweight robotic manipulators seems to be conclusive due to the advantages they offer, i.e., higher speed performance, higher payload-to-weight ratio, smaller actuators and lower energy consumption, as long as the performance of the corresponding rigid-body robot can be achieved.

On the other hand, a demand for faster and more precise mechanical systems has arisen as higher productivity becomes crucial in contemporary industry. However, the higher operating speeds inevitably bring forth the rapid change of inertial forces, thereby resulting in considerable deformations in the structural members, along with non-negligible vibrations. As a common solution, to increase the operating speeds while reducing the inertial forces, lightweight materials are preferred in building the structural members of the said mechanical system. This may, however, worsen the oscillatory behaviour to the point that the rigid-body model is no longer valid.

The structural members of the lightweight robotic manipulator and mechanical system at large undergo considerable link deflection, thereby inducing vibration. The former is due to the lack of stiffness, while the latter is due to the lack of structural damping. The vibration thus introduced would cause disastrous results in connection with a conventional control scheme based on the corresponding rigid-body model. It is, therefore, necessary to introduce another classification to cooperate with a system that undergoes elastic deformation. Under this classification, every material portion of the system may possess both mass and elasticity in contrast to the rigid-body system (Meirovithch, 1967). Hence, distributions of the inertia and stiffness are common. Such a system is herewith termed a *flexible-body* system.

1.2 Background and Literature Survey

1.2.1 Spatial Discretization of Continuous Systems

Incorporating the bending vibration of a continuous beam into the equations of motion requires the integration of a partial differential equation (PDE) that satisfies boundary conditions. The PDE is constructed using the Euler-Bernoulli beam theory, which is valid under the following conditions (Timoshenko 1955):

- the beam undergoes small deformation of less than 10% of its length, and does not suffer from axial extension
- the cross-sectional dimensions are small compared with the length of the beam, i.e., the thickness-to-length ratio of the beam is less than ten
- the rotary inertia effects and shear deformation can be neglected.

These conditions establish a relationship between bending moment and bending deformation, so that the kinetic and potential energies for the given structure can be uniquely determined. Applying the extended Hamilton principle gives rise to the PDE and all the necessary boundary conditions. The integral of the PDE is separable in time and space, so that the displacement function $u(x,t)$ along the beam can be expressed as

$$u(x,t) = Y(x)q(t) \tag{1.1}$$

where $Y(x)$ is a function of the spatial variable, while $q(t)$ is a function of time. This representation converts the PDE into two ordinary differential equations in space and time domains, respectively. The nontrivial solutions satisfying the fourth-order ordinary differential equation in the spatial domain are called the *eigenfunctions* or *natural modes*. These solutions can be used as basis functions to determine the elastic displacement at all points in the structure.

Due to the intrinsic nature of the distributed-parameter system, there are infinitely many nontrivial eigenfunctions. Consequently, a large number of the generalized coordinates are required to represent the elastic deformation along the beam. In theory, the elastic displacement function lies in the space that is spanned by an infinite number of modes (Hughes, 1987). Such displacement functions are often referred to as the exact solution for the given PDE. It is noteworthy that the said space is hypothetical, and thus, may not exist in practice. If a finite number of modes were chosen, how many modes would be necessary to describe the vibrational behaviour of the beam with sufficient fidelity? To answer this question, we may need an engineering compromise between the required accuracy and the practical standpoint. Furthermore, determining these eigenfunctions becomes considerably complicated by the boundary conditions and particular configuration of the continuous body (Meirovitch, 1967).

Such difficulties can be avoided using an approximated solution of the PDE; however, the approximated solution 1) must be given in finite-dimensional form, while assuring the required accuracy; and 2) must be assessable through a physically meaningful quantity such as strain. The first condition allows an accurate yet computationally manageable solution. Computational efficiency is critical for the approximation to be implemented in real-time. The second condition becomes more relevant when the said approximations are linked directly to the feedback control scheme. A fast and precise measurement of such a quantity ensures that the controller has accurate information on the system behaviour.

Previous approaches to modelling of the structural member of flexible manipulators can be classified into the following two groups.

Normal-Mode Approach

The first approach is the normal-mode analysis, which determines the solution of the PDE in the form of a finite sum composed of a linear combination of eigenfunctions, which satisfy all the boundary conditions and the differential equation of the underlying eigenvalue problem, multiplied by time-dependent generalized coordinates (Book and Majette, 1983; Cannon and Schmitz, 1984; Sakawa, Matsuno and Fukushima, 1987). This approach treats a continuous system as a finite-dimensional system by eliminating higher modes. Moreover, coupling terms between each mode in forming equations of motion must vanish and diagonal terms become unity due to the generalized orthogonality and normality conditions (Meirovitch, 1967), respectively, that are imposed on these eigenfunctions. This will reduce substantially the required computational effort.

Despite its computational efficiency, this method has certain limitations. First, obtaining eigenfunctions can be difficult in practice. Cases for which exact solutions have been found generally relate to uniform systems with relatively simple boundary conditions. Second, the measure of certain state variables (particularly, the end-point transverse displacement and its first time-rate of change associated with bending vibration) often requires the use of a vision system (Chen and Zheng, 1992) which, although suitable for end point-tracking control, is too slow for the transverse-vibration control of the entire beam.

Finite Elements Method

The second approach is the finite element method (Bahgat and Willmert, 1976; Bayo, 1987; Giovagnoni and Rossi, 1989), which discretizes the continuous system into a finite set of elements on which the displacement field is assumed to take on a simple form, usually a multivariate polynomial of a low degree (up to three). It divides complicated structures into small elements, so that each of the elements can be analyzed and numerical data of the required accuracy can be extracted with relative ease. This method allows the modelling of links that have nonhomogeneous material properties, nonuniform cross-sections, and a variety of boundary conditions. However, the use of finite element methods generally requires a large system of ordinary differential equations to model the system with sufficient fidelity, and thus may not be suitable for real-time closed-loop control.

Cubic Splines

In an effort to accommodate the real-time control requirement, cubic splines are employed as trial functions to approximate the elastica of the continuous beam at a given set of supporting points (Dancose, Angeles and Hori, 1989). Although cubic splines can be regarded as a special class of finite elements, the proposed approach possesses certain properties that distinguish it from the finite element method, namely,

- This approach provides an exact interpolation of the original physical data—measured at the supporting points—by a cubic spline passing through the supporting points, whereby the displacement field is given as a polynomial of low degree.
- The first-derivative continuity condition of cubic splines eliminates the need of considering additional coordinates such as slopes at the supporting points. This, in turn, reduces the computational burden significantly.
- The cubic-spline spatial discretization gives rise to a linear relationship between displacement and curvature values at the supporting points. This relationship allows the displacement function to be inferred from the set of curvature values at the supporting points of the spline. It is noteworthy that these curvatures can be directly measured from fast and accurate strain gauges, whereas the measurement of displacement along the beam requires a computationally-expensive vision system.

Considering that the selection of a sampling rate plays a key role in the successful digital control of a system possessing multi-rate resonances, the use of cubic splines can provide more flexibility in designing the control system and thus make the real-time control more practical.

In summary, cubic splines consist of piecewise cubic polynomials between every two supporting points, where not only the displacement and the slopes, but also the second derivative is *continuous* (Strang, 1986). Cubic splines allow direct measurements through strain gauges. Hence, beam deformation is not assumed, but measured at the supporting points and then interpolated using cubic splines with time-varying coefficients.

1.2.2 Dynamics Formulation with the NOC

In the dynamic analysis of a mechanical system with chains of flexible elements, the mutual dependence between rigid-body motion and elastic motion has received a great amount of attention. This dependence becomes an essential criterion in classifying most previous works done to date (Bayo and Serna, 1989; Nagarajan and Turcic, 1990), which is due to the growing demand for increased operating speed. The higher the operating speeds required, the larger the inertial forces induced. In addition, the rapid change of inertial forces produces impact-type loadings, so that structural members undergo a substantial amount of link deflections. Hence, link deflections are attributed to both rigid and elastic motions. In this context, neglecting those coupling terms between the former and the latter, and separating the rigid-body motion from the elastic motion—the rigid-body motion is defined as a nominal motion and then used as an input to synthesize the resulting elastic deformations (Sadler and Sandor, 1973; Midha, Erdman and Frohrib, 1977)—would give rise to erroneous results. As was verified experimentally by Turcic and Midha (1984), the assumption made on the independence of the rigid-body and the elastic motions is only valid for a certain class of system such as an elastic four-bar crank-rocker mechanism with a large flywheel at the crank. The large inertia thus created by locating the flywheel at the crank reduces the variation of inertial forces in such a way that the mechanism considered can achieve its force balance. This force balancing eliminates rapid inertia changes that often cause impact loadings. The flywheel is thus used to prevent exciting the elastic motion so that the rigid motion is maintained independent of the elastic motion. It must, however, be taken into account that impact loadings are developed by not only the higher operating speed, but also the intrinsic singularities of the mechanisms at hand. These singularities often introduce substantial link deflections, and thus make the aforementioned assumption on the independence of the rigid-body motion and the elastic motion difficult to accept.

It is of practical importance to consider that the nominal motion must account for the rigid-body motion and the elastic motion as well. This becomes apparent when the feedback control is used to suppress link oscillations while attaining its desired rigid-body motion. The corrective measure provided by the aforementioned controller takes into account both the rigid-body and elastic motions. Moreover, the coupling terms between the two motions must be considered in the kinematic and dynamic formulations. The coupling terms are a kind of messenger that transmits external forces into the internal system so that its internal behaviour comes into effect. Without considering these factors, it is very difficult to secure the proper dynamic responses. A comprehensive discussion on this topic can be found (Naganathan and Soni, 1987).

Even if the nominal motion is properly defined so that the mutual dependence between the rigid body and the elastic motion is taken into consideration, the task of incorporating the constraints due to kinematic loops becomes more challenging in the dynamic analysis of the mechanism at hand. Most studies undertaken to date use Lagrange multipliers to incorporate these constraints into the equations of motion. First, the equations of motions are developed by employing the maximal set of the generalized coordinates to locate and orient bodies in space. The constraints due to the coupling of each intermediate link with its neighbours and the loop closures are then imposed to represent the kinematics of the system. This approach yields a system of nonlinear differential equations, as well as algebraic equations (Song and Haug, 1980; Shabana and Wehage, 1983). In contrast to the concise and systematic formulation thus provided, the solution of the mixed set of differential and algebraic equations is not trivial and even far more complex than the integration of the differential equations alone. In addition, the number of equations to be solved is larger than actually needed. This is so because a number of dependent generalized coordinated is employed in the dynamic formulation.

It is, therefore, desirable to find the equations of motion with the minimum number of generalized coordinates, while considering the constraints within the model. Along these lines, the penalty method is worth mentioning. In this method, the constraints are directly inserted into Lagrange's formulation instead of adjoining them with the aid of Lagrange multipliers. This can be achieved by introducing fictitious penalty functions. These functions are then penalized by increasing weighting factors to force the verification of the constraints within a prescribed tolerance. This method has certain drawbacks: 1) the insertion of the constraints into Lagrange's formulation only holds if the weighting factors approach infinity, and thus, bring forth the problem of choosing the right penalty factors; 2) although large weighting factors guarantee the convergence to the constraint, they may lead to numerical ill-conditioning and develop very large roundoff errors (Bayo and Serna, 1989); 3) a moderate choice of the weighting factors requires an iteration process, which in turn increases the computational burden.

In this thesis, the spatial discretization technique based on cubic splines is incorporated into a methodology consisting of the use of the natural orthogonal complement of kinematic constraints (Angeles and Lee, 1988), that eliminates the constraint forces and moments from the mathematical model. With the foregoing approach, the coupling between the rigid-body and the elastic motions is fully considered in the equations of motion. Moreover, the governing equations thus derived can be expressed in terms of a minimal set of generalized coordinates, while taking into account the constraints arising from the couplings between consecutive links and the loop closures. The constraint forces thus introduced are effectively eliminated by virtue of the natural orthogonal complement (NOC), obtained from a suitable kinematic formulation of the linear velocity constraints.

A number of approaches to obtaining the orthogonal complement of the kinematic constraints have been proposed for a multibody system, which leads to an elimination of the said constraint forces and moments. For example, a singular-value decomposition method is used to extract independent generalized coordinates from the dependent ones, while producing the said orthogonal complement (Singh and Likins, 1985). In the same vein, the orthogonal complement is obtained on the basis of successive multiplications of Householder transformations, while exploiting its enhanced numerical properties (Amirouche, Jia and Ider, 1988; Ider and Amirouche, 1988). In the present study, the orthogonal complement matrix is extracted from the reciprocity relations between the independent generalized speeds and the constraint forces (Angeles and Lee, 1988; Cyril, Angeles and Misra, 1991; Darcovich, Angeles and Misra, 1992). With this approach, the solution of differential and algebraic equations is not needed, in contrast with the dynamic formulation using Lagrange multipliers. Neither is the cumbersome penalty function required.

1.2.3 Robustness Issues

The objective of the control scheme is to suppress the vibration and bending of all the bodies of the system, while attempting to produce the required rigid-body motion of one of the elements, e.g., the end-effector in a robotic manipulator. To attain this goal, precise information concerning link deflection is needed so that the controller can determine the source of link oscillation. However, this measurement results in a noncollocated control problem; i.e., the sensors and actuators are placed at different locations on the flexible structure. This introduces unstable zeros, which impose an upper limit on the bandwidth that can be achieved and increase the overall sensitivity to disturbances in the passband of the system. Hence, the presence of unstable zeros turns out to be a fundamental limitation induced by the system characteristics on the performance of the controller.

It has been reported that an accurate model is essential to successful noncollocated control due to the limited bandwidth capabilities of noncollocated controllers (Cannon and Schmitz, 1984). However, the mathematical model is only an approximation of a nonlinear and infinite-dimensional system, so that the accuracy of the model required to accommodate noncollocated sensing is often questionable. Considering that unstable zeros are imposed by the system characteristics, a model that reduces the effects of noncollocated sensing has to be sought without sacrificing accuracy.

In dealing with distributed-parameter systems, it is common engineering practice to assume that the first few modes are dominant and the higher modes are taken care of by the structural damping of the system itself. The infinite-dimensional system is then controlled by a finite-dimensional compensator.

It has been pointed out that the unmodelled higher modes may reduce the stability margin of the closed-loop system, and thus cause instability associated with the linear-quadratic-Gaussian compensator design (Gibson and Adamian, 1991). This is, in fact, the well-known spillover effect (Balas, 1982). Since the controller and observer gains lie predominantly within the span of the finite number of modes to be considered, the unmodelled higher modes are practically orthogonal to these gains, and thus, the LQG compensator mostly ignores them. The high-frequency residual vibrations are thus fed back to the control system by noise-sensitive sensors. Therefore, the model must be such that the controller designed based on it is robust to those unmodelled higher modes that may contain a wide range of frequency spectrum.

Previous studies in the literature have focused on the modelling and control of a rather simple structure, such as a rotating flexible beam. Moreover, they do not always take the effect of noncollocated sensing and robustness to unmodelled higher-order dynamics into account. However, the growing demand to expand the existing modelling and control methodologies to more complex systems having several structurally flexible links requires a control scheme that is robust against variations in their open-loop dynamics. Furthermore, this control scheme must provide an improved signal-to-noise ratio, thereby enhancing the capability of the controller against the chronic spillover effects associated with the noncollocated sensing.

One way of seeking for the desired robustness is to synthesize the controller while simplifying the dynamics of the system model as much as possible. It is rather traditional for a control engineer to seek the achievable bandwidth in which the said controller is not sensitive to the system dynamics. In this approach, the neglected higher-order dynamics is not a concern as long as the controller does not excite the high-frequency modes, i.e., the closed-loop bandwidth is chosen to be sufficiently low. Therefore, the model is simplified at the expense of a low achievable bandwidth.

Another way is to find a model that allows a design of the robust control scheme, while considering the higher-order dynamics as much as required. In this case, the controller can be designed using one of the many methods available. Since the dynamics of the system impose an upper limit on the obtainable bandwidth, inclusion of higher-order dynamics in the model would increase the achievable closed-loop bandwidth.

The latter approach is taken to assess the robustness of linear-quadratic-Gaussian (LQG) compensators designed with two different spatial discretization methods, in terms of the observation spillover due to estimation errors and the control spillover due to modelling errors. The two discretization methods used are the normal-mode and the cubic-spline methods. In order to investigate observation spillover effects, the sensitivity function of the LQG compensator is introduced. Moreover, the quantitative measure of the robustness of the LQ state feedback is used to provide tolerable levels of control spillover, so that the closed-loop system remains stable. An analysis based on Nyquist plots shows a substantial improvement in robustness using cubic splines over normal modes.

1.2.4 Design and Implementation of Control Schemes

Design of a Nonlinear Controller

The governing equations for the planar four-bar linkage with structurally flexible elements are, in general, highly coupled and nonlinear. Moreover, the mechanism is often subject to rapid changes of environment and so are its variables, such as the joint angles and their time-rates of change. Furthermore, such a mechanism may possess kinematic singularities, also known as *dead points*. These singularities are intrinsic and thus unavoidable if the mechanism undergoes its full motion cycle.

The control objective is to suppress the vibration of the flexible elements and to attain asymptotic trajectory tracking at all times. In addition, the controller thus employed must ensure the boundedness of all internal signals so that the closed-loop control system provides global convergence for all desired trajectories. The control scheme that achieves such objectives is difficult to obtain due to the nonlinear characteristics of the mechanism, compounded by the rapid parameter variation and existence of singularities. Therefore, a controller based on an approximate model is not expected to work well.

For example, it is well known that gain scheduling may not guarantee global convergence, unless the following two facts are secured: 1) the scheduling parameter should capture the nonlinearities of the plant; and 2) the scheduling parameter should vary slowly (Shamma and Athans, 1992). Since the gain scheduling is based on a collection of linear time-invariant approximations to a nonlinear plant at fixed operating points, a reliable control performance is expected for the fixed operating condition from which the gain is taken. Hence, the rapid parameter variation throughout the range of operating conditions may significantly deteriorate the overall performance of the control system. However, gain scheduling becomes a reliable alternative if the rigidity of the system can be compromised in such a way that a little link flexibility is allowed. In other words, tolerating a little link flexibility gives rise to better tradeoff in the rigid-body motion control, such as position and orientation control of the end-effectors (Carusone and D'Eleuterio, 1993; Carusone and D'Eleuterio, 1993).

A computed-torque approach is a good candidate to deal with such difficulties and to achieve the control objectives. The computed-torque method is a model-based control algorithm relying on the inverse dynamics of the system. The inverse dynamics is then used for feedback linearization of a nonlinear system provided that the parameters needed for control are known. The latter is seldom the case because the dynamic model is at most a reflection of a nonlinear plant onto the mathematically realizable subspace, which often turns out to be too abstract. To bridge this discrepancy, various adaptive routines have been added to the framework of the computed-torque approach (Craig, Hsu and Sastry, 1986; Spong and Ortega, 1988; Middleton and Goodwin, 1988).

Adaptive schemes have been evolving in such a way that less and less restrictions are necessary in implementing the computed-torque method. However, the transient performance of these control algorithms depends heavily on the initial condition of a system and is not yet fully practical. Moreover, since the asymptotic stability has not been proven to be uniform, a small change in the dynamics may result in loss of stability (Ortega and Spong, 1989).

The state of the art of the computed-torque approach, which is used in the control of robotic manipulators, is still based on the assumption that all joint variables are available. This assumption may be sufficient for the motion control of rigid-body robotic manipulators, although the experimental verification of such cases is seldom found in the open literature to date. This assumption may not allow the direct application of the computed-torque approach for the control of the mechanism with a chain of structurally flexible elements. Not only joint variables but also information on the link deformation is needed for the successful control of a flexible mechanism. However, some of the variables associated with the link deformation may not be available through direct measurement.

A nonlinear control scheme proposed in this thesis estimates the variables not available from the measured output, while taking care of the associated nonlinearities in the control scheme. The basic framework is similar to the computed-torque approach in the sense that feedback linearization is used (Fig. 1.1). The proposed controller consists of two blocks: the inner loop block is a nonlinear state feedback control law and the outer loop is typically a linear compensator driven by the tracking error between the estimated and the nominal states (Fig. 1.2). To obtain the estimated state, a Kalman filter based on the dynamic model is used.

The key idea lies in the fact that the dynamic formulation based on the NOC

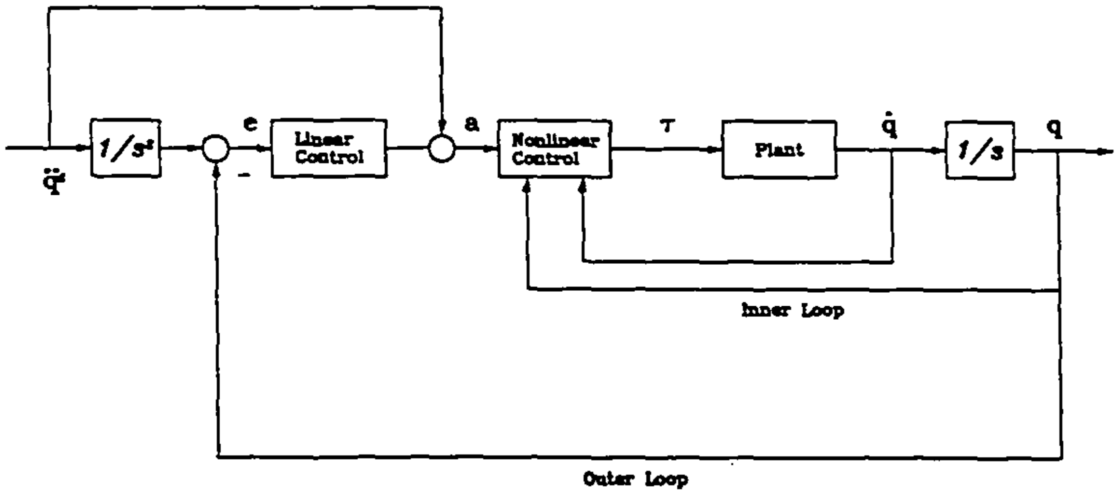

Figure 1.1: A general structure of the computed-torque approach in nonlinear control form

provides the decoupled and coupled equations of motion simultaneously. The former is constructed in terms of the extended generalized speeds, while the latter is expressed in terms of the independent generalized speeds. The connection between these two equations of motion can be obtained as a form of the NOC.

The Kalman filter can then be obtained by using the linearized decoupled equations of motion. It should be realized that the nonlinear terms in the decoupled equations of motion are not associated with rigid-body coordinates but rather with the link deflections, namely, flexible coordinates. Moreover, the coupling terms are not neglected in the foregoing equations of motion. Hence, the admissible control law can also be constructed based on the linearized decoupled equations of motion. This linear compensator constitutes the outer loop (Fig. 1.2). However, the use of the decoupled equations of motion gives rise to the control inputs in terms of the extended generalized forces that contain nonworking constraint forces, instead of the applied torque. When the nonworking constraint forces are eliminated by virtue of the NOC, the applied torque can be obtained by filtering the generalized forces through the NOC. Since the NOC is configuration-dependent, the inner loop is required for the NOC to assess those state variables and used as a nonlinear state feedback (Fig. 1.2).

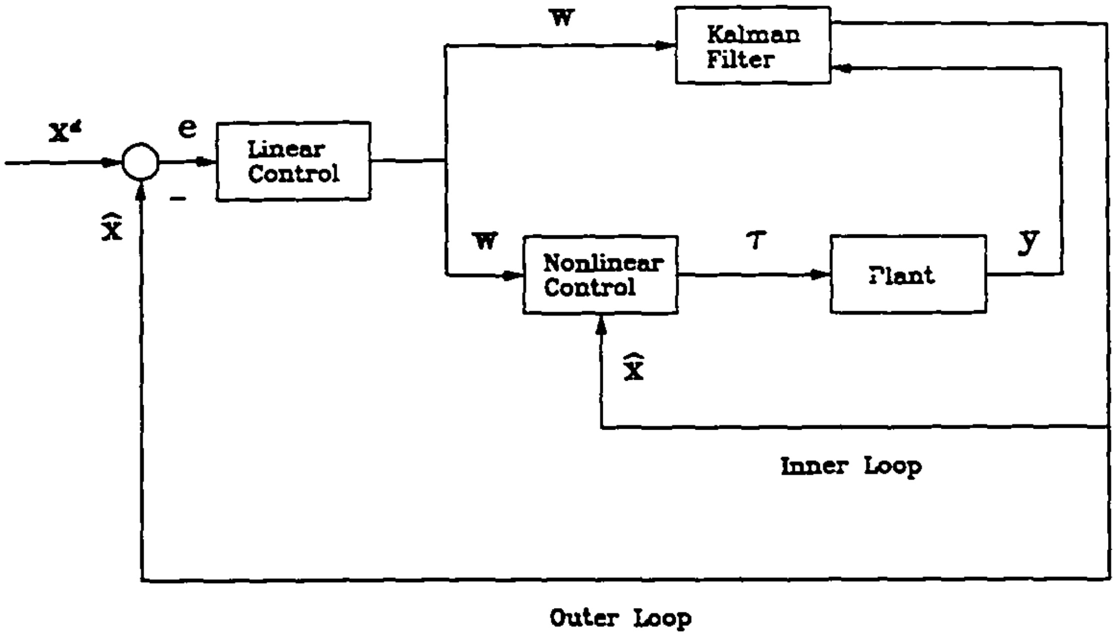

Figure 1.2: A proposed nonlinear control algorithm

This model-based control algorithm can be implemented safely on industrial robots, where each joint is controlled individually. Moreover, it avoids the use of computationally expensive adaptive control schemes as well as cumbersome gain-scheduling techniques that are usually needed for the control of such highly nonlinear systems.

Implementation of the Control Scheme Using the Euler Operator

If the proposed control algorithm is implemented on a digital computer, the NOC has to be updated quickly enough so that discretization effects do not degrade its performance relative to the ideal continuous-time case. This is true if the NOC filter can be executed with no computational delay. Moreover, a rapid sampling may tend to increase observation spillover by feeding back the control signal biased by high-frequency residual vibrations, even when an approximate finite-dimensional model is used in the digital control but based on the *shift operator* (Balas, 1982). This is contrary to the commonly made assumption that a higher sampling rate allows the continuous-time system to be better approximated by the discrete-time system.

In this thesis, the *Euler operator* is used for a discrete representation of the proposed control scheme and its computation. The numerical superiority over the usual shift operator of digital control laws using the Euler operator has been examined extensively (Li and Gevers, 1993; Comeau and Hori, 1992; Middleton and Goodwin, 1986). These studies show that the Euler operator formulation offers better finite-word-length coefficient representation and less finite-word length rounding error performance in many cases. Moreover, the use of the Euler-operator formulation provides a close correspondence between continuous- and discrete-time results (Hori, Nikiforuk and Kanai, 1989; Middleton and Goodwin, 1990). Unlike the shift operator, the discrete-time theory based on the Euler operator converges to the appropriate continuous-time results as the sampling rate increases. Such connections provide more flexibility in specifying performance requirements, thereby allowing the digital controllers to be evaluated in a continuous-time context.

Robustness Analysis of the Digital Control Laws

The discrete realization of a continuous-time system is often subject to parameter variations due to finite-word-length effects. Such variations are often very large and therefore deteriorate the stabilizing property obtainable with the continuous-time LQ state feedback. This phenomenon becomes more worrisome when the system to be controlled possesses multiple, high-frequency resonances. It is well known that high-frequency resonances in the plant may cause unacceptable sensitivities to disturbances in conjunction with the discretization (Franklin, Powell and Workman 1990). Hence, it is important to examine the robustness of the discrete LQ state feedback in the presence of system uncertainty.

In this regard, an allowable bound in nonlinear perturbations for continuous-time LQ state feedback is extended to the discrete-time LQ state feedback case for easy assessment of its robustness. A quantitative measure of the robustness of the discrete-time LQ state feedback is then used to study the effect of the two different representations: the Euler and the shift operator formulations. It is shown that the discrete-time LQ state feedback using the Euler operator is more robust against nonlinear perturbations than that using the shift operator. Moreover, the resulting response becomes much closer to that of the continuous LQ state feedback as the sampling rate increases, than the shift-operator case.

1.3 Simulation and Experiments

Simulations are performed to assess the on-line capability of the proposed control scheme. The mechanism under consideration is a planar four-bar linkage of the crank-rocker type, where some or all moving links are flexible. In designing a prototype mechanism, the links are made to be slender and long wherever possible, so that they may be modelled using the Euler-Bernoulli beam theory. Moreover, the joints are carefully designed to achieve accurate kinematic couplings, while minimizing their weights. The prototype mechanism is manufactured and integrated into a data-acquisition system comprising two digital signal processors, along with analog-to-digital and digital-to-analog converters. The experimental verification of the proposed control scheme is carried out using the prototype mechanism.

The angle of rotation of the input link and its time-rate of change are measured and used to infer the rest of the rigid-body motions. The vibrational behaviour of the mechanism is then measured using two sets of full-bridge strain gauges that are installed at the midspan of the coupler and output links. When this output and the input joint torques are sampled, the model-based Kalman filter reconstructs the state variables. The joint torque can then be obtained from the admissible control law in conjunction with the NOC filter. This torque is in turn applied to the system via a precision DC motor and to the said Kalman filter.

One aspect of this study is to assess the viability of calculating the NOC on-line, which is essential for the successful implementation of the proposed control algorithm. The experimental study is thus focused on the numerical performance of the NOC filter. In this regard, the Euler-operator formulation that closely approximates the corresponding continuous-time system is used for the discrete-time system representation. The filter is executed on a 33M-flops digital signal processor (DSP). The experimental results show that the desired performance of the control system can be achieved with sampling rates as high as 200 Hz.

Knowing that this type of mechanism possesses singularities intrinsically, both simulation and experimental results are compared in order to investigate the effect of those singularities on the applied torque. This is significant in analyzing the system response, because a rapid inertia change, which may affect the system dynamics greatly, occurs in the neighbourhood of a singular configuration. Experimental studies show that the rapid inertia change at the singular configurations appears in the form of disturbances. Hence, the capability of attenuating the disturbances has been considered in designing the LQG compensator. Moreover, an open-loop simulation using the inverse dynamics of the corresponding rigid-body model is conducted to show a difficulty of the simulation study under the influence of rapid inertia changes that occur near the singular configuration.

An experimental study on the control of a rotating flexible beam is also conducted. As discussed earlier, the use of cubic splines allows a definition of the state-variable vector as the set of curvature values at the nodal points of the spline and their time-rates of change. The former are measured directly with strain gauges, while the latter are estimated with a Kalman filter. The objective of this experiment is to address the observability and controllability of the rotating flexible beam with a torque applied at the hub of the beam using the smallest possible number of measurements. The experimental results indicate that the estimation of the state variables can be accomplished if at least two measurements are taken, these being the curvature at the root of the beam and the hub rotational angle. Moreover, the vibration of the flexible beam can be successfully suppressed by means of the applied torque obtained with the admissible control law in conjunction with the Kalman filter.

1.4 Thesis Overview

This thesis consists of eight chapters, which are outlined below:

Chapter 1 is devoted to the background and motivation of the research to be presented in this thesis. It includes the definitions of some basic concepts, literature survey and description of the problems that are covered throughout the thesis.

Chapter 2 deals with the spatial discretization of the continuous beam. Two spatial discretization methods are presented, i.e., a normal-mode method and a cubic-spline technique. Cases for two different boundary conditions—pinned-pinned and clamped-free—are discussed for each of the two spatial discretization methods.

Chapter 3 presents a kinematic formulation for a mechanism having a closed kinematic chain. An equivalent rigid-link system (ERLS) is used to resolve the overall motion of the mechanism into the sum of a rigid-body motion and a flexible-body motion. The kinematic constraint equations are then formulated and the independent and dependent generalized speeds are defined based on the said equations. The orthogonal complement of the foregoing constraints equations is extracted from the reciprocity relations between the independent generalized speeds and the constraint forces, and is defined as the underlying natural orthogonal complement (NOC).

Chapter 4 is devoted to the formulation of the governing equations exploiting the properties provided by the NOC, namely, those naturally incorporating the constraints into the equations of motion and eliminating the constraint forces thus introduced. The equations of motion for each separate link are constructed using Lagrange's equations and then assembled to give the unconstrained equations of motion for the entire system. The latter are called the uncoupled equations of motion. The coupled equations of motion are then obtained by multiplying both sides of the uncoupled equations of motion by the transpose of the NOC. Finally, the dynamic formulation of a rotating flexible beam is presented in detail at the end of this chapter.

Chapter 5 provides the robustness analysis of the dynamic models of the rotating flexible beam obtained using both spatial discretization methods, namely, the normal-mode approach and the cubic-spline technique. A sensitivity analysis of the linear-quadratic-Gaussian (LQG) compensator is performed to assess the capability of attenuating estimation errors due to unmodelled higher-order dynamics. The allowable bound for nonlinear perturbations is also sought in conjunction with LQ state feedback. For the said dynamic models, the sensitivity analysis is used to investigate the effect of the observation spillover, whereas the allowable bound is exploited to test the robustness against the control spillover.

Chapter 6 is concerned with the design of a model-based control scheme and its on-line implementation. The control scheme consists of two blocks: the first bock is devoted to the linearization of the highly coupled nonlinear system, while the second block is assigned to obtain the required applied torques from the generalized forces. This partitioning of the control scheme is feasible on the basis of using the NOC as a filter. This control system is then discretized and expressed in the Euler operator, which provides close connections between the continuous- and the discrete-time results. Two theorems are developed to quantitatively measure the robustness bound of the discrete-time linear-quadratic (LQ) state feedback in the presence of nonlinear perturbations. These theorems allow the robustness measure of the discrete-time LQ state feedback associated with the use of different operators; i.e., as the shift and Euler operators.

Chapter 7 presents the numerical and experimental results for the proposed control scheme designed for the planar four-bar mechanism of the crank-rocker type. The control algorithm is numerically implemented on the simulator based on the nonlinear equations of motion. Based on these results, the prototype mechanism is manufactured and then integrated into a data-acquisition system. The experimental verification of the proposed control scheme is carried out using the setup thus made. Several issues are addressed concerning the experimental results such as the effects of the singularities and rapid inertia changes. Moreover, the experimental results for the control of the rotating flexible beam are included in this chapter.

Chapter 8 is devoted to the conclusions derived from this research work. The results thus obtained are summarized and then, some suggestions are made for further work.

Chapter 2

Spatial Discretization of Continuous Systems

2.1 Introduction

The governing PDE of a uniform beam that is subject to only bending is obtained using the extended Hamilton principle, along with necessary boundary conditions. The method of separation of variables enables us to convert the PDE into two sets of ODEs in the time and space domains. Two spatial discretization methods, one based on normal modes, the other one cubic splines, are used to find a proper approximate solution of the fourth-order ODE associated with the spatial variable. Cases for two different boundary conditions—pinned-pinned and clamped-free—are discussed in conjunction with both spatial discretization methods.

In the normal-mode approach, the displacement is approximated as a finite sum consisting of the normal modes and the corresponding time-dependent coordinates, commonly known as the normal coordinates. For the uniform beam, the natural modes are solved by finding a general solution of the fourth-order ODE in space and applying appropriate boundary conditions therein. The natural modes are normalized for the sake of convenience. The normal modes thus produced then satisfy the orthogonality conditions.

In the cubic-spline technique, the displacement functions between the supporting points are given in the form of piecewise third-order polynomials having continuous second derivatives (Rogers and Adams, 1976). The overall displacement is then constructed by an interpolation of the set of physical data taken at the supporting points. Boundary conditions are then imposed to eliminate the need of finding the extra coefficients that result from the use of the cubic splines. A linear relation between the displacement and the curvature values is given at the end.

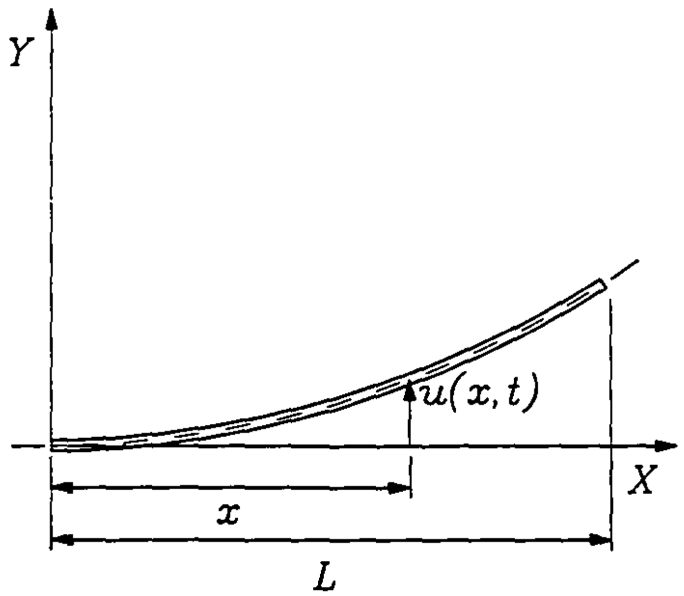

Figure 2.1: Bending deformation in a uniform beam

2.2 The Euler-Bernoulli Beam

The relation between bending moment and deformation in a flexible beam is given by

$$M(x,t) = EI(x)\frac{\partial^2 u(x,t)}{\partial x^2} \tag{2.1}$$

where $EI(x)$ is the flexural rigidity, consisting of Young's modulus E and the cross-sectional area moment of inertia $I(x)$ about an axis normal to the XY plane and passing through the centre of the cross-section. Moreover, $u(x,t)$ denotes the transverse displacement along the beam at any point x and time t, as given in Fig. 2.1.

The potential energy associated with the deformation of the beam has the form:

$$V = \frac{1}{2}\int_0^L EI(x)\left[\frac{\partial^2 u(x,t)}{\partial x^2}\right]^2 dx \tag{2.2}$$

In addition, the kinetic energy can be expressed as

$$T = \frac{1}{2}\int_0^L m(x)\left[\frac{\partial u(x,t)}{\partial t}\right]^2 dx \tag{2.3}$$

where $m(x)$ is the mass per unit length.

Applying the Hamilton principle, the governing PDE is found by minimizing the following function

$$I = \int_{t_1}^{t_2}(T-V)dt \tag{2.4}$$

$$= \frac{1}{2}\int_{t_1}^{t_2}\int_0^L \left(m(x)\left[\frac{\partial u}{\partial t}\right]^2 - EI(x)\left[\frac{\partial^2 u}{\partial x^2}\right]^2\right) dx\ dt \tag{2.5}$$

This can be achieved with the aid of the calculus of variations, namely, as

$$\delta I = \delta(I_1 - I_2) = 0 \tag{2.6}$$

where

$$\delta I_1 = \int_{t_1}^{t_2}\int_0^L m(x)\frac{\partial u}{\partial t}\frac{\partial(\delta u)}{\partial t}dx\ dt \tag{2.7}$$

$$\delta I_2 = \int_{t_1}^{t_2}\int_0^L EI(x)\frac{\partial^2 u}{\partial x^2}\frac{\partial^2(\delta u)}{\partial x^2}dx\ dt \tag{2.8}$$

Performing the standard integration by parts for δI_1 gives

$$\delta I_1 = \int_0^L m(x)\frac{\partial u}{\partial t}\ \delta u|_{t_1}^{t_2}\, dx\ - \int_{t_1}^{t_2}\int_0^L m(x)\frac{\partial^2 u}{\partial t^2}\delta u dx\ dt \tag{2.9}$$

Since the variation δu must vanish at t_1 and t_2 by definition, one obtains

$$\delta I_1 = -\int_{t_1}^{t_2}\int_0^L m(x)\frac{\partial^2 u}{\partial t^2}\delta u dx\ dt \tag{2.10}$$

Applying the same procedures to δI_2 produces

$$\begin{aligned}\delta I_2 = & \int_{t_1}^{t_2} EI(x)\tfrac{\partial^2 u}{\partial x^2}\tfrac{\partial(\delta u)}{\partial x}\Big|_0^L dt \; - \int_{t_1}^{t_2} \tfrac{\partial}{\partial x}\left(EI(x)\tfrac{\partial^2 u}{\partial x^2}\right)\delta u\Big|_0^L dt \\ & + \int_{t_1}^{t_2}\int_0^L \tfrac{\partial^2}{\partial x^2}\left(EI(x)\tfrac{\partial^2 u}{\partial x^2}\right)\delta u dx\, dt\end{aligned} \tag{2.11}$$

Now, combining eqs.(2.10) and (2.11) and collecting the integrands that contain δu, one obtains the three equations below:

$$\int_{t_1}^{t_2}\int_0^L \left(\frac{\partial^2}{\partial x^2}\left(EI(x)\frac{\partial^2 u}{\partial x^2}\right) + m(x)\frac{\partial^2 u}{\partial t^2}\right)\delta u dx\, dt = 0 \tag{2.12}$$

$$\int_{t_1}^{t_2} \frac{\partial}{\partial x}\left(EI(x)\frac{\partial^2 u}{\partial x^2}\right)\delta u\Big|_0^L dt = 0 \tag{2.13}$$

$$\int_{t_1}^{t_2} EI(x)\frac{\partial^2 u}{\partial x^2}\frac{\partial(\delta u)}{\partial x}\Big|_0^L dt = 0 \tag{2.14}$$

From the foregoing equations, the governing PDE can be obtained as

$$\frac{\partial^2}{\partial x^2}\left(EI(x)\frac{\partial^2 u}{\partial x^2}\right) + m(x)\frac{\partial^2 u}{\partial t^2} = 0 \tag{2.15}$$

along with all possible boundary conditions:

$$EI(x)\frac{\partial^2 u}{\partial x^2}\frac{\partial(\delta u)}{\partial x}\Big|_0^L = 0 \tag{2.16}$$

$$\left(EI(x)\frac{\partial^2 u}{\partial x^2}\right)\delta u\Big|_0^L = 0 \tag{2.17}$$

The latter can be translated into the boundary conditions given below:

- clamped end: $u = 0$, $\frac{\partial u}{\partial x} = 0$
- pinned end: $u = 0$, $\frac{\partial^2 u}{\partial x^2} = 0$
- free end: $\frac{\partial^2 u}{\partial x^2} = 0$, $\frac{\partial^3 u}{\partial x^3} = 0$

The method of separation of variables, on the other hand, enables us to write the foregoing PDE as two sets of ODEs in the space and time domains, namely,

$$\frac{d^2}{dx^2}\left(EI(x)\frac{d^2 Y}{dx^2}\right) - \omega^2 m(x)\frac{d^2 Y}{dt^2} = 0 \tag{2.18}$$

$$\frac{d^2 q(t)}{dt^2} + \omega^2 q(t) = 0 \tag{2.19}$$

where ω^2 is a positive quantity representing the square of the natural frequency ω.

2.3 Normal-Mode Approach

In the normal-mode approach, the transverse vibration of the flexible link can be approximated by a finite number of the normal modes obtained by determining the eigenfunctions of the system, while satisfying the boundary conditions. The displacement function is then given by

$$u(x,t) = \sum_{r=1}^{n-1} Y_r(x)\, q_r(t) \tag{2.20}$$

where $Y_r(x)$ denotes the rth eigenfunction, also known as the rth *mode*, and $\{q_r(t)\}_{r=1}^{n-1}$ are the time-dependent generalized coordinates. Since these coordinates are not attached to any physical quantity, they are not measurable.

In the two subsections below, the normal modes satisfying eq.(2.18) are derived in conjunction with two sets of boundary conditions: pinned-pinned and clamped-free.

2.3.1 Pinned-Pinned Beam

In this case, the geometric and natural boundary conditions are given, respectively, by

$$u(0,t) = u(L,t) = 0 \tag{2.21}$$

$$u''(0,t) = u''(L,t) = 0 \tag{2.22}$$

which means that the deflection and the bending moment at both ends vanish.

While imposing the aforementioned boundary conditions, the nontrivial solution of eq.(2.18) reduces to

$$Y_r = C_r \sin \kappa_r x, \quad r = 1, \cdots, n-1 \tag{2.23}$$

where C_r is any constant that satisfies the normality conditions

$$m \int_0^L Y_r^2(x)dx \; = 1 \tag{2.24}$$

In addition, κ_r in eq.(2.23) is obtained from the characteristic equation

$$\sin \kappa_r L = 0 \tag{2.25}$$

The solution of the characteristic equation can be readily obtained as

$$\kappa_r L = r\pi, \quad r = 1, \cdots, n-1 \tag{2.26}$$

Moreover, the natural frequencies, for $r = 1, \cdots, n-1$, are

$$\omega_r = (r\pi)^2 \sqrt{\frac{EI}{mL^4}} \tag{2.27}$$

Furthermore, the normal modes thus obtained must satisfy the orthogonality conditions given below:

$$\int_0^L m(x) Y_r(x) Y_s(x) dx = \delta_{rs}, \qquad r, s = 1, 2, \cdots \tag{2.28}$$

$$\int_0^L EI(x) \frac{d^2 Y_r(x)}{dx^2} \frac{d^2 Y_s(x)}{dx^2} dx = \omega_r^2 \delta_{rs}, \qquad r, s = 1, 2, \cdots \tag{2.29}$$

where δ_{rs} is the Kronecker delta. These relations mean that all the modes are orthogonal to one another (Meirovitch 1967). Such orthogonality conditions will greatly reduce the complexity in forming the equations of motion, especially whenever elastic motions are induced by the rigid body motion. However, these relations will bring forth some difficulties in connection with the controller, as discussed in Chapter 5.

2.3.2 Clamped-Free Beam

In the presence of clamped-free boundary conditions, the solutions of eq.(2.18), which are known as eigenfunctions, lead to $r = 1, \ldots, n-1$,

$$\begin{aligned} Y_r(x) = A_r((&\sin \kappa_r L - \sinh \kappa_r L)(\sin \kappa_r x - \sinh \kappa_r x) \\ &+ (\cos \kappa_r L + \cosh \kappa_r L)(\cos \kappa_r x - \cosh \kappa_r x)), \quad r = 1, \cdots, n-1 \end{aligned} \tag{2.30}$$

where

$$A_r = C_r / (\sin \kappa_r L - \sinh \kappa_r L) \tag{2.31}$$

with C_r defined as a normalizing constant and κ_r denoting the rth eigenvalue defined as the rth root of the characteristic equation, namely,

$$\cos\kappa_r L \cosh\kappa_r L = -1 \tag{2.32}$$

2.4 Cubic-Spline Technique

The link deformation $u(x,t)$ in the interval $x_r \le x \le x_{r+1}$ is approximated by a cubic spline function as

$$u(x,t) = A_r(x-x_r)^3 + B_r(x-x_r)^2 + C_r(x-x_r) + D_r \tag{2.33}$$

where x_r is the abscissa of the rth supporting point of the spline (Dierckx, 1993). Deriving the coefficients as functions of the displacement u and the curvature u'' at the rth supporting point yields

$$A_r = \frac{1}{6\Delta x_r}(u''_{r+1} - u''_r), \tag{2.34}$$

$$B_r = \frac{1}{2}u''_r \tag{2.35}$$

$$C_r = \frac{\Delta u_r}{\Delta x_r} - \frac{1}{6}\Delta x_r(u''_{r+1} + 2u''_r), \tag{2.36}$$

$$D_r = u_r \tag{2.37}$$

where $\Delta x_r = x_{r+1} - x_r$ and $\Delta u_r = u_{r+1} - u_r$. Furthermore, the requirement of continuity in the first derivative is imposed, namely,

$$u'_r(x_{r+1}) = u'_{r+1}(x_{r+1}) \qquad \text{for } r = 1, ..., n-2 \tag{2.38}$$

After substituting eqs. (2.34), (2.35), (2.36) and (2.37) into eq. (2.33), one obtains a linear system of $(n-2)$ simultaneous equations, i.e.,

$$\alpha_r u''_r + 2(\alpha_r + \alpha_{r+1})u''_{r+1} + \alpha_{r+1}u''_{r+2} = 6\,[\beta_r u_r - (\beta_r + \beta_{r+1})u_{r+1} + \beta_{r+1}u_{r+2}] \tag{2.39}$$

where $\alpha_r \equiv \Delta x_r$ and $\beta_r \equiv 1/\Delta x_r$ for $r = 1, ..., n-2$. Notice that we have $(n-2)$ equations here for the given n-dimensional curvature vector. It is, therefore, required to find two more equations that are obtained by considering the boundary conditions.

2.4.1 Pinned-Pinned Beam

The geometric and natural boundary conditions associated with the pinned-pinned beam can be expressed in terms of the corresponding values at the the discretized supporting points, namely, as

$$u_1 = u_n = 0 \tag{2.40}$$

$$u_1'' = u_n'' = 0 \tag{2.41}$$

Imposing the foregoing boundary conditions to eq.(2.39) eliminates two unknowns in the foregoing system, and hence, gives the $(n-2)$ linear relationships between curvature and displacement, namely,

$$\mathbf{A}_p\,\mathbf{u}'' = 6\,\mathbf{C}_p\,\mathbf{u} \tag{2.42}$$

where

$$\mathbf{A}_p = \begin{bmatrix} 2\alpha_1' & \alpha_2 & 0 & \dots & 0 \\ \alpha_2 & 2\alpha_2' & \alpha_3 & \dots & 0 \\ 0 & \ddots & \ddots & \ddots & \vdots \\ 0 & \dots & 0 & \alpha_{n-3} & 2\alpha_{n-3}' \end{bmatrix} \tag{2.43}$$

$$\mathbf{C}_p = \begin{bmatrix} -\beta_1' & \beta_2 & 0 & \dots & 0 \\ \beta_2 & -\beta_2' & \beta_3 & \dots & 0 \\ 0 & \ddots & \ddots & \ddots & \vdots \\ 0 & \dots & 0 & \beta_{n-3} & -\beta_{n-3}' \end{bmatrix} \tag{2.44}$$

with

$$\alpha_r' \equiv \alpha_r + \alpha_{r+1},\ \beta_r' \equiv \beta_r + \beta_{r+1},\ \text{for } r = 1, ..., n-3$$

In eq. (2.42), $\mathbf{u}$ is the vector of time-varying displacements and $\mathbf{u}''$ is the vector of time-varying curvatures at the supporting points, i.e.,

$$\mathbf{u} = \begin{bmatrix} u_2, \dots, u_{n-1} \end{bmatrix}^T \in I\!R^{(n-2)} \tag{2.45}$$

$$\mathbf{u}'' = \begin{bmatrix} u_2'', \dots, u_{n-1}'' \end{bmatrix}^T \in I\!R^{(n-2)} \tag{2.46}$$

Thus, eq. (2.42) leads to

$$\mathbf{u} = \mathbf{T}_p \mathbf{u}'' \tag{2.47}$$

where

$$\mathbf{T}_p = \frac{1}{6}\mathbf{C}_p^{-1}\mathbf{A}_p$$

with $\mathbf{C}_p$ being nonsingular.

2.4.2 Clamped-Free Beam

The boundary conditions for this beam have been found to be very useful in the analysis of a simple structural element. It has been reported that such boundary conditions possesses better numerical properties than the pinned-pinned boundary conditions in predicting the closed-loop system dynamics where feedback control is necessary (Cetinkunt and Yu, 1992).

The corresponding geometric boundary conditions at the clamped end, $x = 0$, are given as

$$u(0,t) = 0, \;\; \frac{\partial u}{\partial x}(0,t) = 0 \tag{2.48}$$

The foregoing boundary conditions add one more equation, namely,

$$2\alpha_1 u_1'' + \alpha_1 u_2'' = 6\beta_1(u_2 - u_1) \tag{2.49}$$

Moreover, at the free end, $x = L$, both the moment and the shear force exerted on the link vanish, so that

$$\frac{\partial^2 u}{\partial x^2}(L,t) = 0, \;\; \frac{\partial^3 u}{\partial x^3}(L,t) = 0 \tag{2.50}$$

Applying the zero shear force at the free end produces

$$u_n''' = 6A_{n-1} \tag{2.51}$$

$$= u_n'' - u_{n-1}'' = 0 \tag{2.52}$$

Hence,

$$u_n'' = u_{n-1}'' \tag{2.53}$$

Finally, the $(n-1)$ linear relationships between curvature and displacement, including eqs.(2.49) and (2.53), can be written in vector form as

$$\mathbf{A}_c\, \mathbf{u}'' = 6\, \mathbf{C}_c\, \mathbf{u} \tag{2.54}$$

where

$$\mathbf{A}_c = \begin{bmatrix} 2\alpha_1 & \alpha_1 & 0 & \dots & 0 \\ \alpha_1 & 2\alpha_1' & \alpha_2 & \dots & 0 \\ 0 & \ddots & \ddots & \ddots & \vdots \\ 0 & \dots & \alpha_{n-3} & 2\alpha_{n-3}' & \alpha_{n-2} \\ 0 & \dots & 0 & \alpha_{n-2} & 2\alpha_{n-2}' \end{bmatrix} \tag{2.55}$$

$$\mathbf{C}_c = \begin{bmatrix} \beta_1 & 0 & 0 & \dots & & 0 \\ -\beta_1' & \beta_2 & 0 & \dots & & \\ \beta_2 & -\beta_2' & \beta_3 & 0 & & \\ 0 & \ddots & \ddots & \ddots & \ddots & \vdots \\ 0 & \dots & 0 & \beta_{n-2} & -\beta_{n-2}' & \beta_{n'} \end{bmatrix} \tag{2.56}$$

In eq.(2.54), $\mathbf{u}$ is the vector of time-varying displacements and $\mathbf{u}''$ is the vector of time-varying curvatures at the supporting points, i.e.,

$$\mathbf{u} = \begin{bmatrix} u_2, \dots, u_n \end{bmatrix}^T \in \mathbb{R}^{(n-1)} \tag{2.57}$$

$$\mathbf{u}'' = \begin{bmatrix} u_1'', \dots, u_{n-1}'' \end{bmatrix}^T \in \mathbb{R}^{(n-1)} \tag{2.58}$$

Thus, eq.(2.54) leads to

$$\mathbf{u} = \mathbf{T}_c \mathbf{u}'' \tag{2.59}$$

where

$$\mathbf{T}_c = \frac{1}{6}\mathbf{C}_c^{-1}\mathbf{A}_c$$

with $\mathbf{C}_c$ being nonsingular.

The displacement function $u_r(x,t)$ given in eq.(2.33) can be written also in vector form, namely,

$$u_r(x,t) = \left[\ (x-x_r)^3 \quad (x-x_r)^2 \quad (x-x_r) \quad 1\ \right] \begin{bmatrix} A_r(t) \\ B_r(t) \\ C_r(t) \\ D_r(t) \end{bmatrix} \tag{2.60}$$

Defining $\mathbf{s}_r(x)$ as

$$\mathbf{s}_r(x) \equiv \left[\ (x-x_r)^3 \quad (x-x_r)^2 \quad (x-x_r) \quad 1\ \right]^T \tag{2.61}$$

and substituting the time varying coefficients given in terms of displacements and curvatures at the supporting points into eq.(2.60) produces

$$u_r(x,t) = \mathbf{s}_r^T \mathbf{U}''_r \mathbf{u}'' + \mathbf{s}_r^T \mathbf{U}_r \mathbf{u} \tag{2.62}$$

in which $\mathbf{U}''_r$ and $\mathbf{U}_r$ are given by

$$\mathbf{U}''_r = \begin{bmatrix} 0 & \dots & 0 & -\beta_r/6 & \beta_r/6 & 0 & \dots & 0 \\ 0 & \dots & 0 & 1/2 & 0 & 0 & \dots & 0 \\ 0 & \dots & 0 & -\alpha_r/3 & -\alpha_r/6 & 0 & \dots & 0 \\ 0 & \dots & 0 & 0 & 0 & 0 & \dots & 0 \end{bmatrix} \tag{2.63}$$

$$\mathbf{U}_r = \begin{bmatrix} 0 & \dots & 0 & 0 & 0 & 0 & \dots & 0 \\ 0 & \dots & 0 & 0 & 0 & 0 & \dots & 0 \\ 0 & \dots & 0 & -\beta_r & \beta_r & 0 & \dots & 0 \\ 0 & \dots & 0 & 1 & 0 & 0 & \dots & 0 \end{bmatrix}. \tag{2.64}$$

Note that $\mathbf{U}''_r$ is a $4 \times (n-1)$ matrix whose only nonzero entries appear in its $(r+1)$st and rth columns, when clamped-free boundary conditions are imposed, while $\mathbf{U}''_r$ is a $4 \times (n-2)$ matrix whose only nonzero entries appear in its $(r+1)$st and rth columns, when pinned-pinned boundary conditions are imposed. Moreover, $\mathbf{U}_r$ is a

$4 \times (n-1)$ matrix whose only nonzero entries appear in its rth and $(r-1)$st columns, when clamped-free boundary conditions are imposed, while $\mathbf{U}_r$ is a $4 \times (n-2)$ matrix whose only nonzero entries appear in its $(r+1)$st and rth columns, when pinned-pinned boundary conditions are imposed.

Furthermore, using the linear relationship between displacement and curvature given in eq.(2.59), the displacement function $u_r(x,t)$ becomes

$$u_r(x,t) = \mathbf{s}_r^T(x)\, \mathbf{\Delta}_r\, \mathbf{u}''(t) \tag{2.65}$$

where

$$\mathbf{\Delta}_r = \mathbf{U}_r'' + \mathbf{U}_r \mathbf{T}_c \tag{2.66}$$

Chapter 3

Kinematics of a Flexible Mechanism

3.1 Introduction

Unlike systems with open kinematic chains where the terminal link has a free end, the kinematic formulation of closed-chain systems requires considering that the terminal link is constrained at both ends. The kinematic constraint equations of a flexible mechanism simultaneously involve rigid-body and flexible-body motions. Furthermore, the axial shortening effect, also known as geometric shortening, cannot be neglected if the angular rates of the bodies are comparable to their first natural frequency (Cyril, 1988). This effect significantly increases the complexity of the kinematic formulation.

An equivalent rigid-link system (ERLS) has been introduced to resolve the overall motion of a serial-type flexible system into the sum of a rigid-body motion and a flexible-body motion (Giovagnoni, 1994; Chang and Hamilton, 1991). This ERLS is then extended to incorporate a flexible mechanism with closed kinematic chains, which greatly facilitates the kinematic formulation, because the equivalent rigid-body motion can be extracted from the overall motion of the flexible system by applying the ERLS. It is noteworthy that *a priori* knowledge of the rigid-body motion is not necessary in this formulation, since the nominal motion of the chain of rigid bodies is simultaneously constituted from the motion of the ERLS. Consequently, the said

ERLS considers the couplings between the rigid-body and the flexible-body motions.

The generalized speeds thus obtained from the kinematic velocity constraints include both independent and dependent generalized speeds. The dependent generalized speeds arise from the coupling of each intermediate link with its neighbours and constraints due to loop closures. The use of the ERLS enables us to write the vector of generalized speeds in terms of the vector of independent generalized speeds. This establishes a transformation that is an explicit function of the configuration of the mechanism and is called the natural orthogonal complement (NOC) (Angeles and Lee, 1989). The NOC will be used to form the system of dynamic equations in terms of the generalized coordinates, by eliminating the need to solve for constraint forces.

3.2 An Equivalent Rigid-Link System (ERLS)

An equivalent rigid-link system (ERLS) has been found to be very useful and efficient in describing the overall motion of a serial-type flexible manipulator (Chang and Hamilton, 1991). With the ERLS, the motion involved in such a system can be readily expressed as the sum of a large motion and a small motion. The large motion is attributed to the motion of the equivalent rigid-body system, while the small motion accounts for deviations of the flexible system with respect to its equivalent rigid-body motion. The small motion is mainly due to the structural flexibilities and partly due to the rigid-body motion. Consequently, the use of the ERLS allows the closure form of the kinematic constraint equations in terms of rigid-body motions and associated link deflections. However, it is noteworthy that the ERLS is only a hypothetical system, which is the closest rigid system to the corresponding flexible system.

Here, the ERLS is extended to incorporate a flexible mechanism with a closed kinematic chain. Unlike the serial-type flexible system, where the line between joints i and $i+1$ is drawn parallel to the tangent at the distal end of link i (Fig. 3.1), in a flexible mechanism the line is drawn between joint i and joint $i+1$ (Fig. 3.2). The extended ERLS approximates the said flexible mechanism, while serving to separate

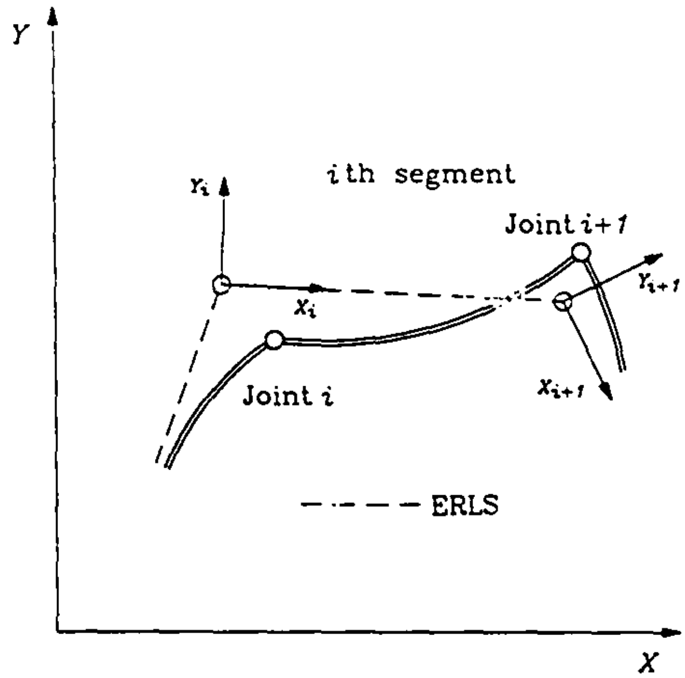

Figure 3.1: Equivalent rigid-link system for a serial flexible manipulator

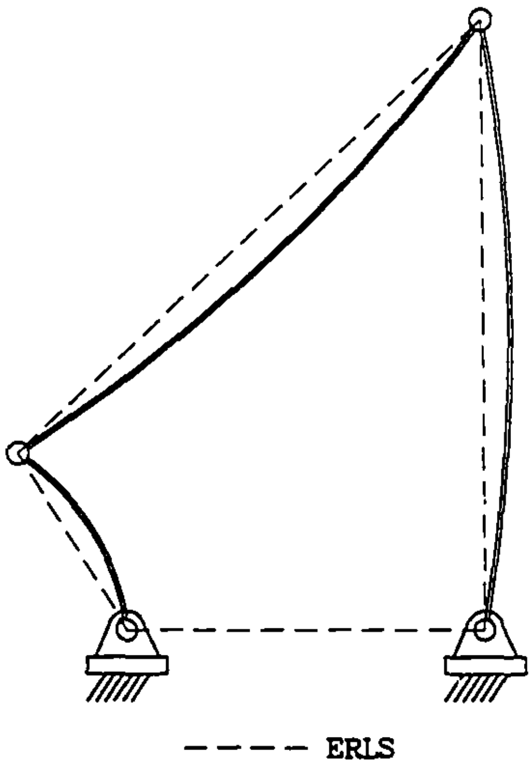

Figure 3.2: Equivalent rigid-link system for a flexible mechanism with a closed kinematic loop

the overall motion into the rigid-body and the elastic motions. Moreover, the linear relation between curvature and displacement derived in the previous chapter can be employed if displacements measured from the moving rigid-body configuration are small.

3.3 Kinematic Constraint Equations

The mechanical system considered here is a planar four-bar linkage where some or all links are flexible (Fig. 3.3). It is driven by an actuator at point O_2. The coupler and output links length of (a_3) and (a_4), respectively, are constrained to follow the motion of the input link length of (a_2), while the base link length of (a_1) is fixed and acts as a reference frame. The actuated link is modelled as a beam with clamped-free end conditions and undergoes axial deflection due to geometric shortening. The unactuated links are modelled as pinned-pinned beams. As a result, the endpoints of these links are fixed relative to the link axes.

The architecture of the linkage is simply defined by the undeformed length of link i—denoted as a_i—where $i = 1, \ldots, 4$, as shown in Fig. 3.3. The configuration of the linkage is described by a set of independent rotational and flexible coordinates. These consist of the angle of rotation of the input link, θ_2, along with the elastic coordinates of flexible links, each of which is represented by an l-dimensional vector $\mathbf{u}''_i$. Moreover, $\mathbf{u}''_i$ is the vector of curvature values measured along link i, from which the supporting points are taken.

3.3.1 Axial Shortening Effect

Since the aforementioned mechanism should accommodate faster operating speeds with a high degree of accuracy, axial shortening has to be included in the kinematic formulation. However, consideration of the axial shortening may require additional generalized coordinates (Kane, Ryan and Banerjee, 1987). Hence, a method must

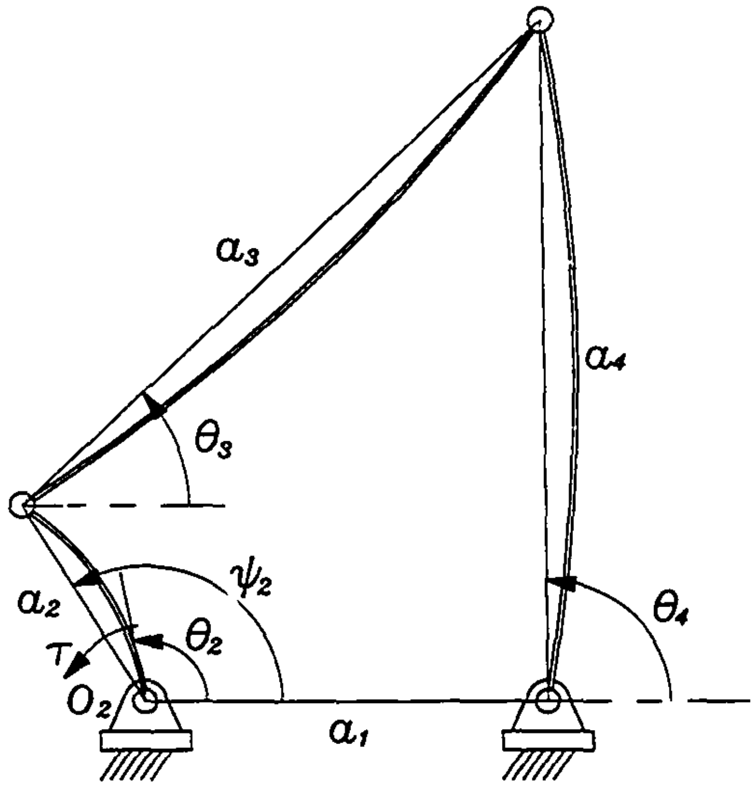

Figure 3.3: Architecture of a four-bar linkage

be sought to effectively model this effect without introducing additional generalized coordinates.

Figure 3.4 shows a schematic diagram of the axial shortening effect due to the elastic deformation. The assumption of the constant link length under the clamped-free boundary condition is no longer valid when the structural members of the mechanism undergo relatively large elastic deformation.

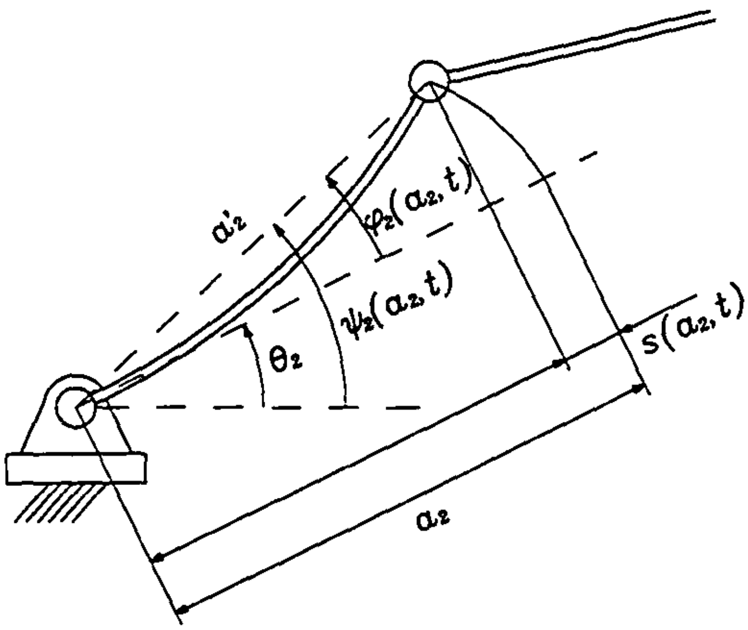

Figure 3.4: Schematic diagram of the axial shortening

The shortening over the length of the beam can be obtained as

$$s(a_i,t) \simeq \int_0^{a_i} (ds - dx) \tag{3.1}$$

where ds denotes the length of a small section of the deflected beam, while dx denotes the that of the undeformed beam. The length of a small section of the deflected beam is given by

$$ds = \left[1 + \left(\frac{du}{dx}\right)^2\right]^{\frac{1}{2}} dx \tag{3.2}$$

where du is the deflection associated with a small section dx along the neutral axis attached to the undeformed position of link i. Taking a truncated series expansion of the foregoing equation gives

$$\left[1+\left(\frac{du}{dx}\right)^2\right]^{\frac{1}{2}} \simeq 1+\frac{1}{2}\left(\frac{du}{dx}\right)^2 \tag{3.3}$$

Substituting the approximation into eq.(3.2), one obtains

$$ds - dx = \frac{1}{2}\left(\frac{du}{dx}\right)^2 dx \tag{3.4}$$

Equation (3.1) then becomes

$$s(a_i,t) = \frac{1}{2}\int_0^{a_i}\left(\frac{du}{dx}\right)^2 dx \tag{3.5}$$

By virtue of the cubic-spline technique, eq.(3.5) can be expressed in a discretized form, namely,

$$s(a_i,t) = \frac{1}{2}\sum_{j=1}^{a_i}\left(\int_{x_j}^{x_{j+1}} \mathbf{u''}_i^T\ \boldsymbol{\Delta}_j^T \mathbf{F}_j'(x)\boldsymbol{\Delta}_j \mathbf{u''}_i\, dx\right) \tag{3.6}$$

where $\boldsymbol{\Delta}_j \equiv \mathbf{U}_j'' + \mathbf{U}_j\mathbf{T}_c$ and

$$\mathbf{F}_j'(x) \equiv \frac{\partial \mathbf{s}_j(x)}{\partial x}\frac{\partial \mathbf{s}_j{}^T(x)}{\partial x} \tag{3.7}$$

If we define

$$\boldsymbol{\Upsilon}_i \equiv \sum_{j=1}^{a_i}\left(\int_{x_j}^{x_{j+1}} \boldsymbol{\Delta}_j^T \mathbf{F}_j'(x)\boldsymbol{\Delta}_j dx\right) \tag{3.8}$$

then eq.(3.6) becomes

$$s(a_i,t) = \frac{1}{2}\mathbf{u''}_i^T\ \boldsymbol{\Upsilon}_i \mathbf{u''}_i \tag{3.9}$$

As shown in the foregoing equation, the axial shortening effect can be systematically considered without introducing additional generalized coordinates.

Towards this end, several kinematic parameters are introduced. Using the displacement function obtained in eq.(2.65), the deformation at the end of the input link is defined as

$$u^2(a_i,t) = \mathbf{u''}_i^T\ \boldsymbol{\Theta}_i \mathbf{u''}_i \tag{3.10}$$

where

$$\Theta_i = \Delta_l^T \mathbf{F}(a_i) \Delta_l \tag{3.11}$$

and where

$$\mathbf{F}(a_i) \equiv \mathbf{s}_l(a_i) \mathbf{s}_l^T(a_i) \tag{3.12}$$

The length of the equivalent rigid-link can be expressed as

$$a_i' = \sqrt{(a_i - s(a_i, t))^2 + u(a_i, t)^2} \tag{3.13}$$

Substituting eqs.(3.9) and (3.10) into the above equation, we obtain

$$a_i' = \sqrt{a_i^2 - \mathbf{u}''^T_i \left[a_i \Upsilon_i - \frac{1}{4} \Upsilon_i^T \mathbf{u}''_i \, \mathbf{u}''^T_i \, \Upsilon_i - \Theta_i \right] \mathbf{u}''_i} \tag{3.14}$$

In addition, the angle φ_i defined between the undeformed position of link i and the line extending from the origin to the end-point is given by:

$$\varphi_i = \tan^{-1}\left(\frac{u(a_i, t)}{a_i'}\right) \tag{3.15}$$

It should be noted that the link lengths remain constant for unactuated links due to pinned-pinned boundary conditions, i.e., $a_i' = a_i$.

3.3.2 Joint Angles

Given the independent coordinates as input, it is desired to find the values of the unactuated joint angles, i.e, θ_3 and θ_4. This can be readily achieved by virtue of the ERLS and the constraint equation imposed on it, namely,

$$\mathbf{a}_2 + \mathbf{a}_3 = \mathbf{a}_4 + \mathbf{a}_1 \tag{3.16}$$

It is recognized that some of the quantities that are constant in the rigid case become variables if the linkage is flexible. Specifically, the link lengths a_i should be replaced with those of equivalent rigid-links a_i'.

Equation (3.16) provides the following two relationships, one in terms of the input and output angles and the other in terms of the input and coupler angles:

$$f_1(\psi_2, \theta_4, k_1, k_2) = k_1 + k_2 \cos\theta_4 - k_3 \cos\psi_2 - cos(\theta_4 - \psi_2) = 0 \quad (3.17)$$

$$f_2(\psi_2, \theta_3, k_1', k_2') = k_1' - k_2' \cos\theta_3 - k_3' \cos\psi_2 + cos(\psi_2 - \theta_3) = 0 \quad (3.18)$$

where

$$k_1 = \frac{a_1^2 + {a_2'}^2 - a_3^2 + a_4^2}{2a_2' a_4} \quad (3.19)$$

$$k_2 = \frac{a_1}{a_2'} \quad (3.20)$$

$$k_3 = \frac{a_1}{a_4} \quad (3.21)$$

$$k_1' = \frac{a_1^2 + {a_2'}^2 + a_3^2 - a_4^2}{2a_2' a_3} \quad (3.22)$$

$$k_2' = \frac{a_1}{a_2'} \quad (3.23)$$

$$k_3' = \frac{a_1}{a_3} \quad (3.24)$$

It should be noted that the kinematic variables containing the term a_2', such as k_1, k_2, k_1' and k_2', vary with time, as the length of the actuated link varies due to the axial shortening.

Introducing an intermediate variable T, eqs.(3.17) and (3.18) take on the quadratic form given below:

$$AT^2 + 2BT + C = 0 \quad (3.25)$$

where

$$T \equiv \tan(\frac{\theta_4}{2}) \quad (3.26)$$

and

$$A = k_1 - k_2 + (1 - k_3)\cos\psi_2 \quad (3.27)$$

$$B = -\sin\psi_2 \quad (3.28)$$

$$C = k_1 + k_2 - (1 + k_3)\cos\psi_2 \quad (3.29)$$

From eq.(3.25), the output angle is derived as

$$\theta_4 = 2\tan^{-1}\left(\frac{-B + K\sqrt{B^2 - AC}}{A}\right) \tag{3.30}$$

where K is the branch index of the linkage configuration and is either -1 or 1.

Similarly, the coupler angle can be obtained as

$$\theta_3 = 2\tan^{-1}\left(\frac{-B' + K\sqrt{B'^2 - A'C'}}{A'}\right) \tag{3.31}$$

where

$$A' = k_1' + k_2' - (k_3' + 1)\cos\psi_2 \tag{3.32}$$

$$B' = \sin\psi_2 \tag{3.33}$$

$$C' = k_1' - k_2' - (k_3' - 1)\cos\psi_2 \tag{3.34}$$

with an appropriate selection of $T \equiv \tan(\frac{\theta_3}{2})$.

3.3.3 Joint Velocity Constraints

As a first step towards finding the unactuated joint velocities, the time derivative of the input-output relation, given in eq.(3.17), needs to be taken, namely,

$$\frac{df_1}{dt} = \frac{\partial f_1}{\partial \psi_2}\dot{\psi}_2 + \frac{\partial f_1}{\partial \theta_4}\dot{\theta}_4 + \frac{\partial f_1}{\partial k_1}\dot{k}_1 + \frac{\partial f_1}{\partial k_2}\dot{k}_2 = 0 \tag{3.35}$$

from which it is possible to solve for $\dot{\theta}_4$ by rearranging the terms as follows

$$\dot{\theta}_4 = -\frac{1}{\partial f_1/\partial \theta_4}\left(\frac{\partial f_1}{\partial \psi_2}\dot{\psi}_2 + \frac{\partial f_1}{\partial k_1}\dot{k}_1 + \frac{\partial f_1}{\partial k_2}\dot{k}_2\right) \tag{3.36}$$

In order to express the time-rate of change of the output angle as a function of the independent velocities, partial derivatives are taken with respect to the independent generalized coordinates. Differentiating eqs.(3.19) and (3.20) with respect to time gives

$$\dot{k}_1 = t_1\boldsymbol{\zeta}^T\dot{\mathbf{u}}_2'' \tag{3.37}$$

$$\dot{k}_2 = t_2\boldsymbol{\zeta}^T\dot{\mathbf{u}}_2'' \tag{3.38}$$

where

$$t_1 \equiv -\frac{1}{a_2'}\frac{\partial k_1}{\partial a_2'} = \frac{(a_1^2 + a_4^2) - (a_2'^2 + a_3^2)}{2a_4 a_2'^3} \tag{3.39}$$

$$t_2 \equiv -\frac{1}{a_2'}\frac{\partial k_2}{\partial a_2'} = \frac{a_1}{a_2'^3} \tag{3.40}$$

$$\boldsymbol{\zeta} \equiv -a_2'\frac{\partial a_2}{\partial \mathbf{u}_2''} = ((a_2\boldsymbol{\Upsilon}_2 - \boldsymbol{\Theta}_2) - \frac{1}{2}\boldsymbol{\Upsilon}_2\mathbf{u}''_2\,\mathbf{u}''^T_2\,\boldsymbol{\Upsilon}_2)^T\mathbf{u}''_2 \tag{3.41}$$

Moreover, the input angle defined in the ERLS can also be expressed as

$$\psi_2(t) = \theta_2(t) + \varphi_2(a_2, t) \tag{3.42}$$

where θ_2 is the angle of rotation of the input link and $\varphi_2(a_2, t)$ is the angle between its undeformed neutral axis and the line extending from the origin to the end-point, i.e., input link of the corresponding ERLS. Care must be taken in considering the latter, because it is not a joint angle, but an angle due to the link deflection, namely,

$$\varphi_2 = \tan^{-1}(\frac{u(a_2, t)}{a_2'}) \tag{3.43}$$

Upon differentiation of eq.(3.42), we obtain

$$\dot\psi_2(t) = \dot\theta_2(t) + \dot\varphi_2(a_2, t) \tag{3.44}$$

where

$$\dot\varphi_2(a_2, t) = \frac{(a_2 - s(a_2, t))\dot u(a_2, t) + u(a_2, t)\dot s(a_2, t)}{a_2'^2} \tag{3.45}$$

In the above equations, the terms containing the time-rate of either the transverse or axial displacement can be expressed as functions of the curvature vector using cubic splines, namely,

$$\dot u(a_2, t) = \boldsymbol{\epsilon}_2^T(a_2)\dot{\mathbf{u}}''_2 \tag{3.46}$$

$$\dot s(a_2, t) = \mathbf{u}''^T_2\,\boldsymbol{\Upsilon}_2\dot{\mathbf{u}}''_2 \tag{3.47}$$

where $\boldsymbol{\epsilon}_2(a_2) = \mathbf{s}_l(a_2)\,\boldsymbol{\Delta}_l^T$. Substituting eqs.(3.46) and (3.47) into eq.(3.45) leads to

$$\dot\varphi_2(a_2, t) = \boldsymbol{\eta}^T\dot{\mathbf{u}}''_2 \tag{3.48}$$

where

$$\eta = \frac{(a_2 - \frac{1}{2}\mathbf{u}''^T_2\ \mathbf{\Upsilon}_2\mathbf{u}'')\epsilon_2 + \mathbf{\Upsilon}^T_2\mathbf{u}''_2\ \mathbf{u}''^T_2\ \epsilon_2}{a_2^2 - \mathbf{u}''^T_2\left[a_2\mathbf{\Upsilon}_2 - \frac{1}{4}\mathbf{\Upsilon}^T_2\mathbf{u}''_2\ \mathbf{u}''^T_2\ \mathbf{\Upsilon}_2 - \mathbf{\Theta}_2\right]\mathbf{u}''_2} \tag{3.49}$$

Moreover, the partial derivatives in eq.(3.35) are computed as follows:

$$N_1 \equiv -\frac{\partial f_1}{\partial \theta_4} = k_2 \sin\theta_4 - \sin(\theta_4 - \psi_2) \tag{3.50}$$

$$N_2 \equiv \frac{\partial f_1}{\partial \psi_2} = k_3 \sin\psi_2 - \sin(\theta_4 - \psi_2) \tag{3.51}$$

$$N_3 \equiv \frac{\partial f_1}{\partial k_1} = 1 \tag{3.52}$$

$$N_4 \equiv \frac{\partial f_1}{\partial k_2} = \cos\theta_4 \tag{3.53}$$

Now eq.(3.36) can be rewritten as:

$$\dot{\theta}_4 = M_1\dot{\theta}_2 + \mathbf{m}_1^T\dot{\mathbf{u}}''_2 \tag{3.54}$$

where

$$M_1 = \frac{N_2}{N_1} \tag{3.55}$$

$$\mathbf{m}_1 = \frac{1}{N_1}((t_1 + t_2\cos\theta_4)\boldsymbol{\zeta} + N_2\boldsymbol{\eta}) \tag{3.56}$$

Similarly, the time-rate of change of the coupler angle can be obtained from the following equation:

$$\frac{df_2}{dt} = \frac{\partial f_2}{\partial \psi_2}\dot{\psi}_2 + \frac{\partial f_2}{\partial \theta_3}\dot{\theta}_3 + \frac{\partial f_2}{\partial k_1'}\dot{k}_1' + \frac{\partial f_2}{\partial k_2'}\dot{k}_2' = 0 \tag{3.57}$$

where the kinematic variables are given by

$$\dot{k}_1' = t_3\boldsymbol{\zeta}^T\dot{\mathbf{u}}''_2 \tag{3.58}$$

$$\dot{k}_2' = t_2\boldsymbol{\zeta}^T\dot{\mathbf{u}}''_2 \tag{3.59}$$

and

$$t_3 = \frac{(a_1^2 + a_3^2) - (a_2'^2 + a_4^2)}{2a_3a_2'^3} \tag{3.60}$$

In addition, the partial derivatives in eq.(3.57) are computed as follows:

$$N_1' \equiv -\frac{\partial f_2}{\partial \theta_3} = -k_2' \sin\theta_3 - \sin(\psi_2 - \theta_3) \tag{3.61}$$

$$N_2' \equiv \frac{\partial f_2}{\partial \psi_2} = k_3' \sin\psi_2 - \sin(\psi_2 - \theta_3) \tag{3.62}$$

$$N_3' \equiv \frac{\partial f_2}{\partial k_1'} = 1 \tag{3.63}$$

$$N_4' \equiv \frac{\partial f_2}{\partial k_2'} = -\cos\theta_3 \tag{3.64}$$

Hence, the final form of the time-rate of change of the coupler angle is given by

$$\dot{\theta}_3 = M_2\dot{\theta}_2 + \mathbf{m}_2^T\dot{\mathbf{u}}''_2 \tag{3.65}$$

where

$$M_2 = \frac{N_2'}{N_1'} \tag{3.66}$$

$$\mathbf{m}_2 = \frac{1}{N_1'}((t_3 - t_2\cos\theta_3)\boldsymbol{\zeta} + N_2'\boldsymbol{\eta}) \tag{3.67}$$

3.3.4 Velocity Constraints on Body-Fixed Frames

Let $\mathbf{r}_i$ be the position vector of any point P on link i, with respect to the moving frame $\mathcal{F}_i$ attached to the corresponding neutral axis, as shown in Fig. 3.5. Moreover, let us define $\mathbf{x}_i$ and $\mathbf{y}_i$ as the unit vectors parallel to axes X_i and Y_i, respectively, and let x and y be the coordinates of any point in the said frame. The position vector $\mathbf{r}_i$ of an arbitrary point of the ith link is then defined as

$$\mathbf{r}_i = (x - s(x,t))\mathbf{x}_i + u(x,t)\mathbf{y}_i \tag{3.68}$$

The position vector of any point P in the inertial frame, $\boldsymbol{\rho}_i$, can be expressed, in turn, as

$$\boldsymbol{\rho}_i = \mathbf{p}_i + \mathbf{r}_i, \;\; i = 2,3,4 \tag{3.69}$$

whose time-derivative is given by

$$\dot{\boldsymbol{\rho}}_i = \dot{\mathbf{p}}_i + \omega_i\mathbf{E}\mathbf{r}_i + \mathring{\mathbf{r}}_i, \;\; i = 2,3,4 \tag{3.70}$$

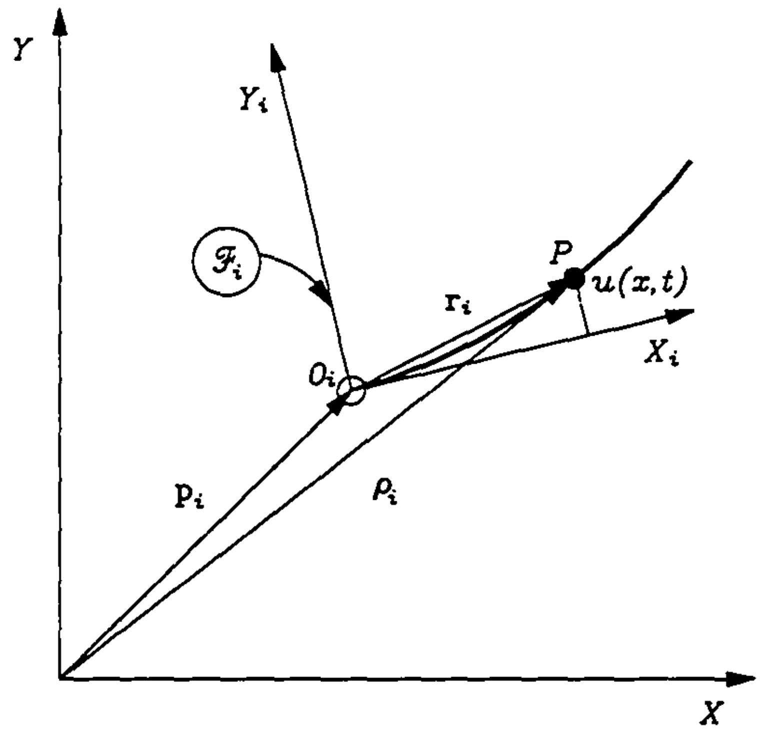

Figure 3.5: Position vector of a point on the link

with matrix $\mathbf{E}$ defined as

$$\mathbf{E} \equiv \begin{bmatrix} 0 & -1 \\ 1 & 0 \end{bmatrix} \tag{3.71}$$

In eq.(3.70), the scalars ω_i, for $i = 3, 4$, are obtained in eqs.(3.54) and (3.65), and $\overset{\circ}{(\cdot)}$ represents the time-derivative of $(\cdot)$ in frame $\mathcal{F}_i$ when regarding this frame fixed. In addition, $\mathbf{E}$ is an orthogonal matrix that rotates 2-dimensional vectors counterclockwise through an angle of 90°, and hence, $\mathbf{E}^T = -\mathbf{E}$ and $\mathbf{E}^T\mathbf{E} = \mathbf{1}$ with $\mathbf{1}$ denoting the 2×2 identity matrix.

Having considered that the transverse and axial displacements are due to the link flexibility and the geometric shortening, respectively, and that their time-rates of change are explicitly expressed in terms of curvatures along the link, the m-dimensional vector of generalized coordinates and speeds for the ith link can be defined as

$$\mathbf{q}_i \equiv [\mathbf{p}_i^T \;\; \theta_i \;\; \mathbf{u}''^T_i]^T \tag{3.72}$$

$$\dot{\mathbf{q}}_i \equiv [\dot{\mathbf{p}}_i^T \ \ \omega_i \ \ \dot{\mathbf{u}}''^T_i]^T \tag{3.73}$$

where $\mathbf{p}_i$ denotes the position vector of the origin O_i for link i, while θ_i and ω_i denote the angle measured from the inertial frame and its time-derivative. Moreover, $\mathbf{u}''_i$ denotes the l-dimensional curvature vector, where l depends on the imposed boundary condition and the number of nodal points. The vector of *generalized speeds* of the mechanism is then defined as

$$\dot{\mathbf{q}} = [\dot{\mathbf{q}}_2^T \ \ \dot{\mathbf{q}}_3^T \ \ \dot{\mathbf{q}}_4^T]^T \tag{3.74}$$

The forgoing vector can be expressed as a function of the r-dimensional *independent generalized speeds*, namely,

$$\dot{\mathbf{q}} = \mathbf{N}(\mathbf{q})\mathbf{v} \tag{3.75}$$

where $\mathbf{N}(\mathbf{q})$ is an $N \times r$ sparse matrix with $N = 3m$. Moreover, for the given mechanism, the r-dimensional vector of independent generalized speeds is defined as

$$\mathbf{v} = [\dot{\theta}_2 \ \ \dot{\mathbf{u}}''^T_2 \ \ \dot{\mathbf{u}}''^T_3 \ \ \dot{\mathbf{u}}''^T_4]^T \tag{3.76}$$

3.3.5 Introduction of the Natural Orthogonal Complement

On the other hand, the kinematic velocity constraints produced by eqs.(3.54), (3.65) and (3.70) can be written in terms of the generalized speeds as

$$\mathbf{A}\dot{\mathbf{q}} = \mathbf{0}_s \tag{3.77}$$

where $\mathbf{A} = \mathbf{A}(\mathbf{q}, t)$ is an $s \times N$ matrix with $s < N$, and $\mathbf{0}_s$ is the s-dimensional zero vector. Moreover, let q be the rank of matrix $\mathbf{A}$. Then, the degree of freedom of the system, denoted by r, is

$$r = N - q \tag{3.78}$$

Substitution of eq.(3.75) into eq.(3.77) leads to

$$\mathbf{A}\mathbf{N}\mathbf{v} = \mathbf{0}_s \tag{3.79}$$

Since $\mathbf{v}$ is r-dimensional and its components are linearly independent, eq.(3.79) holds if and only if

$$\mathbf{AN} = \mathbf{O}_{sr} \tag{3.80}$$

This shows that $\mathbf{N}$ is an $N \times r$ *orthogonal complement* of $\mathbf{A}$, where $\mathbf{O}_{sr}$ is the $s \times r$ zero matrix. Because of the form in which $\mathbf{N}$ is defined, it is termed the *natural orthogonal complement* of $\mathbf{A}$.

Chapter 4

Dynamics Formulation with the NOC

4.1 Introduction

In order to derive the dynamic equations of a mechanism modelled as a chain of flexible elements, two methods are systematically integrated: the natural orthogonal complement (NOC) and cubic splines. The former allows the dynamic equations of the mechanical system to be formulated without using Lagrange multipliers, whereas the latter allows the elastic motions associated with structural members to be described with a finite number of generalized coordinates. The proposed approach takes into account mutual couplings between the rigid-body and elastic motions in its formulation. Furthermore, the equations of motion are expressed in terms of the minimum number of generalized coordinates, i.e., the degree of freedom of the given system.

The approach taken in this section can be summarized as follows:

1. Expressions for the kinetic and potential energies, as well as the Rayleigh dissipation function are constructed for each link, which is considered as an unconstrained body.
2. These expressions are then spatially discretized along the link using the cubic spline technique, so that the set of elastic coordinates is finite.
3. The rigid-body motions are expressed using a set of dependent generalized

coordinates, as needed to locate and orient each unconstrained body in space.

4. The equations of motion for each individual unconstrained link are formulated using Lagrange's equations. It should be recognized that the corresponding coordinate system includes both independent and dependent generalized coordinates. The dependent coordinates arise from the coupling of each intermediate link with its neighbours and the constraints due to the loop-closure.

5. The resulting equations are assembled for the entire system to constitute the decoupled equations of motion. This formulation inevitably brings forth the nonworking constraint forces in conjunction with the dependent generalized coordinates.

6. By virtue of the natural orthogonal complement, the nonworking constraint forces are eliminated and the coupled equations of motion expressed in terms of a minimum number of generalized coordinates are derived.

The dynamic formulation of a rotating flexible beam will be presented in detail at the end of this chapter. To describe the vibrational behaviour arising due to link flexibility, two spatial discretization methods are considered: the normal-mode method and the cubic-spline technique. The corresponding couplings between the rigid-body and the elastic motions are then examined in terms of their physical significance. Finally, the resulting dynamic models are then used to discuss the robustness of the different spatial discretization methods.

4.2 Dynamic Modelling of the Mechanism

The mechanical system considered throughout the first half of this chapter is a planar four-bar linkage of the crank-rocker type. It is driven by a constant angular velocity input that produces a high acceleration of the output link during a part of its motion cycle. Since the mechanism performs its motion in the horizontal plane, gravity is not considered in the formulation. It should be pointed out that transverse vibration results not only from link flexibility but also from the singularities of the mechanism at hand. The effect of singularities will be extensively discussed with the experimental results in a later chapter.

The kinetic and potential energies for link i, denoted by T_i and V_i respectively, and the Rayleigh dissipation function due to the structural damping of link i, denoted by D_i, are given by

$$T_i = \frac{1}{2}\int_0^{a_i} m_i(x)\dot{\boldsymbol{\rho}}_i^T\dot{\boldsymbol{\rho}}_i dx \tag{4.1}$$

$$V_i = \frac{1}{2}\int_0^{a_i} EI_i(x)[u_{xx}(x,t)]^2 dx \tag{4.2}$$

$$D_i = \frac{1}{2}\int_0^{a_i} c_i[u_{xt}(x,t)]^2 dx \tag{4.3}$$

where $m_i(x)$ and $EI_i(x)$ denote the mass per unit length and the flexural rigidity of link i, respectively. In addition, c_i is the structural damping coefficient of link i, $u_{xx}(x,t)$ denotes $\partial^2 u/\partial x^2$ and $u_{xt}(x,t)$ denotes $\partial^2 u/\partial x \partial t$.

The term $\dot{\boldsymbol{\rho}}_i^T\dot{\boldsymbol{\rho}}_i$ in eq.(4.1) can be determined using the velocity constraints, given in eq.(3.70), namely,

$$\begin{aligned} \dot{\boldsymbol{\rho}}_i^2 = \; & \dot{\mathbf{p}}_i^2 + 2\omega_i\dot{\mathbf{p}}_i^T\mathbf{E}\mathbf{r}_i + 2\dot{\mathbf{p}}_i^T\mathring{\mathbf{r}}_i \\ & -2\omega_i\mathbf{r}_i^T\mathbf{E}\mathring{\mathbf{r}}_i + \omega_i^2\mathbf{r}_i^2 + \mathring{\mathbf{r}}_i^2 \end{aligned} \tag{4.4}$$

where $\mathring{\mathbf{r}}_i$ denotes the time-derivative of the position vector $\mathbf{r}_i$ in its own frame, regarding this frame as fixed.

Upon substituting eq.(4.4) into eq.(4.1) and performing an integration over the link, one obtains the resulting kinetic energy. This task is difficult to implement due to the intrinsic nature of the distributed-parameter system and the fact that the link undergoes axial displacement due to the geometric stiffening.

4.2.1 Kinetic and Potential Energies for a Clamped-Free Beam

When considering a link with clamped-free boundary conditions, it is no longer valid to assume that the link length remains constant, especially at higher operating speeds. Consequently, the kinetic energy must account for both the axial displacement due to geometric stiffening and the transverse translation due to bending. Since the clamped-free boundary conditions are applied to the input link of the mechanism, the kinetic energy of the input link is constructed taking centrifugal stiffening into account.

Considering the time-rate of change of the position vector $\boldsymbol{\rho}_2$, given in eq.(3.70), the square of its magnitude, $\|\dot{\boldsymbol{\rho}}_2\|^2 \equiv \dot{\boldsymbol{\rho}}_2^T\,\dot{\boldsymbol{\rho}}_2$, in the case of the input link, becomes

$$\dot{\boldsymbol{\rho}}_2^2 = \omega_2^2\mathbf{r}_2^2 - 2\omega_2\mathbf{r}_2^T\mathbf{E}\mathring{\mathbf{r}}_2 + \mathring{\mathbf{r}}_2^2 \tag{4.5}$$

$$= (x^2 - 2xs + s^2 + u^2)\omega_2^2 + 2(u\dot{s} + x\dot{u} - s\dot{u})\omega_2 + (\dot{s}^2 + \dot{u}^2) \tag{4.6}$$

Upon substitution of eq.(4.6) into the kinetic energy expression, given in eq.(4.1), we obtain

$$T_2 = \tfrac{1}{2}\int_0^{a_2} m_2(x) \quad \begin{aligned}&((x^2 - 2xs + s^2 + u^2)\omega_2^2 \\ &+2(u\dot{s} + x\dot{u} - s\dot{u})\omega_2 + (\dot{s}^2 + \dot{u}^2))\,dx\end{aligned} \tag{4.7}$$

The foregoing equation is then spatially discretized along the link by using the cubic spline technique to describe the displacement function in terms of the curvatures at the supporting points, namely,

$$T_2 = \tfrac{1}{2}\sum_{j=1}^{n-1}\int_{x_j}^{x_{j+1}} m_2(x) \quad \begin{aligned}&((x^2 - 2xs + s^2 + u^2)\omega_2^2 \\ &+2(u\dot{s} + x\dot{u} - s\dot{u})\omega_2 + (\dot{s}^2 + \dot{u}^2))\,dx\end{aligned} \tag{4.8}$$

In this way, the axial displacement due to the centrifugal stiffening can be efficiently determined in the framework of the cubic spline technique.

The axial displacement function can be written in the following form:

$$s(x,t) = \frac{1}{2}\int_0^x \left(\frac{\partial u}{\partial x}\right)^2 dx \tag{4.9}$$

i.e.,

$$s(x,t) = \frac{1}{2}\mathbf{u}''^T_2 \left(\sum_{k=1}^{j-1} \left(\mathbf{\Delta}_k^T \int_{x_k}^{x_{k+1}} \mathbf{F}'_k(x)dx \; \mathbf{\Delta}_k \right) + \mathbf{\Delta}_j^T \int_{x_j}^{x} \mathbf{F}'_j(x)dx \; \mathbf{\Delta}_j \right) \mathbf{u}''_2 \quad (4.10)$$

where x lies in the interval $x_j \leq x \leq x_{j+1}$. To reduce the computational complexity, the axial displacement between two adjacent supporting points is assumed to be constant. Such an assumption, however, does not affect the evaluation of the axial displacement at the proximal end with which the kinematic properties are obtained, as discussed in the previous chapter. This is so because the end tip is located exactly on the supporting point. Hence,

$$s(x,t) = \frac{1}{2}\mathbf{u}''^T_2 \left(\sum_{k=1}^{j-1} \mathbf{\Upsilon}_k \right) \mathbf{u}''_2 \quad (4.11)$$

where

$$\mathbf{\Upsilon}_k = \mathbf{\Delta}_k^T \int_{x_k}^{x_{k+1}} \mathbf{F}'_k(x)dx \; \mathbf{\Delta}_k \quad (4.12)$$

and

$$\mathbf{F}'_k(x) \equiv \frac{\partial \mathbf{s}_k(x)}{\partial x} \frac{\partial \mathbf{s}_k^T(x)}{\partial x} \quad (4.13)$$

Furthermore, the isoparametric beam element enables the kinetic energy to have the form given below:

$$T_2 = \frac{1}{2}(\gamma_1 - \gamma_2 + \gamma_3 + \gamma_4)\omega_2^2 + 2\omega_2(\boldsymbol{\gamma}_1^T + \boldsymbol{\gamma}_2^T - \boldsymbol{\gamma}_3^T)\dot{\mathbf{u}}''_2 + \dot{\mathbf{u}}''^T_2 \, (\mathbf{\Gamma}_1 + \mathbf{\Gamma}_2)\dot{\mathbf{u}}''_2 \quad (4.14)$$

The coefficients of the foregoing equation are given in Table 4.1, where the first column shows the expression for the kinetic energy segment in terms of continuous spatial variables, whereas the second column shows the spatially discretized kinetic energy expression for a segment excluding spatial coordinates.

Finally, the kinetic energy of the input link can be written as

$$T_2 = \frac{1}{2}\dot{\mathbf{q}}_2^T \, \mathbf{M}_2 \, \dot{\mathbf{q}}_2 \quad (4.15)$$

Table 4.1: Evaluation of the kinetic energy under the clamped-free boundary conditions

	Continuous	Discretized
γ_1	$\int_0^{a_2} m_2(x)x^2dx$	$\frac{1}{3}m_2a_2^3$
γ_2	$2\int_0^{a_2} m_2(x)xs\,dx$	$m_2\mathbf{u}''^T_2\left(\sum_{j=1}^{n-1}\frac{x_{j+1}^2-x_j^2}{2}\left(\sum_{k=1}^{j-1}\boldsymbol{\Upsilon}_k\right)\right)\mathbf{u}''_2$
γ_3	$\int_0^{a_2} m_2(x)s^2dx$	$m_2\mathbf{u}''^T_2\sum_{j=1}^{n-1}\left(\frac{x_{j+1}-x_j}{4}\left(\sum_{k=1}^{j-1}\boldsymbol{\Upsilon}_k\right)\mathbf{u}''_2\,\mathbf{u}''^T_2\left(\sum_{k=1}^{j-1}\boldsymbol{\Upsilon}_k\right)\right)\mathbf{u}''_2$
γ_4	$\int_0^{a_2} m_2(x)u^2dx$	$m_2\mathbf{u}''^T_2\left(\sum_{j=1}^{n-1}\boldsymbol{\Delta}_j^T\int_{x_j}^{x_{j+1}}\mathbf{F}_j(x)dx\,\boldsymbol{\Delta}_j\right)\mathbf{u}''_2$
$\boldsymbol{\gamma}_1$	$\int_0^{a_2} m_2(x)u\dot{s}dx$	$m_2\sum_{j=1}^{n-1}\left(\left(\int_{x_j}^{x_{j+1}}\mathbf{s}_j^T(x)dx\right)\boldsymbol{\Delta}_j\mathbf{u}''_2\,\mathbf{u}''^T_2\left(\sum_{k=1}^{j-1}\boldsymbol{\Upsilon}_k\right)\right)^T$
$\boldsymbol{\gamma}_2$	$\int_0^{a_2} m_2(x)x\dot{u}dx$	$m_2\sum_{j=1}^{n-1}\boldsymbol{\Delta}_j^T\left(\int_{x_j}^{x_{j+1}}x\mathbf{s}_j(x)dx\right)$
$\boldsymbol{\gamma}_3$	$\int_0^{a_2} m_2(x)s\dot{u}dx$	$\frac{1}{2}m_2\sum_{j=1}^{n-1}\left(\left(\sum_{k=1}^{j-1}\boldsymbol{\Upsilon}_k\right)\mathbf{u}''_2\int_{x_j}^{x_{j+1}}\mathbf{s}_j^T(x)dx\,\boldsymbol{\Delta}_j\right)^T\mathbf{u}''_2$
$\boldsymbol{\Gamma}_1$	$\int_0^{a_2} m_2(x)\dot{s}^2dx$	$m_2\sum_{j=1}^{n-1}\left((x_{j+1}-x_j)\left(\sum_{k=1}^{j-1}\boldsymbol{\Upsilon}_k\right)\mathbf{u}''_2\,\mathbf{u}''^T_2\left(\sum_{k=1}^{j-1}\boldsymbol{\Upsilon}_k\right)\right)$
$\boldsymbol{\Gamma}_2$	$\int_0^{a_2} m_2(x)\dot{u}^2dx$	$m_2\left(\sum_{j=1}^{n-1}\boldsymbol{\Delta}_j^T\int_{x_j}^{x_{j+1}}\mathbf{F}_j(x)dx\,\boldsymbol{\Delta}_j\right)$

where

$$\mathbf{M}_2 = \begin{bmatrix} \gamma & \gamma^T \\ \gamma & \mathbf{\Gamma} \end{bmatrix} \tag{4.16}$$

and

$$\gamma \equiv \gamma_1 - \gamma_2 + \gamma_3 + \gamma_4 \tag{4.17}$$

$$\gamma \equiv \gamma_1 + \gamma_2 - \gamma_3 \tag{4.18}$$

$$\mathbf{\Gamma} \equiv \mathbf{\Gamma}_1 + \mathbf{\Gamma}_2 \tag{4.19}$$

In eq.(4.16) $\mathbf{M}_2$ is an $m \times m$ symmetric positive-definite matrix, where m denotes the number of generalized coordinates with which both rigid-body and elastic motions are defined. The number m varies with the number of supporting points, as well as the number of rigid-body coordinates.

The potential energy, in turn, is given by

$$V_2 = \frac{1}{2}\int_0^{a_2} EI(x)\left(u''(x,t)\right)^2 dx \tag{4.20}$$

After spatially disretizing the foregoing equation and substituting the spatial variables by the cubic spline forms, one obtains

$$V_2 = \frac{1}{2}\mathbf{u''}_2^T \left(\sum_{k=1}^{n-1} \mathbf{\Delta}_j^T \int_{x_j}^{x_j+1} EI(x)\mathbf{F}_j''(x)dx\ \mathbf{\Delta}_j\right)\mathbf{u''}_2 \tag{4.21}$$

where

$$\mathbf{F}_j'' = \frac{\partial^2 \mathbf{s}_j(x)}{\partial x^2}\frac{\partial^2 \mathbf{s}_j^T(x)}{\partial x^2} \tag{4.22}$$

The potential energy can also be written as

$$V_2 = \frac{1}{2}\mathbf{q}_2^T\, \mathbf{K}_2\, \mathbf{q}_2 \tag{4.23}$$

where

$$\mathbf{K}_2 = \begin{bmatrix} 0 & \mathbf{0}^T \\ \mathbf{0} & \mathbf{\Omega}_2 \end{bmatrix} \tag{4.24}$$

and $\mathbf{0}$ is the $(n-1)$-dimensional zero vector. In addition, the $(n-1)\times(n-1)$ stiffness matrix associated with the elastic coordinates Ω_2 is defined as

$$\Omega_2 = \sum_{k=1}^{n-1} \mathbf{\Delta}_j^T \left(\int_{x_j}^{x_{j+1}} EI(x)\mathbf{F}_j''(x)dx \right) \mathbf{\Delta}_j \tag{4.25}$$

Likewise, the Rayleigh dissipation function due to structural damping can be written as

$$D_2 = \frac{1}{2} c_2 \dot{\mathbf{u}}''^T_2 \left(\sum_{j=1}^{n-1} \mathbf{\Delta}_j^T \int_{x_j}^{x_{j+1}} \mathbf{F}_j'(x)dx \; \mathbf{\Delta}_j \right) \dot{\mathbf{u}}''_2 \tag{4.26}$$

where

$$\mathbf{F}_j'(x) = \frac{\partial \mathbf{s}_j(x)}{\partial x} \frac{\partial \mathbf{s}_j^T(x)}{\partial x} \tag{4.27}$$

Then,

$$D_2 = \frac{1}{2} \dot{\mathbf{q}}_2^T \, \mathbf{D}_2 \, \dot{\mathbf{q}}_2 \tag{4.28}$$

where

$$\mathbf{D}_2 = \begin{bmatrix} 0 & \mathbf{0}^T \\ \mathbf{0} & \Lambda_2 \end{bmatrix} \tag{4.29}$$

In the above equation, the $(n-1)\times(n-1)$ damping matrix arising form the structural damping of the flexible element is defined as

$$\Lambda_2 = c_2 \sum_{j=1}^{n-1} \mathbf{\Delta}_j^T \int_{x_j}^{x_{j+1}} \mathbf{F}_j'(x)dx \; \mathbf{\Delta}_j \tag{4.30}$$

4.2.2 Kinetic and Potential Energies for a Pinned-Pinned Beam

The kinetic energy of a link with pinned-pinned boundary conditions takes a rather simple form because the link length remains constant. Since the coupler and follower links of the four-bar mechanism are modelled with the pinned-pinned boundary conditions, the kinetic energies of these two links are derived with the same formulation.

The kinetic energies, for $i = 3, 4$, are given by

$$T_i = \frac{1}{2} \int_0^{a_i} m_i(x) \left(\dot{\mathbf{p}}_i^2 + 2\omega_i \dot{\mathbf{p}}_i^T \mathbf{E} \mathbf{r}_i + 2\dot{\mathbf{p}}_i^T \mathring{\mathbf{r}}_i - 2\omega_i \mathbf{r}_i^T \mathbf{E} \mathring{\mathbf{r}}_i + \omega_i^2 \mathbf{r}_i^2 + \mathring{\mathbf{r}}_i^2 \right) dx \tag{4.31}$$

Using the cubic-spline technique, the foregoing equations can be expressed as

$$\begin{aligned} T_i = \; & \tfrac{1}{2}(\gamma_1\, \dot{\mathbf{p}}_i^T \mathbf{1} \dot{\mathbf{p}}_i + 2\, \dot{\mathbf{p}}_i^T \boldsymbol{\gamma}_1 \omega_i + 2\, \dot{\mathbf{p}}_i^T \boldsymbol{\Gamma}_1 \dot{\mathbf{u}}''_i \\ & -2\, \omega_i\, \boldsymbol{\gamma}_2^T \dot{\mathbf{u}}''_i + \gamma_2\, \omega_i^2 + \dot{\mathbf{u}}''^T_i\, \boldsymbol{\Gamma}_2 \dot{\mathbf{u}}''_i) \end{aligned} \tag{4.32}$$

where the coefficients are given in Table 4.2.

The kinetic energy expression can then be put in the form

$$T_i = \frac{1}{2} \dot{\mathbf{q}}_i^T\, \mathbf{M}_i\, \dot{\mathbf{q}}_i \tag{4.33}$$

where

$$\mathbf{M}_i = \begin{bmatrix} \gamma_1 \mathbf{1} & \boldsymbol{\gamma}_1 & \boldsymbol{\Gamma}_1 \\ \boldsymbol{\gamma}_1^T & \gamma_2 & \boldsymbol{\gamma}_2^T \\ \boldsymbol{\Gamma}_1^T & \boldsymbol{\gamma}_2 & \boldsymbol{\Gamma}_2 \end{bmatrix} \tag{4.34}$$

in which

$$\begin{aligned} &\boldsymbol{\gamma}_1 \in I\!R^{2\times 1} && \boldsymbol{\gamma}_2 \in I\!R^{(n-2)\times 1} \\ &\boldsymbol{\Gamma}_1 \in I\!R^{2\times(n-2)} && \boldsymbol{\Gamma}_1 \in I\!R^{(n-2)\times(n-2)} \end{aligned}$$

In addition, $\mathbf{1}$ is the 2×2 identity matrix. Hence, the foregoing mass matrix is of $m \times m$ and is symmetric and positive-definite. As shown in the foregoing formulation, the couplings between the rigid-body and the elastic motions are fully considered.

The potential energy and the Rayleigh dissipation function are readily obtained as

$$V_i = \frac{1}{2} \mathbf{q}_i^T\, \mathbf{K}_i\, \mathbf{q}_i \tag{4.35}$$

$$D_i = \frac{1}{2} \dot{\mathbf{q}}_i^T\, \mathbf{D}_i\, \dot{\mathbf{q}}_i \tag{4.36}$$

where

$$\mathbf{K}_i = \begin{bmatrix} \mathbf{O}_{b\times b} & \mathbf{O}_{b\times(n-2)} \\ \mathbf{O}_{(n-2)\times b} & \boldsymbol{\Omega}_i \end{bmatrix} \in I\!R^{m\times m} \tag{4.37}$$

$$\mathbf{D}_i = \begin{bmatrix} \mathbf{O}_{b\times b} & \mathbf{O}_{b\times(n-2)} \\ \mathbf{O}_{(n-2)\times b} & \boldsymbol{\Lambda}_i \end{bmatrix} \in I\!R^{m\times m} \tag{4.38}$$

(4.39)

Table 4.2: Evaluation of the kinetic energy under the pinned-pinned boundary conditions

	Continuous	Discretized
γ_1	$\int_0^{a_i} m_i(x)dx$	$m_i a_i$
γ_2	$\int_0^{a_i} m_i(x)(x^2+u^2)dx$	$m_i\left(\frac{a_i^3}{3}+\mathbf{u}''^T_i\left(\sum_{j=1}^{n-2}\boldsymbol{\Delta}_j^T\int_{x_j}^{x_{j+1}}\mathbf{F}_j(x)dx\ \boldsymbol{\Delta}_j\right)\mathbf{u}''_i\right)$
γ_1	$\int_0^{a_i} m_i(x)\begin{bmatrix}-u\\ x\end{bmatrix}dx$	$m_i\sum_{j=1}^{n-2}\begin{bmatrix}-\int_{x_j}^{x_{j+1}}\mathbf{s}_j^T\boldsymbol{\Delta}_j dx\ \mathbf{u}''_i\\ \frac{x_{j+1}^2-x_j^2}{2}\end{bmatrix}$
γ_2	$\int_0^{a_i} m_i(x)x\dot{u}dx$	$m_i\sum_{j=1}^{n-2}\left(\int_{x_j}^{x_{j+1}} x\mathbf{s}_j^T(x)\boldsymbol{\Delta}_j dx\right)^T$
Γ_1	$\begin{bmatrix}0\\ 1\end{bmatrix}\int_0^{a_i} m_i(x)\dot{u}dx$	$m_i\begin{bmatrix}0\\ 1\end{bmatrix}\sum_{j=1}^{n-2}\left(\int_{x_j}^{x_{j+1}}\mathbf{s}_j^T(x)\mathbf{C}_j dx\right)$
Γ_2	$\int_0^{a_i} m_i(x)\dot{u}^2dx$	$m_i\sum_{j=1}^{n-2}\left(\int_{x_j}^{x_{j+1}}\boldsymbol{\Delta}_j^T\mathbf{F}_j(x)\boldsymbol{\Delta}_j dx\right)$

where b denotes the number of rigid-body coordinates. The stiffness and damping sub-matrices associated with the elastic motion are defined as

$$\Omega_i = \sum_{k=1}^{n-2} \Delta_j^T \int_{x_j}^{x_j+1} EI(x)\mathbf{F}_j''(x)dx\ \Delta_j^T \in I\!R^{(n-2)\times(n-2)} \tag{4.40}$$

$$\Lambda_i = c_i \sum_{j=1}^{n-2} \Delta_j^T \int_{x_j}^{x_j+1} \mathbf{F}_j'(x)dx\ \Delta_j \in I\!R^{(n-2)\times(n-2)} \tag{4.41}$$

4.2.3 Dynamic Formulation for an Unconstrained Link

The dynamics equations are then derived for link i using Lagrange's equation, as shown below:

$$\frac{d}{dt}\left(\frac{\partial T_i}{\partial \dot{\mathbf{q}}_i}\right) - \frac{\partial T_i}{\partial \mathbf{q}_i} = \mathbf{w}_i^E + \mathbf{w}_i^C - \frac{\partial V_i}{\partial q_i} - \frac{\partial D_i}{\partial \dot{\mathbf{q}}_i} \tag{4.42}$$

where $\mathbf{w}_i^E$ and $\mathbf{w}_i^C$ represent the vectors of *external* and *kinematic constraint* forces, respectively. The equations of motion for each separate link then become

$$\mathbf{M}_i\ddot{\mathbf{q}}_i + \mathbf{C}_i\dot{\mathbf{q}}_i + \mathbf{K}_i\mathbf{q}_i = \mathbf{w}_i \quad (i = 2, 3, 4) \tag{4.43}$$

where the vector of generalized forces is defined as $\mathbf{w}_i \equiv \mathbf{w}_i^E + \mathbf{w}_i^C$, and

$$\mathbf{C}_i \equiv \dot{\mathbf{M}}_i + \mathbf{D}_i - \mathbf{\Phi}_i \tag{4.44}$$

$$\mathbf{\Phi}_i \equiv \frac{1}{2}\left[\frac{\partial(\mathbf{M}_i\dot{\mathbf{q}}_i)}{\partial \mathbf{q}_i}\right]^T \tag{4.45}$$

4.2.4 Decoupled Equations of Motion

After assembling the foregoing equations for the entire mechanism, the decoupled equations of motion take the form

$$\mathbf{M}\ddot{\mathbf{q}} + \mathbf{C}\dot{\mathbf{q}} + \mathbf{K}\mathbf{q} = \mathbf{w} \tag{4.46}$$

where

$$\mathbf{M} = \mathrm{diag}(\mathbf{M}_2, \mathbf{M}_3, \mathbf{M}_4) \tag{4.47}$$

$$\mathbf{K} = \mathrm{diag}(\mathbf{K}_2, \mathbf{K}_3, \mathbf{K}_4) \tag{4.48}$$

$$\mathbf{C} = \mathrm{diag}(\mathbf{C}_2, \mathbf{C}_3, \mathbf{C}_4) \tag{4.49}$$

$$\mathbf{w} = [\mathbf{w}_2^T \ \ \mathbf{w}_3^T \ \ \mathbf{w}_4^T]^T \tag{4.50}$$

Let us now define the state-variable vector $\mathbf{x}$ as

$$\mathbf{x} = [\mathbf{q}^T \ \ \dot{\mathbf{q}}^T]^T \tag{4.51}$$

and the state-variable vector associated with only the elastic motion $\mathbf{u}''$ as

$$\mathbf{u}''^T \equiv [\mathbf{u}''^T_2 \ \ \mathbf{u}''^T_3 \ \ \mathbf{u}''^T_4] \tag{4.52}$$

The equations of motion then take the state-space representation below:

$$\dot{\mathbf{x}}(t) = \mathbf{A}(\mathbf{u}'', \dot{\mathbf{u}}'')\mathbf{x}(t) + \mathbf{B}(\mathbf{u}'')\mathbf{w}(t) \tag{4.53}$$

with $\mathbf{A}(\mathbf{u}'', t)$ and $\mathbf{B}(\mathbf{u}'', t)$ defined as

$$\mathbf{A} \equiv \begin{bmatrix} \mathbf{O}_N & \mathbf{I}_N \\ -\mathbf{M}^{-1}\mathbf{K} & -\mathbf{M}^{-1}\mathbf{C} \end{bmatrix} \tag{4.54}$$

$$\mathbf{B} \equiv \begin{bmatrix} \mathbf{O}_{Np} \\ \mathbf{M}^{-1}\mathbf{P} \end{bmatrix} \tag{4.55}$$

It should be noted that $\mathbf{P}$ is a $N \times p$ permutation matrix whose nonzero element in each column designates the presence of either an associated constraint force or an external force. Moreover, p denotes the number of generalized coordinates associated with the rigid-body motion, while $\mathbf{I}_N$ and $\mathbf{O}_N$ are the $N \times N$ identity and zero matrices, respectively. In addition, $\mathbf{O}_{Np}$ is the $N \times p$ zero matrix.

4.2.5 Coupled Equations of Motion

Let us define the state-variable vector $\mathbf{z}$ in terms of the independent generalized coordinates and their first time-derivatives, namely,

$$\mathbf{z} \equiv \begin{bmatrix} \boldsymbol{\phi} \\ \dot{\boldsymbol{\phi}} \end{bmatrix} \equiv \begin{bmatrix} \boldsymbol{\phi} \\ \mathbf{v} \end{bmatrix} \tag{4.56}$$

The coupled equations of motion in terms of the minimum number of generalized coordinates are obtained by first differentiating eq.(3.75), namely,

$$\ddot{\mathbf{q}} = \dot{\mathbf{N}}\mathbf{v} + \mathbf{N}\dot{\mathbf{v}} \tag{4.57}$$

and then substituting the above equation into eq.(4.46), thus obtaining

$$\mathbf{M}\mathbf{N}\dot{\mathbf{v}} + (\mathbf{M}\dot{\mathbf{N}} + \mathbf{C}\mathbf{N})\mathbf{v} + \mathbf{K}\mathbf{q} = \mathbf{w} \tag{4.58}$$

Note that $\mathbf{K}$, as defined in eq.(4.48), consists of the stiffness matrices associated with the flexible coordinates of each link and the zero matrices associated with the rigid-body coordinates.

Moreover, the power Π developed by the constraint forces $\mathbf{w}^C$ must vanish by definition, i.e.,

$$\Pi = \dot{\mathbf{q}}^T\mathbf{w}^C = \mathbf{v}^T\mathbf{N}^T\mathbf{w}^C = 0 \tag{4.59}$$

and, since all the components of $\mathbf{v}$ are linearly independent, we must have

$$\mathbf{N}^T\mathbf{w}^C = \mathbf{0}_r \tag{4.60}$$

Pre-multiplying by $\mathbf{N}^T$ both sides of eq.(4.58) now gives

$$\mathbf{M}''\dot{\mathbf{v}} + \mathbf{C}''\mathbf{v} + \mathbf{K}''\boldsymbol{\phi} = \boldsymbol{\tau} \tag{4.61}$$

where

$$\boldsymbol{\tau} \equiv \mathbf{N}^T\mathbf{w}^E \tag{4.62}$$

with $\boldsymbol{\tau}$ being the vector of generalized applied torques and

$$\mathbf{M}'' \equiv \mathbf{N}^T\mathbf{M}\mathbf{N} \tag{4.63}$$

$$\mathbf{C}'' \equiv \mathbf{N}^T(\mathbf{M}\dot{\mathbf{N}} + \mathbf{C}\mathbf{N}) \tag{4.64}$$

$$\mathbf{K}'' \equiv \mathbf{N}^T\mathbf{K}\mathbf{N} \equiv \boldsymbol{\Omega} \tag{4.65}$$

where

$$\boldsymbol{\Omega} = \text{diag}[\mathbf{K}_2 \;\; \boldsymbol{\Omega}_3 \;\; \boldsymbol{\Omega}_4] \tag{4.66}$$

It should be recognized that the constraint forces are eliminated by virtue of eq.(4.60).

The foregoing coupled equations of motion can be expressed in state-space form as

$$\dot{\mathbf{z}}(t) = \boldsymbol{\Phi}(\mathbf{z}, t)\mathbf{z}(t) + \boldsymbol{\mu}(\mathbf{z}, t)\tau(t) \tag{4.67}$$

where

$$\boldsymbol{\Phi} \equiv \begin{bmatrix} \mathbf{O}_r & \mathbf{I}_r \\ -\mathbf{M}''^{-1}\mathbf{K}'' & -\mathbf{M}''^{-1}\mathbf{C}'' \end{bmatrix}$$

$$\boldsymbol{\mu} \equiv \begin{bmatrix} \mathbf{0}_r \\ \mathbf{M}''^{-1}\mathbf{p} \end{bmatrix}$$

with $\mathbf{p}$ being the permutation vector whose nonzero component designates the presence of the generalized applied force, while $\mathbf{I}_r$ and $\mathbf{O}_r$ are the $r \times r$ identity and zero matrices, respectively. Moreover, $\mathbf{0}_r$ is the r-dimensional zero vector.

4.3 Dynamic Formulation of a Rotating Beam

4.3.1 Problem Formulation

In this section, the dynamic model of a rotating beam is obtained using the two different spatial discretization methods introduced above, namely, the normal-mode and the cubic-spline methods. Then the robustness of the control scheme, based on each of the aforementioned discretization methods, will be assessed in the subsequent chapters. To ease the robustness analysis, the models are sought in the form of a single-input-single-output system. The objective of the control scheme is to suppress the transverse vibration at the tip of the beam, while keeping the desired rigid-body motion. This can be achieved by varying the torque applied at the hub while measuring the tip displacement due to both rigid-body and flexible motions.

The mechanical system under study consists of a clamped-free beam of length L, rotating horizontally about its fixed end, as shown in Fig. 4.1. In this study, the rotary inertia and shear deformation effects can be neglected in order to use Euler-Bernoulli beam theory.

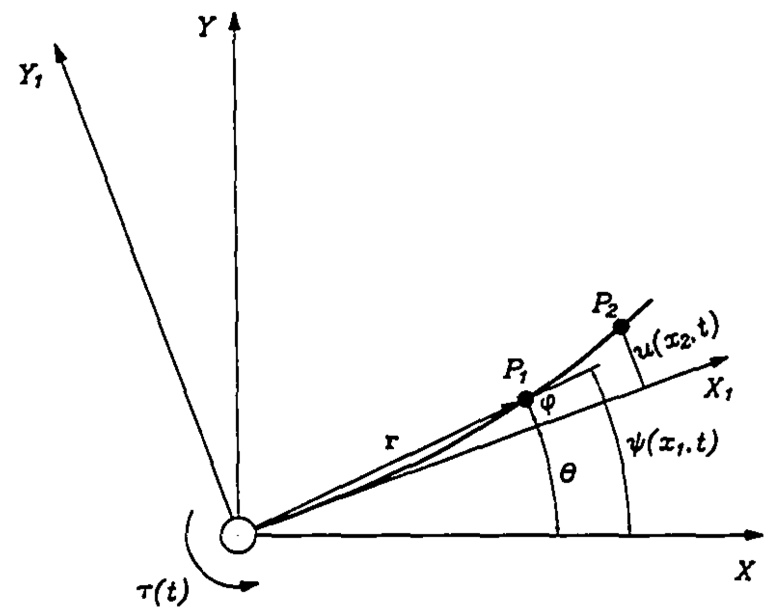

Figure 4.1: Schematic diagram of a rotating flexible beam

The control system to be used must require only a single measurement, which must allow the system to infer both the rigid-body and elastic motions at the same time. Therefore, it is crucial for the output to be expressed in terms of the state-variable vector, which includes the rigid-body and the elastic coordinates.

The kinematic description of the output to be measured, as shown in Fig. 4.1, is given by

$$\psi(L,t) = \theta(t) + \varphi(L,t) \tag{4.68}$$

Moreover, the angular deviation from the neutral axis, $\varphi(L,t)$, is assumed to be small, so that it can be approximated using the linear term of its series expansion, namely,

$$\varphi(L,t) = \tan^{-1}\left(\frac{u(L,t)}{L}\right) \approx \frac{u(L,t)}{L} \tag{4.69}$$

It should be noted that the output can be expressed as a sum of the rigid-body and the elastic motions, and these can be selected as the generalized coordinates, whatever spatial discretization method is used.

The kinetic energy and the potential energy, denoted by T and V, respectively, are given as

$$T = \frac{1}{2}\int_0^L m(x)\dot{\mathbf{r}}^T\dot{\mathbf{r}}dx + \frac{1}{2}I_h\dot{\theta}^2 \tag{4.70}$$

$$V = \frac{1}{2}\int_0^L EI(x)\left[u_{xx}(x,t)\right]^2 dx \tag{4.71}$$

where I_h is the moment of inertia of the hub. In the foregoing equation, the magnitude of the velocity of an arbitrary point along the link is given by

$$\|\dot{\mathbf{r}}\| = \sqrt{u^2\dot{\theta}^2 + x^2\dot{\theta}^2 + \dot{u}^2 + 2x\dot{\theta}\dot{u}} \tag{4.72}$$

Finally, the Lagrangian is calculated as

$$\begin{aligned} L = \ & \tfrac{1}{2}\int_0^L m(x)\left(u^2\dot{\theta}^2 + x^2\dot{\theta}^2 + \dot{u}^2 + 2x\dot{\theta}\dot{u}\right)dx \\ & + \tfrac{1}{2}I_h\dot{\theta}^2 - \tfrac{1}{2}\int_0^L EI(x)\left(u''(x,t)\right)^2 dx \end{aligned} \tag{4.73}$$

The Rayleigh dissipation function is omitted in the foregoing formulation to simplify the dynamic formulation.

Due to the intrinsic nature of the distributed parameter system, a very large number of generalized coordinates is required to describe the vibrational behaviour prope-ly. It is, however, of practical importance to use a manageable and finite set of coordinates. The two spatial discretization methods discussed in Chapter 2 are employed to derive finite-dimensional models.

4.3.2 Normal-Mode Spatial Discretization Method

In this approach, the displacement function is given as a finite sum composed of a linear combination of modes and their normal coordinates, as given in eq.(2.20). The spatial variables appearing in eq.(4.73) can then be replaced with the said displacement function to rewrite the Lagrangian in the framework of the normal-mode analysis. The higher-order terms associated with the elastic motions are then eliminated in the foregoing procedure, so that a linearized model can be constructed. It is, however, noteworthy that the linearization is performed only for the elastic motions and the rigid-body motion is not simplified.

The resulting Lagrangian is given by

$$L = \frac{1}{2}(I_t\dot{\theta}^2 + \dot{q}_r^2 + 2\sum_{r=1}^{n-1} J_r\dot{\theta}\dot{q}_r - \sum_{r=1}^{n-1}\omega_r^2 q_r^2) \tag{4.74}$$

in which

$$I_t = I_h + I_b \tag{4.75}$$

$$J_r = \int_0^L m(x)xY_r(x)dx \tag{4.76}$$

$$\omega_r = (\kappa_r l)^2\sqrt{\frac{EI}{mL^4}}, \quad r = 1, \ldots, n-1 \tag{4.77}$$

and I_b is the moment of inertia of the rigid beam about the centre of the hub. In addition, J_r indicates the coupling between the rigid-body motion and the rth vibrational mode. These coupling terms are also known as the *modal angular momentum coefficients*, and have been found to be useful in determining the dominant modes (Hughes 1980). In fact, the values of these coefficients decrease monotonically toward zero as the number of modes increases. One consequence is that the mutual influence between the rigid-body and the elastic motions becomes weaker for higher modes, to the extent that the higher modes are virtually decoupled from the rigid-body motion. This illustrates the common engineering practice in considering the vibrational behaviour of the structure: the first few modes are significant, while the higher modes may be neglected. A study of the resulting equations of motion illustrates the idea behind such reasoning.

The equations of motion take the form

$$\mathbf{M}_a\ddot{\mathbf{q}} + \mathbf{K}_a\mathbf{q} = \boldsymbol{\tau} \tag{4.78}$$

where $\mathbf{M}_a$ and $\mathbf{K}_a$ are the $n \times n$ mass and stiffness matrices, respectively, while $\mathbf{q}$ and $\boldsymbol{\tau}$ are the n-dimensional vectors of generalized coordinates and generalized applied force. These quantities are given below:

$$\mathbf{M}_a \equiv \begin{bmatrix} \gamma & \boldsymbol{\gamma}^T \\ \boldsymbol{\gamma} & \mathbf{1} \end{bmatrix} \tag{4.79}$$

$$\mathbf{K}_a \equiv \begin{bmatrix} 0 & \mathbf{0}^T \\ \mathbf{0} & \boldsymbol{\Omega} \end{bmatrix} \tag{4.80}$$

$$\mathbf{q} = [\theta \;\; q_1 \;\; \cdots \;\; q_{n-1}]^T \tag{4.81}$$

$$\boldsymbol{\tau} = [\tau(t) \;\; 0 \;\; \cdots \;\; 0]^T \tag{4.82}$$

where $\mathbf{1}$ is the $(n-1) \times (n-1)$ identity matrix and $\mathbf{0}$ is the $(n-1)$-dimensional zero vector. Moreover,

$$\gamma \equiv I_t \tag{4.83}$$

$$\boldsymbol{\gamma} \equiv [J_1 \;\; J_2 \;\; \cdots \;\; J_{n-1}]^T \tag{4.84}$$

$$\boldsymbol{\Omega} \equiv \mathrm{diag}(\omega_1^2 \;\; \omega_2^2 \;\; \cdots \;\; \omega_{n-1}^2) \tag{4.85}$$

The off-diagonal terms of the mass and stiffness matrices associated with the elastic coordinates are zero and their only connections to the rigid-body motion take place through the coupling vector $\boldsymbol{\gamma}$. As this vector becomes closer to zero, the corresponding mode is virtually decoupled from the rigid-body motion. Consequently, that specific mode becomes uncontrollable from the rigid-body motion provided at the hub. This will be further investigated in conjunction with the several control issues in Chapter 5. Moreover, the generalized coordinates used to describe the elastic motions do not represent any measurable physical quantity.

Finally, the output to be measured can be expressed in terms of the generalized coordinates, namely,

$$\varphi(L,t) = \boldsymbol{\xi}_a^T \mathbf{q} \tag{4.86}$$

where

$$\xi_a = \left[1 \ \ \frac{Y_1(l)}{L} \ \ \cdots \ \ \frac{Y_{n-1}(l)}{L}\right]^T \tag{4.87}$$

Since the elastic coordinates are not directly measurable, the output needs to be measured through an indirect method, such as a vision system.

4.3.3 Cubic-Spline Spatial Discretization

Applying the cubic-spline discretization in the same manner used in the previous section, the Lagrangian becomes

$$L = \frac{1}{2}(\gamma\,\dot{\theta}^2 + \dot{\mathbf{u}}''^T\,\mathbf{\Gamma}\dot{\mathbf{u}}'' + 2\,\boldsymbol{\gamma}^T\dot{\theta}\dot{\mathbf{u}}'' - \mathbf{u}''^T\,\mathbf{\Omega}\mathbf{u}'') \tag{4.88}$$

The coefficients in the above equation are readily obtained from Table 4.2, namely,

$$\gamma \equiv I_t \tag{4.89}$$

$$\boldsymbol{\gamma}^T \equiv m\sum_{j=1}^{n-1}\int_{x_j}^{x_{j+1}} x\mathbf{s}_j^T(x)\mathbf{\Delta}_j dx \tag{4.90}$$

$$\mathbf{\Gamma} \equiv m\sum_{j=1}^{n-1}\int_{x_j}^{x_{j+1}} \mathbf{\Delta}_j^T\mathbf{F}_j(x)\mathbf{\Delta}_j dx \tag{4.91}$$

$$\mathbf{\Omega} \equiv \sum_{j=1}^{n-1}\mathbf{\Delta}_j^T\int_{x_j}^{x_{j+1}} EI(x)\mathbf{F}_j''(x)dx\;\mathbf{\Delta}_j^T \tag{4.92}$$

the equations of motion thus becoming

$$\mathbf{M}_c\ddot{\mathbf{q}} + \mathbf{K}_c\mathbf{q} = \boldsymbol{\tau} \tag{4.93}$$

where the $n \times n$ mass and stiffness matrices, as well as the n-dimensional vectors of generalized coordinates and generalized applied force are given below:

$$\mathbf{M}_c = \begin{bmatrix} \gamma & \boldsymbol{\gamma}^T \\ \boldsymbol{\gamma} & \mathbf{\Gamma} \end{bmatrix} \tag{4.94}$$

$$\mathbf{K}_c = \begin{bmatrix} 0 & \mathbf{0}^T \\ \mathbf{0} & \mathbf{\Omega} \end{bmatrix} \tag{4.95}$$

$$\mathbf{q} = [\theta \ \ u_1'' \ \ \cdots \ \ u_{n-1}'']^T \tag{4.96}$$

$$\boldsymbol{\tau} = [\tau(t) \ \ 0 \ \ \cdots \ \ 0]^T \tag{4.97}$$

The mass and stiffness matrices associated with the elastic coordinates $\mathbf{\Gamma}$ and $\mathbf{\Omega}$ are symmetric, positive-definite and their off-diagonal elements are not necessarily zero, as in the normal-mode approach. Moreover, the coupling vector $\boldsymbol{\gamma}$ does not monotonically approach zero, as the number of the elastic modes increases. The coupling terms are simply a relation between the rigid-body motion and the curvature at the supporting points. Remember that the elastic coordinates used in this method are physical variables that can be directly measured using accurate, yet fast strain gauges.

The output to be measured can be expressed in terms of the generalized coordinates, namely,

$$\varphi(L,t) = \boldsymbol{\xi}_c^T \mathbf{q} \tag{4.98}$$

where

$$\boldsymbol{\xi}_c \equiv \mathbf{T}_c^T \begin{bmatrix} 1 \\ \mathbf{0}_{n-2} \\ \frac{1}{L} \end{bmatrix} \tag{4.99}$$

From the above equation, the end-tip displacement can be inferred from the curvature vector $\mathbf{u}''$, which is measured from a set of strain gauges.

Chapter 5

A Robust Model for the Discretization of Flexible Links Based on Cubic Splines

5.1 Introduction

Upon constructing the dynamic model of the rotating flexible beam in state-sp~ce form using the two different spatial discretization methods, the robustness of the control system to be designed based on this model is examined in terms of observation and control spillovers. Both spillovers reduce the stability margin and degrade the system response associated with the noncollocated control problem. A robustness analysis based on such considerations is thus essential before proceeding to a real-time implementation.

A sensitivity analysis of the LQG compensators is performed to assess the capability of attenuating estimation errors due to unmodelled higher-order dynamics. In this regard, the sensitivity function and its complement are formulated. These functions give insight not only into the observation spillover, but also into the reason why the accuracy of the model becomes so important in noncollocated control.

In order to deal with the control spillover, the allowable bound for nonlinear perturbations is sought in conjunction with the LQ state feedback. This bound allows us to quantify the upper level of nonlinear perturbations for which the closed-loop system remains stable. Moreover, such a quantitative measure is used in the selection of the weighting matrices in a quadratic performance index, so that the resulting LQ state feedback becomes robust against nonlinear perturbations.

Simulation studies are undertaken to address the robustness of the control scheme obtained using two spatial discretization techniques: normal modes and cubic splines. Finally, the Nyquist plots of the closed-loop systems are presented to show the frequency response at the cross-over frequency.

5.2 Control Strategy

Considering the tip angle given in eq.(4.68) as the output to be measured, the governing equations of motion obtained by either of the preceding two spatial discretization techniques—eqs.(4.78) or (4.93)—can be cast in state-variable form, namely,

$$\dot{\mathbf{x}}(t) = \mathbf{A}\mathbf{x}(t) + \mathbf{b}u(t) \tag{5.1}$$

$$y(t) = \mathbf{c}^T\mathbf{x}(t) \tag{5.2}$$

where

$$\mathbf{A} = \begin{bmatrix} \mathbf{O} & \mathbf{1} \\ -\mathbf{M}^{-1}\mathbf{K} & \mathbf{O} \end{bmatrix} \in \mathbb{R}^{(2n\times 2n)} \tag{5.3}$$

$$\mathbf{b} = \begin{bmatrix} \mathbf{0} \\ \mathbf{M}^{-1}\mathbf{p} \end{bmatrix} \in \mathbb{R}^{2n} \tag{5.4}$$

$$\mathbf{c}_a = \begin{bmatrix} \boldsymbol{\xi}_a \\ \mathbf{0} \end{bmatrix}, \quad \mathbf{c}_c = \begin{bmatrix} \boldsymbol{\xi}_c \\ \mathbf{0} \end{bmatrix} \in \mathbb{R}^{2n} \tag{5.5}$$

with $\mathbf{O}$ and $\mathbf{1}$ denoting the $n \times n$ zero and identity matrices, respectively. Moreover, $\mathbf{0}$ is the n-dimensional zero vector and the permutation vector $\mathbf{p}$ is given by

$$\mathbf{p} = [1 \;\; \mathbf{0}_{n-1}]^T \tag{5.6}$$

The state vector and scalar input are thus defined as

$$\mathbf{x}(t) = \begin{bmatrix} \mathbf{q}^T(t) & \dot{\mathbf{q}}^T(t) \end{bmatrix}^T, \quad u(t) = \tau(t). \tag{5.7}$$

Assuming that this model is perfect, the state-variable feedback is then obtained by the substitution

$$u(t) = v(t) - \mathbf{k}^T\mathbf{x}(t) \tag{5.8}$$

where $v(t)$ is an external input and the feedback gain $\mathbf{k}$ is sought to minimize the quadratic performance index J defined below:

$$J = \int_0^\infty (\mathbf{x}^T\mathbf{Q}\mathbf{x} + ru(t)^2)dt \tag{5.9}$$

with $\mathbf{Q}$ being positive-semidefinite and $r > 0$. How $\mathbf{Q}$ and r should be selected will be discussed in 5.6.2. The overall system is shown in Fig. 5.1. In the next section, it is assumed that the actual plant is the same as the model, to simplify the study of observation spillover. In section 5.4, it is assumed that all the state variables are directly available but the actual plant has unmodelled dynamics.

5.3 Sensitivity of the LQG Compensator

Observation spillover depends mainly on the capability of the LQG compensator to attenuate estimation errors due to unmodelled higher-order dynamics. These signals are usually characterized by their frequency spectra. To obtain insight into the observation spillover, the sensitivity function of the LQG compensator is formulated as shown in Fig. 5.1 assuming that the actual plant is equal to the linear model given by eqs.(5.1) and (5.2), and the observation noise signals are the only source of disturbance in the system.

Since all state variables are available, the state feedback signal $z(t)$ takes the form

$$z(t) = -\mathbf{k}^T\hat{\mathbf{x}}(t) \tag{5.10}$$

$$= -\mathbf{k}^T\mathbf{x}(t) + w(t) \tag{5.11}$$

where $\tilde{\mathbf{x}} \equiv \mathbf{x} - \hat{\mathbf{x}}$, $w(t) \equiv \mathbf{k}^T\tilde{\mathbf{x}}(t)$. Moreover, $\hat{\mathbf{x}}(t)$ and $\tilde{\mathbf{x}}(t)$ denote the estimated state and estimation error, respectively.

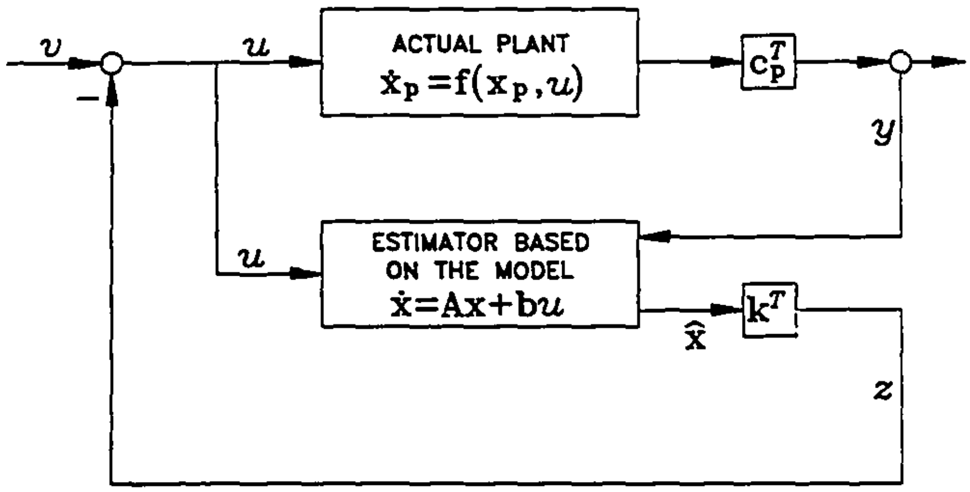

Figure 5.1: LQG compensator for the actual plant, where $\mathbf{x}_p \in I\!R^N$ with the model $\mathbf{x} \in I\!R^{2n}$, where $N > 2n$

The LQG compensator shown in Fig. 5.1 is known to be equivalent to the unity feedback form shown in Fig. 5.2 (Anderson and Moore, 1971), where $e(s) \equiv u(s)$. It should be noted that, for the arguments which follow in this section, the loop gain, $\mathbf{k}^T(s\mathbf{I} - \mathbf{A})\mathbf{b}$, is considered as a virtual plant to be controlled with unity feedback and that the disturbance $w(s)$ is due to estimation errors. In this formulation, let the

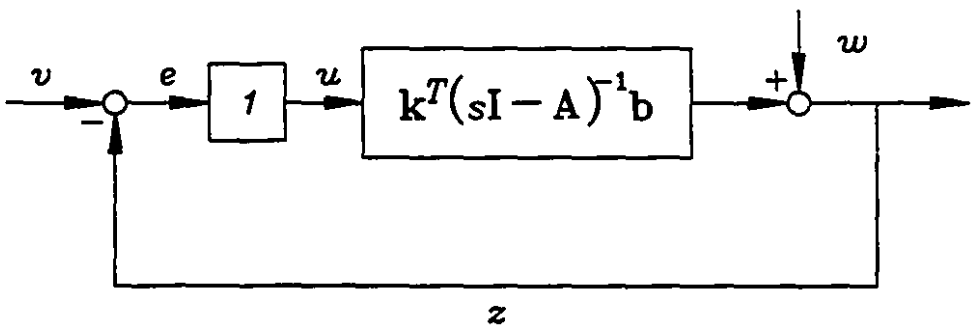

Figure 5.2: Closed-loop optimal control scheme as a unity feedback system

signal $z(t)$ be an output to be controlled, which is defined as

$$z(s) = \mathbf{k}^T(s\mathbf{I} - \mathbf{A})^{-1}\mathbf{b}u(s) + w(s) \tag{5.12}$$

$$= \frac{n(s)}{d(s)}u(s) + w(s) \tag{5.13}$$

Since

$$u(s) = v(s) - z(s) \tag{5.14}$$

we obtain

$$z(s) = T(s)v(s) + S(s)w(s) \tag{5.15}$$

$$u(s) = S(s)(v(s) - w(s)) \tag{5.16}$$

where $S(s)$ and its complement $T(s)$ are given by

$$T(s) = \frac{\mathbf{k}^T(s\mathbf{I} - \mathbf{A})^{-1}\mathbf{b}}{1 + \mathbf{k}^T(s\mathbf{I} - \mathbf{A})^{-1}\mathbf{b}} = \frac{n(s)}{n(s) + d(s)} \tag{5.17}$$

$$S(s) = \frac{1}{1 + \mathbf{k}^T(s\mathbf{I} - \mathbf{A})^{-1}\mathbf{b}} = \frac{d(s)}{n(s) + d(s)} \tag{5.18}$$

and satisfy $S(s) + T(s) = 1$. It is known that the transfer function $S(s)$ from the external input v to the plant input u represents the sensitivity to parameter variations of an optimal state feedback with respect to an equivalent state feedforward, namely,

$$\Delta H_c(s) = S(s)\Delta H_o \tag{5.19}$$

where $\Delta H_c(s)$ and ΔH_o denote changes in the closed-loop system and changes in a nominally equivalent open-loop system, respectively (Doyle and Stein, 1981). It turns out that state feedback reduces sensitivity to plant parameter variations if the magnitude of the return difference, defined as $|1 + \mathbf{k}^T(s\mathbf{I} - \mathbf{A})^{-1}\mathbf{b}|$, is larger than or equal to unity over a sufficiently wide band of frequencies (Perkins and Cruz, 1971). Moreover, if the pair $(\mathbf{A}, \mathbf{b})$ is completely controllable and the pair $(\mathbf{k}, \mathbf{A})$ is completely observable, the following two facts hold: 1) all state variables can be affected by a suitable choice of control input $u(t)$ and 2) the control input given in eq.(5.14) can be identically zero only if the state is identically zero (Kalman, 1964). This can be illustrated using unity feedback, i.e., eq.(5.16), where $v(s) \equiv u(s)$. Ideally, the error remains small and bounded in the passband if the sensitivity function $S(s)$ approaches zero there, and thus makes its complement $T(s)$ close to one. This will provide successful tracking of $z(t)$ to $v(t)$. However, this is not usually possible in the presence of the unstable zeros of the plant. Therefore, a compromise has to be made to meet as closely as possible the desired specifications.

5.4 Robustness of the LQ State Feedback

In practice, the actual system is nonlinear and often subjected to parameter and structural variations, thereby making its accurate mathematical representation difficult to obtain. It is therefore necessary to measure the robustness of the linear-quadratic controller in the presence of nonlinear perturbations (Patel, Toda and Shidhar, 1977). In this section, the allowable bound for nonlinear perturbations is sought, in order to deal with the control spillover resulting from modelling errors. This bound helps to quantify the effects of unmodelled residuals on the closed-loop system.

The nonlinear perturbations associated with parameter variations and modelling errors are taken into account by the addition of a vector $\mathbf{g}$ to eq.(5.1), as

$$\dot{\mathbf{x}}(t) = \mathbf{A}\mathbf{x}(t) + \mathbf{b}u(t) + \mathbf{g}(\mathbf{x}(t), u(t)) \tag{5.20}$$

Since the exact expression of the nonlinear perturbations is not available, the control input is generated based on the linear model given in eq.(5.1). Under the state feedback law $u(t) = -\mathbf{k}^T\mathbf{x}(t)$, the resulting closed-loop system is given by

$$\dot{\mathbf{x}} = \mathbf{A}_c\mathbf{x} + \mathbf{g}(\mathbf{x}) \tag{5.21}$$

$$J = \int_0^\infty \mathbf{x}^T(t)(\mathbf{Q} + \frac{1}{r}\mathbf{k}\mathbf{k}^T)\mathbf{x}(t)dt \tag{5.22}$$

where

$$\mathbf{A}_c \equiv \mathbf{A} - \mathbf{b}\mathbf{k}^T \tag{5.23}$$

To minimize J, the stabilizing gain $\mathbf{k}$ must satisfy the necessary condition (Bélanger, 1990)

$$\mathbf{k} = \frac{1}{r}\mathbf{S}\mathbf{b} \tag{5.24}$$

where $\mathbf{S}$ satisfies the matrix Riccati equation

$$\mathbf{O} = \mathbf{A}^T\mathbf{S} + \mathbf{S}\mathbf{A} - \frac{1}{r}\mathbf{S}\mathbf{b}\mathbf{b}^T\mathbf{S} + \mathbf{Q} \tag{5.25}$$

Then there exists a sufficient condition for an allowable level of nonlinear perturbation such that the stability of the closed-loop system is not disturbed. We now recall

Theorem 5.1 *(Patel, Toda and Shidhar, 1977) Let* $\mathbf{D} = \mathbf{Q} + \frac{1}{r}\mathbf{S}\mathbf{b}\mathbf{b}^T\mathbf{S}$. *The closed-loop system, given in eq.(5.21), remains asymptotically stable if the nonlinear vector function* $\mathbf{g}$ *satisfies the following condition:*

$$\frac{\|\mathbf{g}(\mathbf{x})\|}{\|\mathbf{x}\|} < \zeta = \frac{1}{2\|\mathbf{D}\|_s\|\mathbf{S}\|_s} = \frac{\sigma_{min}(\mathbf{D})}{2\sigma_{max}(\mathbf{S})} \tag{5.26}$$

where $\|\cdot\|$ *and* $\|\cdot\|_s$ *denote the Euclidean and the spectral norms, respectively. Moreover,* $\sigma_{max}(\mathbf{S})$ *denotes the largest singular value of* $\mathbf{S}$, *while* $\sigma_{min}(\mathbf{D})$ *denotes the smallest singular value of* $\mathbf{D}$. *For completeness, the proof of this theorem is given in Appendix A.*

5.5 Non-Zero Set-Point Tracking

If the goal of the control scheme is to force the plant output to follow a non-zero set point, then we need

$$y(t) = \mathbf{c}^T\mathbf{x} \longrightarrow y_d \tag{5.27}$$

This can be achieved by using a constant command input r_d such that

$$\dot{\mathbf{x}} = \mathbf{0} = (\mathbf{A} - \mathbf{b}\mathbf{k}^T)\mathbf{x} + \mathbf{b}r_d \tag{5.28}$$

and thus

$$y_d = \mathbf{c}^T \mathbf{x}_d = \mathbf{c}^T(-\mathbf{A} + \mathbf{b}\mathbf{k}^T)^{-1}\mathbf{b} v_d = H_k(0) r_d \tag{5.29}$$

where $H_k(s)$ is the closed-loop transfer function given by

$$H_k(s) = \mathbf{c}^T(s\mathbf{I} - \mathbf{A} + \mathbf{b}\mathbf{k}^T)^{-1}\mathbf{b} \tag{5.30}$$

When $H_k(0) \neq 0$, a constant command input can be uniquely determined by

$$r_d = H_k^{-1}(0) y_d \tag{5.31}$$

and the closed-loop transfer function (to the constant command input) can be normalized as

$$y(s) = H(s) y_d(s) = H_k(s) H_k^{-1}(0) r_d \tag{5.32}$$

5.6 Simulation Results

Simulations are performed in order to study the robustness of the models obtained using cubic splines and normal modes. These studies include a sensitivity analysis to investigate the effects of observation spillover and permit a quantitative measure of the robustness bound to prevent control spillover. The number of generalized coordinates and material parameters described in Table 5.1 are used in the simulations. In addition, the same weighting matrices are used for the cubic-spline and normal-mode methods to obtain the linear-quadratic regulator gain **k**, namely,

$$\mathbf{Q} = \begin{bmatrix} (100)\,\mathbf{1}_n & \mathbf{O}_n \\ \mathbf{O}_n & (0.1)\,\mathbf{1}_n \end{bmatrix}, \quad r = 1$$

It should be recognized that the models obtained using the aforementioned spatial discretization methods describe a vibrational behaviour of the same system and the state-space system representations thus obtained are expected to possess more or less the same input-output characteristics such as the frequency response. Figure 5.3 shows

Table 5.1: Material properties of the beam

number of nodal points (cubic-spline model)	5
number of modes to be considered (normal-mode model)	4
mass per unit length (m)	0.6697 [kg/m]
flexural rigidity (EI)	14.8535 [kg m^3/s^2]
moment of inertia of the hub (I_h)	2.0927×10^{-4} [kg-m^2]
moment of inertia of the unflexed rigid beam (I_b)	0.2232 [kg-m^2]
length (L)	1 [m]
cross-section	0.0762 $\times$ 0.0032 [m^2]

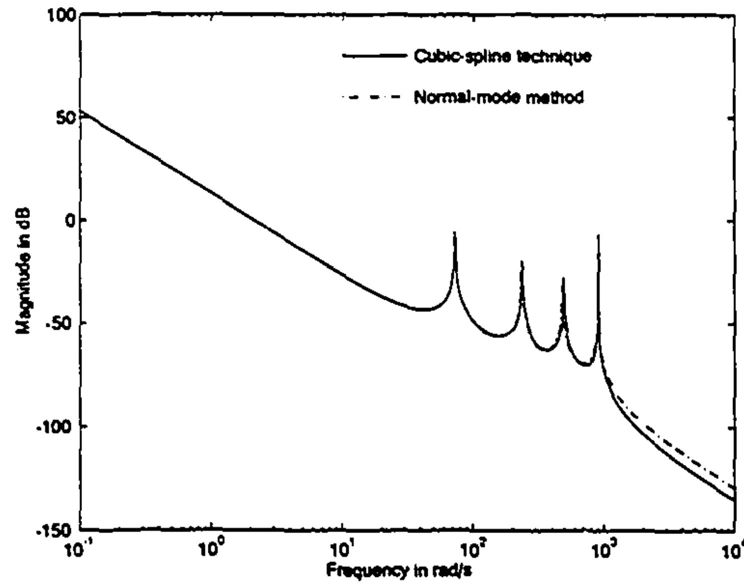

Figure 5.3: Magnitude plot of the open-loop transfer functions with the different spatial discretization

the frequency responses for the two discretization methods. A small difference can be seen between the two at a high-frequency range.

The frequency responses for the closed-loop transfer functions, on the other hand, may differ between the two methods, depending on the description of the internal behaviour of the system. The robustness analysis of the two modelling methods determines which method is more amenable to state feedback control.

5.6.1 Observation Spillover

To investigate the observation spillover due to the neglected higher-order modes, the sensitivity functions, that are a measure of the response to the observation noise signals, are obtained using the controllers based on the two discretization methods. If a control system results in $|S(j\omega)| < 1$, the sensitivity at ω is reduced by the control system. The magnitudes of the sensitivity functions are plotted in Fig. 5.4, and those of complementary sensitivity functions in Fig. 5.5. It can be seen that $|S(j\omega)|$ approaches 0 and $|T(j\omega)|$ approaches 1, where ω is close to the natural frequencies of the open-loop system, which are equivalent to the open-loop poles. This phenomenon can be readily illustrated using eqs.(5.17) and (5.18), namely,

$$S(j\omega_i) = \frac{d(j\omega_i)}{n(j\omega_i) + d(j\omega_i)} = 0, \quad i = 1, \cdots, n-1 \tag{5.33}$$

$$T(j\omega_i) = 1 - S(j\omega_i) = 1 \tag{5.34}$$

in which ω_i is the ith natural frequency of the open-loop system; that is, $d(j\omega_i) = 0$.

When using the normal-mode method, the insensitive regions are concentrated in a narrow band of frequencies around ω_i $(i = 1, \cdots, n-1)$. Furthermore, no sensitivity reduction is achieved at natural frequencies higher than 10^3[rad/s]. In contrast, the sensitivity with the cubic-spline description are lower over all frequency ranges and the insensitive regions are wider. Consequently, the compensator based on the cubic spline technique is less sensitive to observation noise signals and has smaller observation spillover effects.

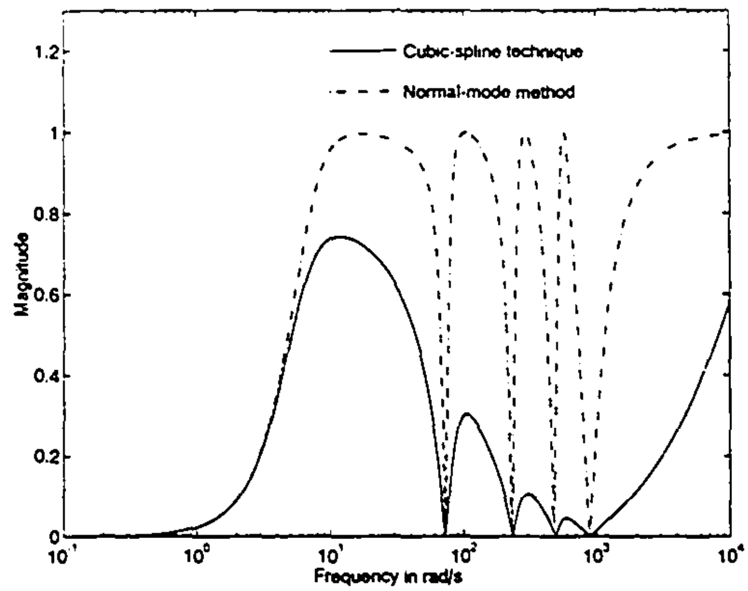

Figure 5.4: Magnitude plot of the sensitivity $S(j\omega)$

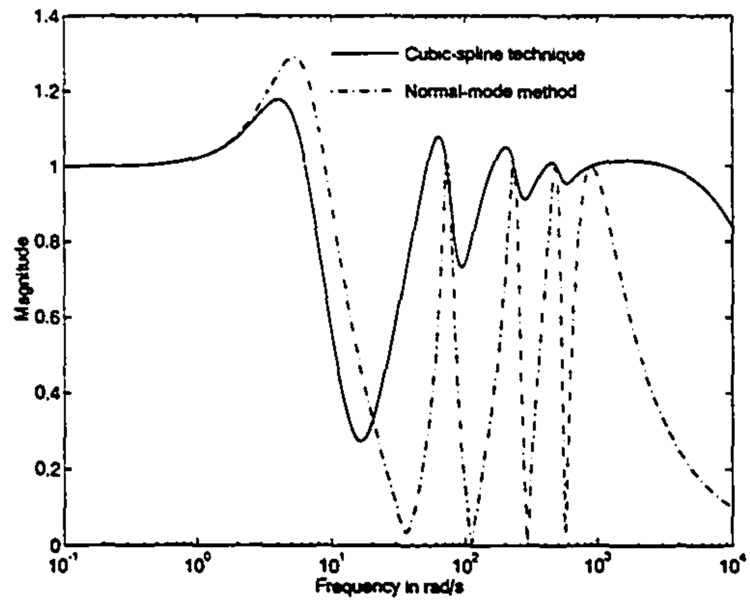

Figure 5.5: Magnitude plot of the complement of the sensitivity $T(j\omega)$

Since the actual system is subjected to modelling errors and nonlinear perturbations, the natural frequencies of the system undergo small deviations from those of the model. Hence, it is desirable for a control law to have a distribution of the insensitive region around the natural frequencies of the system. For this reason, the accuracy of the model becomes more critical when the normal-mode approach is used.

With the sensitivity functions obtained with the same weighting matrices, the state variables in the two different spatial discretizations are different since they are defined in terms of different generalized coordinates: curvatures along the beam and normal coordinates as defined in eq.(5.7). Another useful comparison is based on the pole locations of the closed-loop system, since the control objectives do not vary with different modelling approaches. It turns out that the sensitivity obtained using the normal-mode method can be reduced to match that obtained using the cubic-spline technique, but at the expense of a higher state feedback gain. For example, the control gain $\mathbf{k}_a$ that produces the sensitivity function, shown in Fig. 5.4 for the cubic-spline model, is given by

$$\mathbf{k}_a = 1.0 \times 10^4 \begin{bmatrix} 0.0011 \\ -0.0062 \\ -0.1621 \\ -1.7032 \\ -7.8429 \\ 0.0003 \\ 0.0000 \\ -0.0015 \\ -0.0041 \\ -0.0013 \end{bmatrix}, \mathbf{k}_c = \begin{bmatrix} 10.0000 \\ -57.3803 \\ 120.8451 \\ -97.4219 \\ 64.4285 \\ 2.5610 \\ -0.1325 \\ 0.1771 \\ 0.1215 \\ -0.0237 \end{bmatrix} \tag{5.35}$$

while $\mathbf{k}_c$ is the corresponding control gain for the cubic-spline technique. In the gain vector $\mathbf{k}_a$, the magnitude becomes larger as the number of modes increases. This means that larger weighting factors are necessary to penalize the deviations of the state variables associated with the higher modes. Considering that these gain vectors produce the same control input when multiplied by the corresponding state variables, the higher gain may give rise to numerical ill-conditioning and degrade the performance of the control system.

The compensator based on the cubic-spline technique not only provides significant advantages in terms of sensitivity reduction, but also places less severe requirements on the accuracy of the model. Moreover, this is achieved without introducing a higher gain, which may reduce the stability margins.

5.6.2 Control Spillover

By varying the weighting matrices of the LQ state feedback, bounds on the stability margin can be quantitatively measured in the presence of nonlinear perturbations for both spatial discretization methods. Such bounds help to establish the relation between allowable perturbations and the choice of weighting matrices in the quadratic performance index. Moreover, these bounds indicate tolerable levels of spillover due to modelling errors for a stable operation.

The weighting factors are chosen as

$$\mathbf{Q} = \begin{bmatrix} p\mathbf{1}_n & \mathbf{O}_n \\ \mathbf{O}_n & v\mathbf{1}_n \end{bmatrix}, \quad r = 1 \tag{5.36}$$

where p is the weighting factor for $\mathbf{q}$ (in this simulation, $p = 100$) and v is the weighting factor for $\dot{\mathbf{q}}$, which varies from 0 to 1. Moreover, $\mathbf{1}_n$ is the n-dimensional identity matrix.

The difference between the two discretization methods becomes apparent in Fig. 5.6. It can be seen that the LQ state feedback based on the cubic-spline description can accommodate nonlinear perturbations with an approximate order of magnitude three times greater than that based on the normal-mode approach. The LQ state feedback based on the cubic-spline approximation is thus robust against modelling errors and

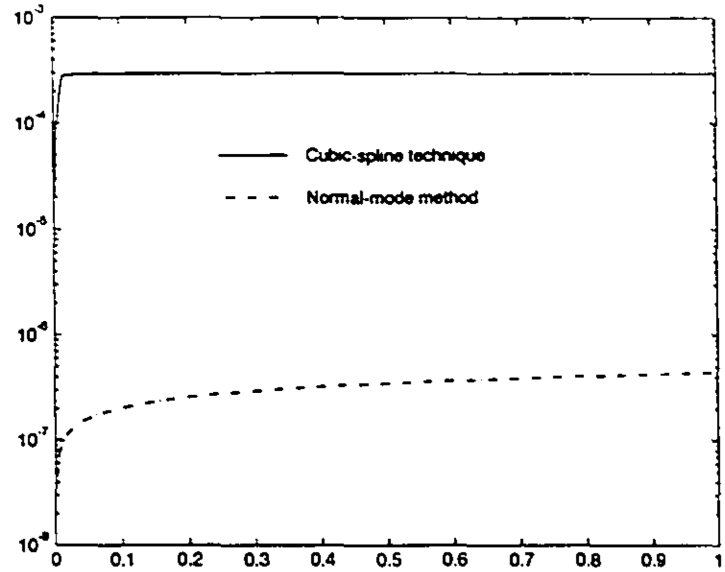

Figure 5.6: Measure of robustness ζ with varying weighting factor v

nonlinear perturbations. Moreover, it may be difficult to determine the proper weighing factors that will make the system robust against nonlinear perturbations when using the normal-mode method.

A Nyquist plot of the open-loop transfer function can be used to determine whether the closed-loop system is stable by examining its behaviour near the crossover frequency. However, since high-order stiff systems have a large peak in the plot, the Nyquist plot of the closed-loop transfer function with a constant reference signal is used to observe the effect of varying the weighting factors as given in eqs.(5.36).

In the Nyquist plot of the closed-loop system obtained using the normal-mode method, the relatively higher peaks can be seen across the natural frequencies (Fig. 5.7). This Nyquist locus consists of sets of peaks that result from the dynamics of the corresponding modes including the rigid-body motion. The said locus closely resembles that obtained from a higher-order oscillatory system.

In contrast to the normal-mode method, the Nyquist plot of the closed-loop system obtained using the cubic-spline technique is very smooth over the entire frequency

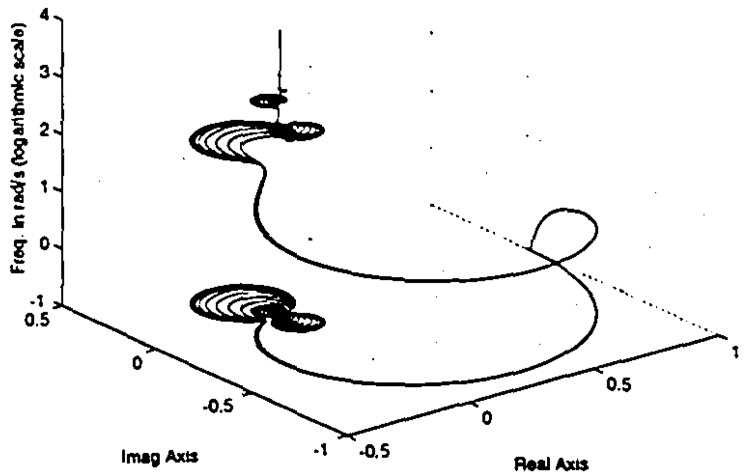

Figure 5.7: Nyquist plots with different weightings for a constant input using the normal-mode method

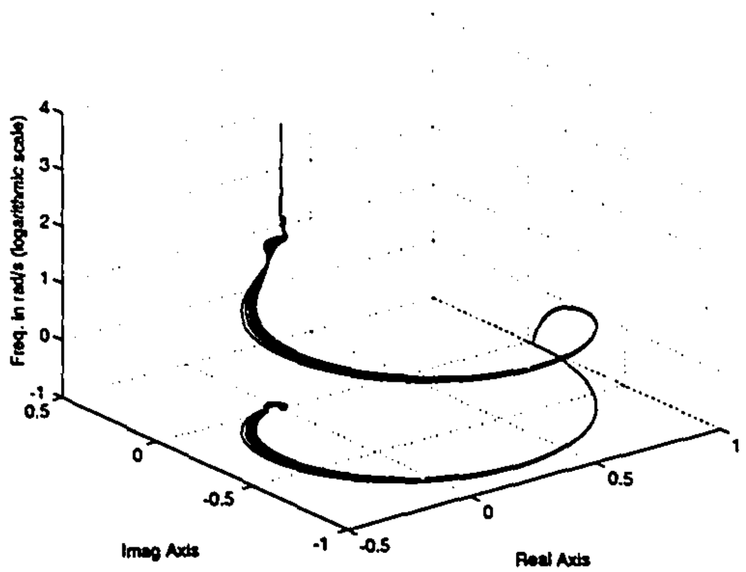

Figure 5.8: Nyquist plots with different weightings for a constant input using the cubic-spline technique

range and relatively smaller peaks are observed associated with the higher modes (Fig. 5.8). This locus is similar to a family of third-order systems.

Despite the almost identical open-loop frequency responses, the closed-loop systems under the same unity-feedback and the same input-output configuration behave differently, especially at higher frequencies, depending on how the vibrational behaviour is described. The effects of the higher modes are obvious in the closed-loop system based on the normal-mode method, whereas such effects are not significant in the closed-loop system based on the cubic-spline model.

The above differences stem from the way in which the model incorporates the correlations among the modes. When using the normal modes, such correlations do not exist, due to the orthogonality conditions. Hence, increasing the number of modes to be considered directly results in an increase in the order of the system model, as observed in the closed-loop Nyquist plot. However, since the cubic-spline model relies on the distribution of strains along the beam, its interpretation of the mode is more physical rather than mathematical. Hence, no such a restriction as the orthogonality of the modes is applied and, thus, mutual influences between the modes can be readily incorporated into the model. In fact, these mutual influences are well observed using the cubic-spline model, namely, the magnitude of the sensitivity function monotonically decreases as the frequencies increase and the effect of the higher modes becomes negligible in the closed-loop Nyquist locus.

From the control standpoint, the model based on cubic splines seems to be much more attractive than the model based on normal modes, due to its better sensitivity characteristic and the robustness of the closed-loop control system to the higher modes. However, there remains one contradiction to be explained: how the approximated model can give rise to a better response than the exact model. This contradiction arises from the fact that cubic splines are used as trial functions to approximate the modes.

It should be recognized that the time-varying coefficients of the cubic splines, which are required to determine the shape function of the beam, are expressed in terms of curvatures. These variables can be readily obtained using strain gauges and thus allow the on-line construction of the shape function that is, in turn, used to describe the vibrational behaviour of the flexible beam. However, in the normal-mode approach, the modes are calculated off-line once and for all and the time-varying quantities, the so called normal coordinates, are used to determine the contribution of each mode to the shape function. Moreover, such variables by themselves do not have any physical interpretation. Simply, they are not measurable.

Therefore, the cubic-spline model is more amenable to real-time control due to its on-line capability of updating the shape function.

Chapter 6

Design and Implementation of the Control Scheme

6.1 Introduction

A model-based control algorithm is presented for a structurally flexible planar mechanism to achieve the performance of its rigid-link counterpart as closely as possible. The control objective is to suppress the vibrations of the flexible elements, while producing the required rigid-body motion. The controller consists of two blocks: the first block is dedicated to the linearization of the highly coupled nonlinear system, while the second block is used to obtain the joint torques required to drive the system. The latter is achieved using a natural orthogonal complement (NOC) filter, which is a transformation applied to the generalized force inputs. The NOC filter produces the applied joint torque as their outputs with all non-working constraint forces eliminated. This model-based control algorithm virtually amounts to those used in industrial robots, where each joint is controlled individually.

Regarding the digital implementation of the proposed control scheme, we resort to a discrete-time system representation using the Euler operator. The advantages thus obtained over the usual shift operator are: 1) improved numerical properties, 2) ease in specifying performance requirements and 3) facilitated evaluation of the digital controller in the continuous-time context.

To quantitatively measure the robustness bound of the discrete-time LQ state feedback in the presence of nonlinear perturbations, two theorems are proposed. The robustness bound obtained using the Euler operator converges to the corresponding continuous-time result both algebraically and numerically. This analysis will help a designer understand the performance of the discrete-time LQ state feedback in the presence of nonlinear perturbations, and select an appropriate sampling interval, which ensures the proper system response.

6.2 Design of the Nonlinear Control Scheme Using the NOC

The coupled equations of motion, for the four-bar linkage with structurally flexible elements as given in eq.(4.61), reveals that the mass, Coriolis and stiffness matrices are coupled with the kinematic constraint equations in quadratic form. The kinematic constraint equations are expressed in terms of the NOC, which is configuration-dependent. Hence, the equations of motion are highly coupled and nonlinear.

It is, however, noteworthy that the rigid-body components of the mass matrix in the decoupled equations of motion, given in eq.(4.46), become constant in the planar case and the nonlinearities are only associated with flexible coordinates. This is attributed to the following two facts: 1) each individual link is considered as an unconstrained body; 2) the equations of motion for each individual link are obtained using Lagrange's equations in a local frame. The decoupled equations of motion are indeed a collection of the equations of motion for each individual link. The couplings between links are achieved through the NOC. It is, therefore, natural for the decoupled equations of motion to have constant components associated with rigid-body coordinates.

Considering that both eqs.(4.46) and (4.61) describe the same dynamic system, a linear compensator can be obtained by linearizing the decoupled equations of motion. Moreover, such a linearization naturally eliminates the Coriolis term by virtue of eq.(4.44), thereby obtaining

$$\dot{\mathbf{x}}(t) = \mathbf{A}\mathbf{x}(t) + \mathbf{B}\mathbf{w}(t) \tag{6.1}$$

$$\mathbf{y} = \mathbf{C}\mathbf{x}(t) \tag{6.2}$$

where $\mathbf{w}$ is the vector of generalized forces.

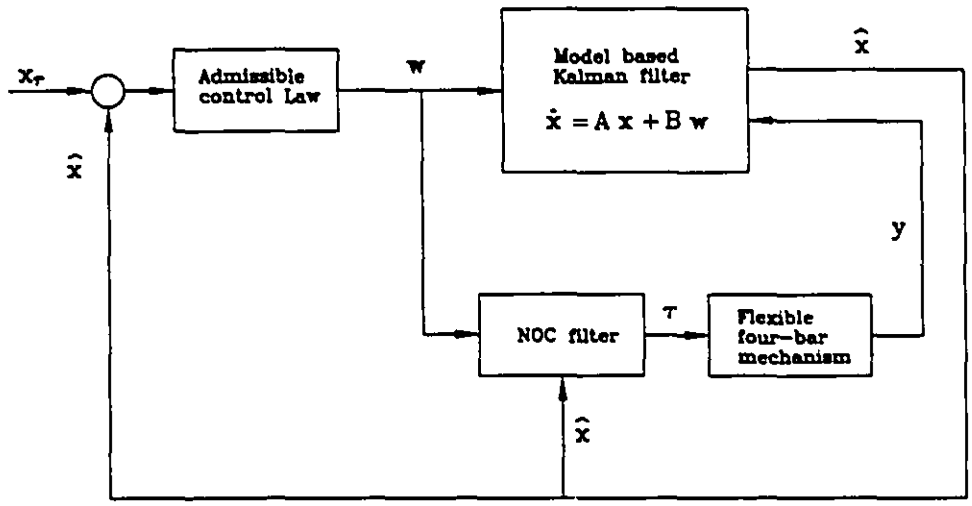

Figure 6.1: Block diagram of the model-based control algorithm using the NOC

One consequence of using the decoupled equations as the governing equations would be the introduction of the generalized forces instead of the applied joint torques. Although the generalized forces are readily obtained by an admissible control law combined with a Kalman filter, there remains the problem of how to extract the applied torques from the generalized forces while filtering out the nonworking constrained forces. Towards this end, the generalized forces are filtered using the NOC as

$$\mathbf{N}^T\mathbf{w} = \boldsymbol{\tau} \equiv \tau\mathbf{p} \tag{6.3}$$

thereby providing the applied generalized torque as shown in Fig. 6.1.

Since the NOC is configuration-dependent, another loop is necessary for the NOC to assess the state variables. It should be realized that the NOC is a sparse matrix whose nonzero elements can be obtained through the relations between the extended and independent generalized speeds. The proposed control scheme, even with an online calculation of the NOC, is implemented with the use of a digital signal processor (DSP).

6.3 LQG Compensator Using the Euler Operator

The LQG compensator consists of the state observer, also known as the Kalman filter, and the feedback of the resultant state estimates. The controller is driven by the estimated deviations of the state variables from their desired values and generates the control signals in such a way that the said deviations remain as small as possible at all times (Athans, 1971). This approach has a particular importance when some of the state variables are not obtainable through direct measurement.

To implement the proposed control algorithm, we resort to a discrete-time system representation using the Euler operator, which is defined as

$$\varepsilon \equiv \frac{z-1}{T} \tag{6.4}$$

where z is the shift operator and T the sampling interval (Hori, Mori and Nikiforuk, 1994).

Assuming that a digital control signal is applied via a zero-order hold, the discrete Kalman state observer in shift form can be obtained as

$$\hat{\mathbf{x}}(k+1) = \mathbf{A}_q\hat{\mathbf{x}}(k) + \mathbf{B}_q\mathbf{w}(k) + \mathbf{H}_q\left(\mathbf{y}(k) - \mathbf{C}_q\hat{\mathbf{x}}(k)\right) \tag{6.5}$$

where

$$\begin{aligned}
\mathbf{A}_q &= e^{\mathbf{A}T} \\
\mathbf{B}_q &= \left(\int_0^T e^{\mathbf{A}\eta} d\eta\right)\mathbf{B} \\
\mathbf{C}_q &= \mathbf{C}
\end{aligned}$$

where the process noise $\mathbf{v}(k)$ and the measurement noise $\mathbf{e}(k)$ are random, uncorrelated processes with zero mean value and covariance matrices given by

$$E\{\mathbf{v}(k)\mathbf{v}(k)^T\} = \mathbf{Q}_q \tag{6.6}$$

$$E\{\mathbf{e}(k)\mathbf{e}(k)^T\} = \mathbf{R}_q. \tag{6.7}$$

It is well known that eq.(6.5) is optimal in the least-square sense if the gain matrix $\mathbf{H}_q$ is chosen as (Franklin, Powell and Workman, 1990; Åström and Wittenmark, 1990)

$$\mathbf{H}_q(k) = \mathbf{A}_q\mathbf{S}_q\mathbf{C}_q^T\left(\mathbf{R}_q + \mathbf{C}_q\mathbf{S}_q\mathbf{C}_q^T\right)^{-1} \tag{6.8}$$

where $\mathbf{S}_q$ satisfies the steady-state discrete algebraic Riccati equation

$$\mathbf{S}_q = \mathbf{Q}_q + \mathbf{A}_q\mathbf{S}_q\mathbf{A}_q^T - \mathbf{A}_q\mathbf{S}_q\mathbf{C}_q^T\left(\mathbf{R}_q + \mathbf{C}_q\mathbf{S}_q\mathbf{C}_q^T\right)^{-1}\mathbf{C}_q\mathbf{S}_q\mathbf{A}_q^T \tag{6.9}$$

Using eq.(6.4), the discrete-time Kalman filter given in eq.(6.5) can be expressed in the Euler domain as

$$\varepsilon\hat{\mathbf{x}}(k) = \mathbf{A}_\epsilon\hat{\mathbf{x}}(k) + \mathbf{B}_\epsilon\mathbf{w}(k) + \mathbf{H}_\epsilon\left(\mathbf{y}(k) - \mathbf{C}_\epsilon\hat{\mathbf{x}}(k)\right) \tag{6.10}$$

where

$$\mathbf{A}_\epsilon = \frac{\mathbf{A}_q - \mathbf{1}}{T} \tag{6.11}$$

$$\mathbf{B}_\epsilon = \frac{\mathbf{B}_q}{T} \tag{6.12}$$

$$\mathbf{C}_\epsilon = \mathbf{C}_q \tag{6.13}$$

Moreover, the covariance matrices in the Euler form of the discrete-time Kalman filter, eq.(6.8), are defined as

$$\mathbf{Q}_\epsilon = \frac{\mathbf{Q}_q}{T} \tag{6.14}$$

$$\mathbf{R}_\epsilon = T\mathbf{R}_q \tag{6.15}$$

We thus obtain

$$\mathbf{H}_\epsilon = \frac{\mathbf{H}_q}{T} \tag{6.16}$$

It has been shown that the foregoing quantity converges to its counterpart in the continuous-time domain as T approaches zero, i.e., (Salgado Middleton and Goodwin, 1988),

$$\lim_{T \to 0} \mathbf{H}_\epsilon = \mathbf{H} \tag{6.17}$$

where

$$\mathbf{H} = \mathbf{S}\mathbf{C}^T\mathbf{R}^{-1} \tag{6.18}$$

and where $\mathbf{S}$ satisfies the continuous-time Riccati differential equation, namely,

$$\dot{\mathbf{S}} = \mathbf{S}\mathbf{A}^T + \mathbf{A}\mathbf{S} - \mathbf{S}\mathbf{C}^T\mathbf{R}^{-1}\mathbf{C}\mathbf{S} + \mathbf{Q} \tag{6.19}$$

Furthermore, the discrete covariance matrices converge to the corresponding continuous matrices as T approaches zero, i.e.,

$$\lim_{T \to 0} \mathbf{R}_\epsilon = \mathbf{R} \tag{6.20}$$

$$\lim_{T \to 0} \mathbf{Q}_\epsilon = \mathbf{Q} \tag{6.21}$$

In conclusion, the discrete-time Kalman filter in Euler form can be evaluated in the continuous-time domain using the aforementioned relations between the discrete and continuous cases. What follows is that the performance specified in the continuous-time domain can be readily transformed into the discrete-time domain using the Euler operator.

The LQG compensator in Euler form is also given by

$$\mathbf{w}(k) = -\mathbf{L}(\hat{\mathbf{x}}(k) - \mathbf{x}_r(k)) \tag{6.22}$$

where $\mathbf{x}_r(\cdot)$ is the reference state and $\mathbf{L}$ is chosen to minimize the following cost function:

$$J = \frac{T}{2}\sum_{0}^{N-1}[\mathbf{x}^T(k)\mathbf{Q}^*\mathbf{x}(k) + \mathbf{w}^T(k)\mathbf{R}^*\mathbf{w}(k)] \tag{6.23}$$

while subject to the following constraint:

$$\varepsilon\mathbf{x}(k) = \mathbf{A}_\epsilon\mathbf{x}(k) + \mathbf{B}_\epsilon\mathbf{w}(k) \tag{6.24}$$

The matrix $\mathbf{Q}^*$ is symmetric and positive-semidefinite, while $\mathbf{R}^*$ is positive-definite.

6.4 Robustness of the Digital Control Laws

The bound that quantitatively measures the allowable level of nonlinear perturbations in the continuous LQ state feedback is extended to consider discrete time realizations of the continuous time state feedback in the presence of nonlinear perturbations. For simplicity, we conduct the robustness analysis for a single-input-single-output system. Such an analysis provides a way to express the robustness property of the discrete-time LQ state feedback in terms of bounds on the perturbations.

6.4.1 The Shift Operator

The discrete-time system representation using the shift form can be written as

$$\mathbf{x}(k+1) = \mathbf{A}_q\mathbf{x}(k) + \mathbf{b}_q u(k) + \mathbf{g}(\mathbf{x}(k), u(k)) \tag{6.25}$$

where the vector $\mathbf{g}(x(k), u(k))$ denotes the nonlinear perturbations associated with the discrete-time realizations due to finite-word-length effects such as roundoff errors.

The control input is then assumed to be generated by the linear model

$$\mathbf{x}(k+1) = \mathbf{A}_q\mathbf{x}(k) + \mathbf{b}_q u(k) \tag{6.26}$$

such that

$$u(k) = -\mathbf{k}_q^T\mathbf{x}(k) \tag{6.27}$$

Here, $\mathbf{k}_q$ is the steady-state, discrete-time controller gain, which minimizes the continuous-time cost function given by

$$J = \frac{1}{2}\int_{k=0}^{Nh} \left(\mathbf{x}^T(t)\mathbf{Q}_c\mathbf{x}(t) + q_c u^2(t)\right) d\tau \tag{6.28}$$

in which $\mathbf{Q}_c$ is symmetric and positive-semidefinite, while q_c is a positive real number. In an effort to attain the performance of the LQ state feedback in continuous-time, the discrete equivalent of the continuous cost function is used, namely,

$$J = \frac{1}{2}\sum_{k=0}^{N-1}[\mathbf{x}(k) \;\; u(k)]^T \begin{bmatrix} \mathbf{Q}_{11} & \mathbf{q}_{12} \\ \mathbf{q}_{12}^T & \varsigma_q \end{bmatrix} \begin{bmatrix} \mathbf{x}(k) \\ u(k) \end{bmatrix} \tag{6.29}$$

where

$$\begin{bmatrix} \mathbf{Q}_{11} & \mathbf{q}_{12} \\ \mathbf{q}_{12}^T & \varsigma_q \end{bmatrix} = \int_0^T \begin{bmatrix} \mathbf{A}_q^T & \mathbf{0} \\ \mathbf{b}_q^T & 1 \end{bmatrix} \begin{bmatrix} \mathbf{Q}_c & \mathbf{0} \\ \mathbf{0}^T & q_c \end{bmatrix} \begin{bmatrix} \mathbf{A}_q & \mathbf{b}_q \\ \mathbf{0}^T & 1 \end{bmatrix} d\tau \tag{6.30}$$

An algorithm for obtaining the solution of eq.(6.30) is well established (Van Loan, 1978) and is readily available in commercial software packages. It should be noted that the resulting discrete weighting matrices include cross terms, containing the product of $\mathbf{x}$ and u. Such cross terms can be eliminated by defining a fictitious control input (Bryson and Ho, 1969) such that

$$u_f = \boldsymbol{\sigma}^T \mathbf{x} + u \tag{6.31}$$

where $\boldsymbol{\sigma} = \frac{1}{\varsigma_q}\mathbf{q}_{12}$. Then, eq.(6.29) becomes

$$J = \frac{1}{2}\sum_{k=0}^{N-1} [\mathbf{x}(k) \;\; u_f(k)]^T \begin{bmatrix} \boldsymbol{\Psi}_q & \mathbf{0} \\ \mathbf{0}^T & \varsigma_q \end{bmatrix} \begin{bmatrix} \mathbf{x}(k) \\ u_f(k) \end{bmatrix} \tag{6.32}$$

where

$$\boldsymbol{\Psi}_q \equiv \mathbf{Q}_{11} - \mathbf{q}_{21}\boldsymbol{\sigma}^T \tag{6.33}$$

The desired gain is then obtained by virtue of eq.(6.31), namely,

$$\mathbf{k}_q = \mathbf{k}_f + \boldsymbol{\sigma} \tag{6.34}$$

where

$$\mathbf{k}_f = \left(\varsigma_q + \mathbf{b}_q^T \mathbf{S}_q \mathbf{b}_q\right)^{-1} \mathbf{A}_q^T \mathbf{S}_q^T \mathbf{b}_q \tag{6.35}$$

while $\mathbf{S}_q$ satisfies the following discrete algebraic Riccati equation

$$\mathbf{O} = \mathbf{S}_q - \mathbf{A}_q^T \mathbf{S}_q \mathbf{A}_q + \left(\varsigma_q + \mathbf{b}_q^T \mathbf{S}_q \mathbf{b}_q\right)^{-1} \mathbf{A}_q^T \mathbf{S} \mathbf{b}_q \mathbf{b}_q^T \mathbf{S}_q^T \mathbf{A}_q - \boldsymbol{\Psi}_q \tag{6.36}$$

The closed-loop system is thus obtained by

$$\mathbf{x}(k+1) = \boldsymbol{\Phi}_q \mathbf{x}(k) + \mathbf{g}(\mathbf{x}(k)) \tag{6.37}$$

where

$$\mathbf{\Phi}_q = \mathbf{A}_q - \mathbf{b}_q\mathbf{k}_q^T \tag{6.38}$$

In eq.(6.37), $\mathbf{g}$ becomes a function of only $\mathbf{x}$ after applying the admissible control law.

The following theorem provides a sufficient condition on the nonlinear vector function $\mathbf{g}$ such that the resulting closed-loop system remains stable.

Theorem 6.1 *Let $\mathbf{D}_q$ be the solution of the following discrete time algebraic Lyapunov equation:*

$$\mathbf{\Phi}_q^T\mathbf{S}_q\mathbf{\Phi}_q - \mathbf{S}_q = -\mathbf{D}_q \tag{6.39}$$

The discrete time, closed-loop system given in eq.(6.37) remains asymptotically stable if the nonlinear vector function $\mathbf{g}$ satisfies

$$\frac{\|\mathbf{g}(\mathbf{x})\|}{\|\mathbf{x}\|} < \zeta_q = -1 + \sqrt{1+\kappa}, \ \ \forall\ \mathbf{x} \in \mathbb{R}^{2n} \tag{6.40}$$

where

$$\kappa = \frac{1}{2\,\|\mathbf{D}_q\|_s\|\mathbf{S}_q\|_s} \equiv \frac{\sigma_{min}(\mathbf{D}_q)}{2\sigma_{max}(\mathbf{S}_q)} > 0 \tag{6.41}$$

in which $\|\cdot\|$ and $\|\cdot\|_s$ denote the Euclidean and spectral norms, respectively. Moreover, $\sigma_{max}(\mathbf{S}_q)$ is the largest singular value of $\mathbf{S}_q$, while $\sigma_{min}(\mathbf{D}_q)$ is the smallest singular value of $\mathbf{D}_q$ (See Appendix B for a proof).

6.4.2 The Euler Operator

When expressed in terms of the Euler operator, the discrete-time, closed-loop system given in eq.(6.37) has the form

$$\epsilon\mathbf{x}(k) = \mathbf{\Phi}_\epsilon\mathbf{x}(k) + \mathbf{g}(\mathbf{x}(k)) \tag{6.42}$$

where

$$\mathbf{\Phi}_\epsilon = \mathbf{A}_\epsilon - \mathbf{b}_\epsilon\mathbf{k}_\epsilon^T \tag{6.43}$$

The desired gain is then obtained by

$$\mathbf{k}_\epsilon = \mathbf{k}_f + \boldsymbol{\sigma} \tag{6.44}$$

where $\boldsymbol{\sigma} = \frac{1}{\varsigma_q}\mathbf{q}_{12}$. To use the same cost function as obtained in the shift operator formulation, the fictitious gain $\mathbf{k}_f$ is chosen to minimize the cost function given below:

$$J = \frac{T}{2}\sum_{k=0}^{N-1}[\mathbf{x}(k) \;\; u_f(k)]^T \begin{bmatrix} \boldsymbol{\Psi}_\epsilon & \mathbf{0} \\ \mathbf{0}^T & \varsigma_\epsilon \end{bmatrix} \begin{bmatrix} \mathbf{x}(k) \\ u_f(k) \end{bmatrix} \tag{6.45}$$

where

$$\boldsymbol{\Psi}_\epsilon = \frac{\boldsymbol{\Psi}_q}{T} \tag{6.46}$$

$$\varsigma_\epsilon = \frac{\varsigma_q}{T} \tag{6.47}$$

Finally,

$$\mathbf{k}_\epsilon^T = \left(\varsigma_\epsilon + T\mathbf{b}_\epsilon^T\mathbf{S}_\epsilon\mathbf{b}_\epsilon\right)^{-1}\mathbf{b}_\epsilon^T\mathbf{S}_\epsilon\left(\mathbf{1} + T\mathbf{A}_\epsilon\right) \tag{6.48}$$

where $\mathbf{S}_\epsilon$ satisfies the following discrete-time Riccati equation (Middleton and Goodwin, 1990)

$$\mathbf{O} = \boldsymbol{\Psi}_\epsilon + \mathbf{S}_\epsilon\mathbf{A}_\epsilon + \mathbf{A}_\epsilon^T\mathbf{S}_\epsilon + T\mathbf{A}_\epsilon^T\mathbf{S}_\epsilon\mathbf{A}_\epsilon - \left(\varsigma_\epsilon + T\mathbf{b}_\epsilon^T\mathbf{S}_\epsilon\mathbf{b}_\epsilon\right)^{-1}\mathbf{k}_\epsilon\mathbf{k}_\epsilon^T \tag{6.49}$$

The same sufficient condition as given in Theorem 6.1 can also be written in the Euler form:

Theorem 6.2 *Let* $\mathbf{D}_\epsilon$ *be the solution of the following discrete algebraic Lyapunov equation:*

$$\boldsymbol{\Phi}_\epsilon^T\mathbf{S}_\epsilon + \mathbf{S}_\epsilon\boldsymbol{\Phi}_\epsilon^T + T\boldsymbol{\Phi}_\epsilon^T\mathbf{S}_\epsilon\boldsymbol{\Phi}_\epsilon = -\mathbf{D}_\epsilon \tag{6.50}$$

The discrete time, closed-loop system given in eq.(6.42) remains asymptotically stable if the nonlinear vector function $\mathbf{g}$ *satisfies*

$$\frac{\|\mathbf{g}(\mathbf{x})\|}{\|\mathbf{x}\|} < \zeta_\epsilon = \frac{1}{T}\left(-1 + \sqrt{(1 + T\kappa)}\right) \tag{6.51}$$

where

$$\kappa = \frac{1}{2\,\|\mathbf{D}_\epsilon\|_s \|\mathbf{S}_\epsilon\|_s} \equiv \frac{\sigma_{min}(\mathbf{D}_\epsilon)}{2\,\sigma_{max}(\mathbf{S}_\epsilon)} > 0 \tag{6.52}$$

in which $\|\cdot\|$ *and* $\|\cdot\|_s$ *denote the Euclidean and spectral norms, respectively. Moreover,* $\sigma_{max}(\mathbf{S}_\epsilon)$ *is the maximum singular value of* $\mathbf{S}_\epsilon$*, while* $\sigma_{min}(\mathbf{D}_\epsilon)$ *is the minimum singular value of* $\mathbf{D}_\epsilon$ *(See Appendix C for a proof).*

A key aspect of the Euler operator is that all discrete-time quantities converge to the corresponding continuous-time quantities as the sampling rate increases, whereas these convergences are not obvious when using the shift operator. To prove the convergence of the discrete-time solution to the corresponding solution for the underlying continuous-time problem, the limit of the partial derivative of eq.(6.51) with respect to T, as the sampling interval approaches zero, is taken, namely,

$$\lim_{T\to 0} \frac{\partial}{\partial T}(1 + T\kappa)^{1/2} = \frac{1}{2}\kappa = \frac{\sigma_{min}(\mathbf{D}_\epsilon)}{2\,\sigma_{max}(\mathbf{S}_\epsilon)} \tag{6.53}$$

Moreover, the following relations are known to hold (Middleton and Goodwin, 1990):

$$\lim_{T\to 0} \sigma_{min}(\mathbf{D}_\epsilon) = \sigma_{min}(\mathbf{D}) \tag{6.54}$$

$$\lim_{T\to 0} \sigma_{max}(\mathbf{S}_\epsilon) = \sigma_{max}(\mathbf{S}) \tag{6.55}$$

Then,

$$\lim_{T\to 0} \zeta_\epsilon = \zeta \tag{6.56}$$

where ζ is defined in Theorem 5.1.

The preceding result shows that the results obtained using the Euler operator are close representations of the corresponding continuous-time results when a high sampling rate is used.

6.4.3 Simulation Results

Simulation studies have been performed to assess the allowable level of nonlinear perturbations arising from the use of discrete-time LQ state feedback. In these studies, the rotating flexible beam whose material properties are given in Table 5.1 is used as a model to be controlled. The vibrational behaviour of the beam is described using cubic splines.

The discrete-time LQ state feedback control law is then formulated using both the Euler and the shift operators. The tolerable bounds for nonlinear perturbations, given in Theorems 6.1 and 6.2, are evaluated in terms of the sampling interval and the penalizing factors in their weighting matrices. It should be noted that the discrete cost functions, for both the Euler and the shift operator formulations, are obtained in such a way that they are equivalent to an analog cost function in continuous time. This will provide a fair basis for comparison of the aforementioned discrete-time systems relative to the continuous-time system.

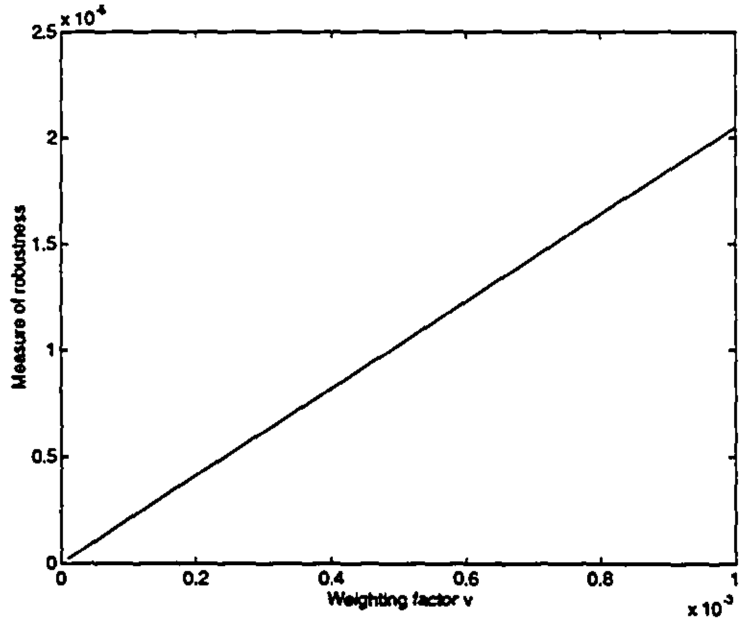

Figure 6.2: Measure of robustness ζ for the continuous time LQ state feedback

To facilitate the comparison, the robustness bound for the continuous-time LQ state feedback, given in Theorem 5.1, is calculated with the cost function given in eq.(5.9), whose weighting matrices are given in eq.(5.36). In general, if the state variables associated with position are only penalized by $\mathbf{Q}$, then the response becomes more oscillatory and larger overshoots occur (Athans, 1971). To avoid these drawbacks, the time-rate of change of such variables are also penalized by varying the weighting factor v in $\mathbf{Q}$ (Fig. 6.2). This implies that the robustness bound increases as the weighting factor v increases.

Identical conditions are used for discrete-time LQ state feedback based on both the Euler and the shift operators. The robustness bounds can then be evaluated in terms of the sampling interval T and the weighting factor v. The robustness envelop obtained using the shift operator shows that the robustness bound increases as the penalizing factor v is increased, whereas the bound decreases as the sampling rate is increased (Fig. 6.3). In fact, when using the shift operator, the obtainable bound is reduced by as much as about 2 orders of magnitude, compared to the continuous case. Consequently, the said digital control system may become more sensitive to parameter variations and more vulnerable to disturbances as the sampling rate increases. This is contrary to the commonly made assumption that the performance of a digital controller improves as the sampling rate is increased.

On the other hand, the bound envelops obtained using the Euler operator shows that the robustness bound increases as both the penalizing factor and sampling rate are increased (Fig. 6.4). Moreover, the overall magnitude tends to converge to that of the continuous-time case as the sampling rate increases. This suggests that a higher sampling rate allows the continuous-time system to be better approximated by the discrete-time system based on the Euler operator.

It should be mentioned that unacceptable regions exist for nonlinear perturbations in both the shift and the Euler operators, and they occur at the same sampling rate (Figs. 6.3 and 6.4). This implies that such regions are independent of the choice of operator, but rather dependent on the selection of the sampling interval. Such phenomenon, explained by Franklin, Powell and Workman (1990) and Powell and

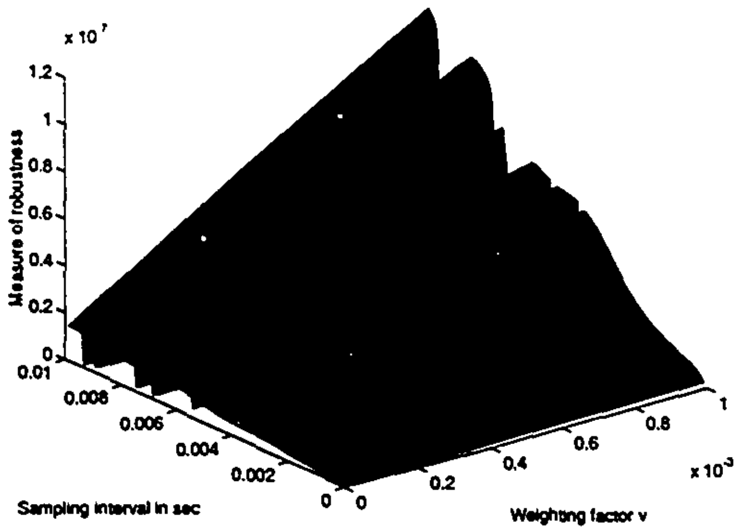

Figure 6.3: Measure of robustness ζ_q using the shift operator

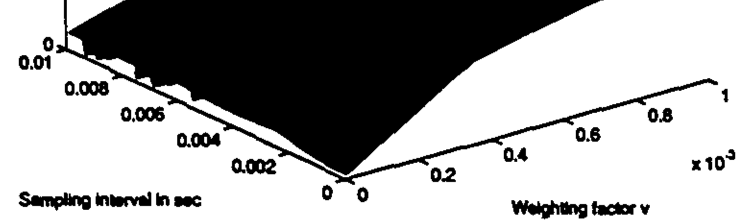

Figure 6.4: Measure of robustness ζ_ϵ using the Euler operator

Katz (1975), is induced by the discrete-time state feedback for a plant possessing multiple bending modes with a sampling rate which is slower than twice the selected open-loop plant resonance. Under this situation, the controller has no information about the resonance, thereby producing an uncontrollable system.

Considering that the plant to be controlled possesses higher-frequency bending modes, the sampling rate has to be chosen in such a way that the unacceptable regions for the nonlinear perturbations are avoided. Hence, the preceding analysis not only provides the robustness bound, but also gives us a guideline to choose a proper sampling rate.

Chapter 7

Numerical and Experimental Results

7.1 Desired Trajectory of the Mechanism

The desired trajectory of the mechanism is chosen such that the coupler and output links undergo doublet-type of excitations in their acceleration profiles, when the input link rotates at a constant angular speed (Fig. 7.1). This is to show clearly the higher modes of the flexible members that may not be apparent otherwise. In this way, the control scheme can be tested even in the presence of high-frequency residual vibrations. Such tests are of practical importance to ensure the performance of the control scheme in real-time without using low-pass filters.

It is known that the use of low-pass filters may be essential for the successful control of a system with multiple high-frequency modes due to observation and control spillovers. High-frequency residual vibrations are sensed and fed back to the control system, thereby losing stability due to the lack of control action to cope with those high-frequency residual vibrations (Gibson and Adamian, 1991; Balas, 1982). Although low-pass filters are effective in dealing with residual vibrations, they can cause a phase shift in the control system and may degrade the system responses.

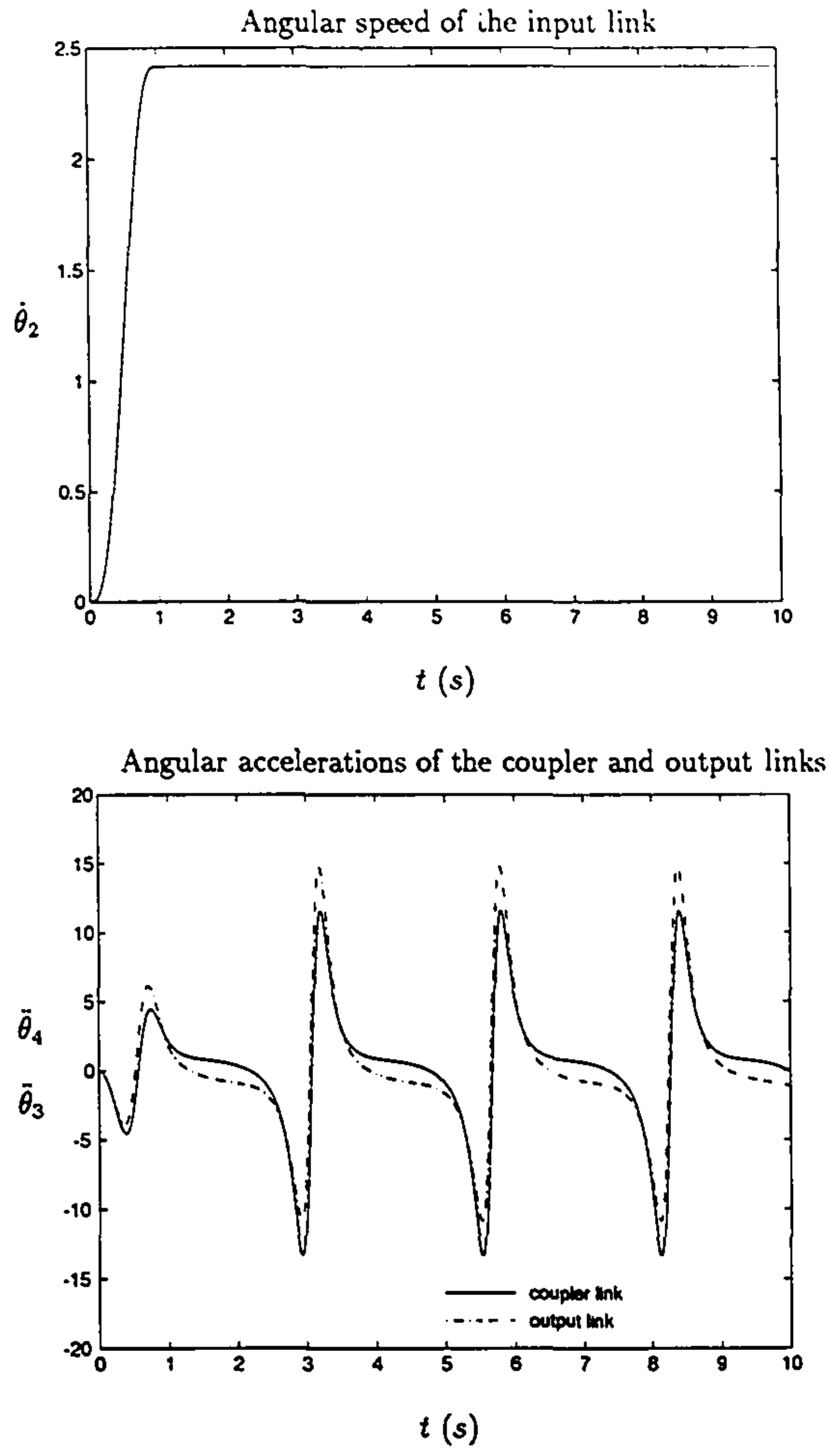

Figure 7.1: Desired angular speed of the input link [rad/s] & consequent angular accelerations of the coupler and input links [rad/s^2]

It is also well known that some four-bar mechanism possess intrinsic singular configurations known as *dead points*. These configurations represent mathematically the vanishing of a denominator. In anticipation of the distorted system response due to the presence of the singular configurations, the dynamic behaviour of the mechanism in the neighbourhood of these dead points should be observed carefully. Moreover, such observations allow us to determine the performance of the control system in terms not only of suppression of the vibration, but also of trajectory tracking.

In summary, the way we choose the desired trajectory is to examine two aspects of the performance of the proposed control scheme: one is a reliability of the control scheme in the presence of high-frequency residual vibrations; the other is a capability of the control scheme to attain the desired rigid-body motion in the presence of singular configurations.

7.2 Outline of the Simulation Algorithm

The algorithm used for simulation of the flexible four-bar mechanism is summarized as follows:

- Linearize the decoupled equations of motion given in eq.(4.53).
- Construct an LQG compensator based on the linearized equations of motion.
- Provide an initial value of $\mathbf{x}_i$.
- **for** $k = 1, \cdots, t_f/T$ **do**
    - Compute the NOC filter given in eq.(3.75).
    - Compute the reference state $\mathbf{x}_r$.
    - Compute the generalized forces $\mathbf{w}$ from the admissible control law as described in eq.(6.22).
    - Compute the applied torque τ using eq.(6.3).

- Regard the torque obtained as a step function during the interval ($0 \leq t \leq T$).
- `for` $t \leq T$ `do`
  - Integrate the nonlinear coupled equations of motion, given in eq.(4.67), using Gear's method.
- `enddo`
- Set $\mathbf{x}$ to the value obtained after the integration, $\mathbf{x}_i = \mathbf{x}_f$
- Obtain the estimated state using the Kalman filter.

- `enddo`

It is noteworthy that the underlying equations of motion consist of highly coupled nonlinear ordinary differential equations. They are also *stiff* in the sense that the ratio between the largest and smallest eigenvalues is large (Gear, 1971). Considering that eigenvalues indicate the speed of response of the system, a large eigenvalue implies a rapidly changing solution and a small eigenvalue corresponds to the slowly changing part of the solution. For the flexible four-bar mechanism, the former reflects the elastic motions while the latter pertains to the rigid-body motion. Since Gear's method is known to be suitable for stiff systems, the numerical integration of the nonlinear system of equations is carried out using Gear's method. The whole scheme is implemented in MATLAB.

7.3 Experimental Setup

To test the validity of the theoretical works discussed in the preceding chapters, the proposed control scheme has been applied to the prototype mechanism (Fig. 7.2). The mechanism is a planar four-bar linkage of the crank-rocker type, having a chain of structurally flexible links. The links are made of aluminum beams with a cross section of 3mm $\times$ 30mm. The large thickness-to-width ratio is used to prevent unwanted

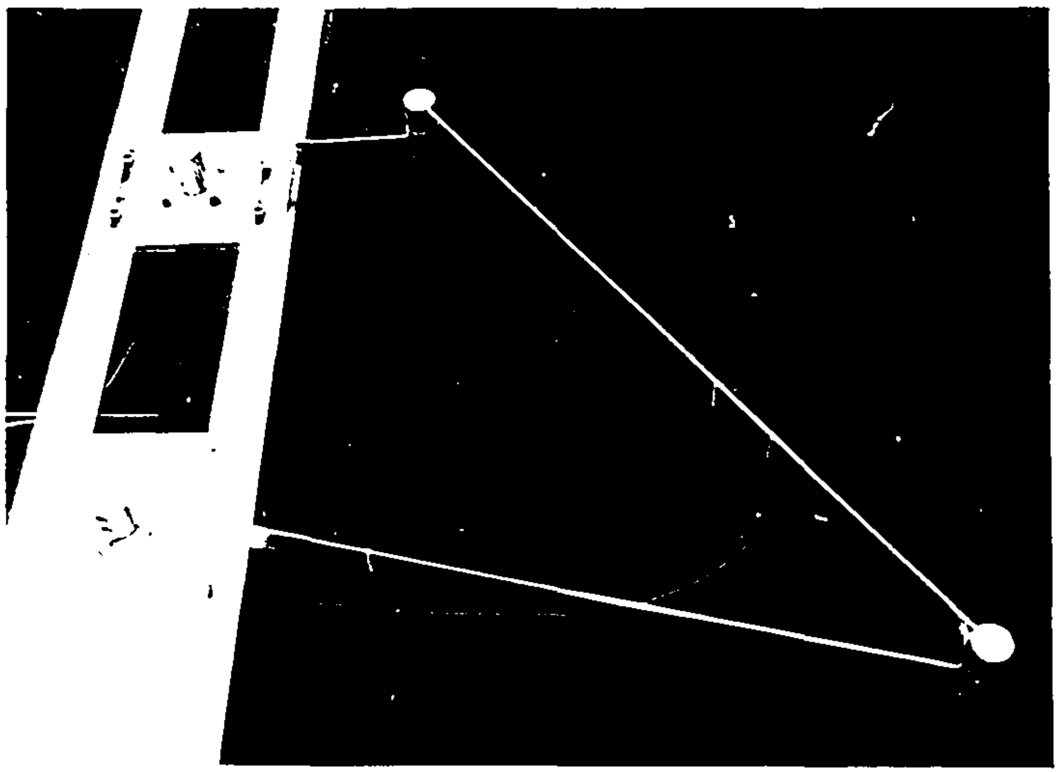

Figure 7.2: The prototype four-bar mechanism

vertical vibrations. The mechanism is thus subject to only transverse vibrations. In addition, the kinematic couplings are achieved using single-row angular contact bearings at each joint. Special care is taken in designing joints in order to make their weights as light as possible, while obtaining accurate couplings. The mechanical specification and material properties are given in Table 7.1.

In the prototype mechanism, the coupler and output links are considered flexible and their elastic motions are modelled using cubic splines. The input link is then considered as a rigid body because of its short length relative to its cross-section. Each flexible link contains five equally spaced nodal points.

It should be recognized that the desired angular speed of the input link is a step type of input. Hence, the acceleration of the input link would vanish unless disturbed. This implies that the input link will undergo considerably less vibration compared to the rest of the links.

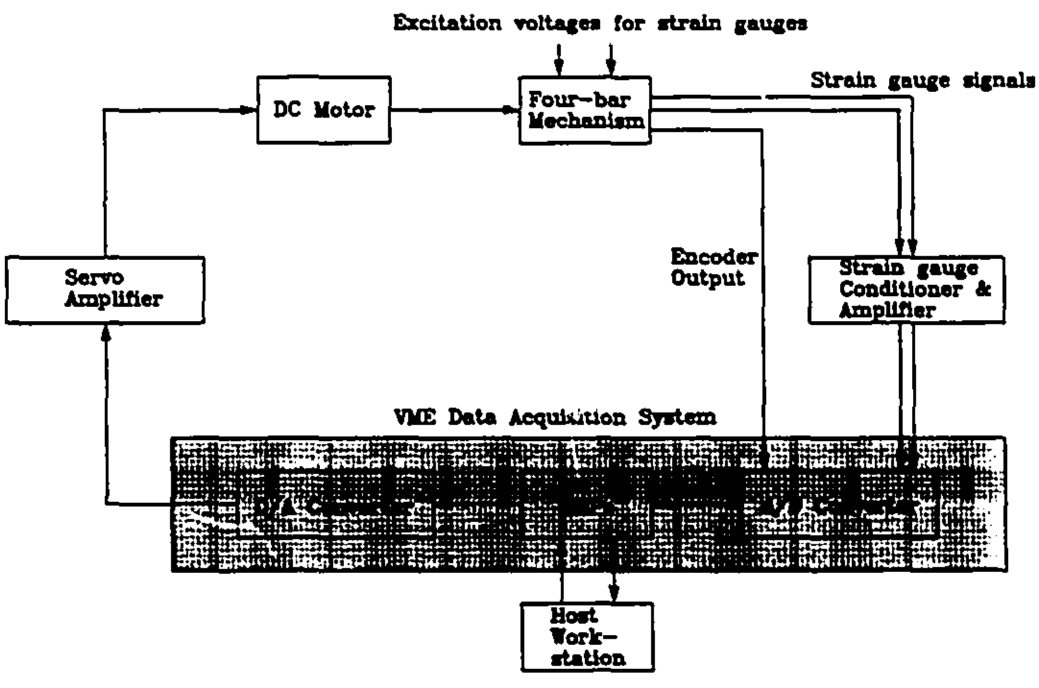

Figure 7.3: Schematic diagram of the experimental setup

A VME board comprising two 33M-flops digital signal processors (DSP) is used to execute the control algorithm and to perform the necessary data acquisition. The board is housed in a VME chassis that includes an 8-channel, 16-bit analog-to-digital (A/D) converter as well as a parallel port. A dual channel incremental encoder interface board from Whedco Inc. is also included in the VME chassis in order to acquire position feedback pulses from encoders. Two sets of full-bridge strain gauges are installed at the midspan of the coupler and output links, respectively. The strain gauge signals are then conditioned and amplified through a 2120A strain gauge conditioner with an adjustable bridge balance (Intertechnology Inc.). The digital control signal generated passes through a 16-bit digital-to-analog converter (D/A) and is applied to a servo amplifier from Copley Controls Corp. The mechanism is then actuated by a brush-type DC servo motor (model name NH2130-138C) from Cleveland Machine Controls Inc. The whole system is interfaced to a host SPARC station through an SBUS-to-VME bus adapter (Fig. 7.3).

Table 7.1: Material properties of the mechanism

Link	length [m]	mass[kg]		flexural	boundary
		link	joint	rigidity [Nm^2]	conditions
1	0.4	-	-	-	-
2	0.2321	0.0567	0.0613	4.7925	-
3	0.7169	0.1750	0.0613	4.7925	pinned-pinned
4	0.6867	0.1676	0.0613	4.7925	pinned-pinned

7.4 Numerical and Experimental Results

7.4.1 Planar Four-Bar Mechanism

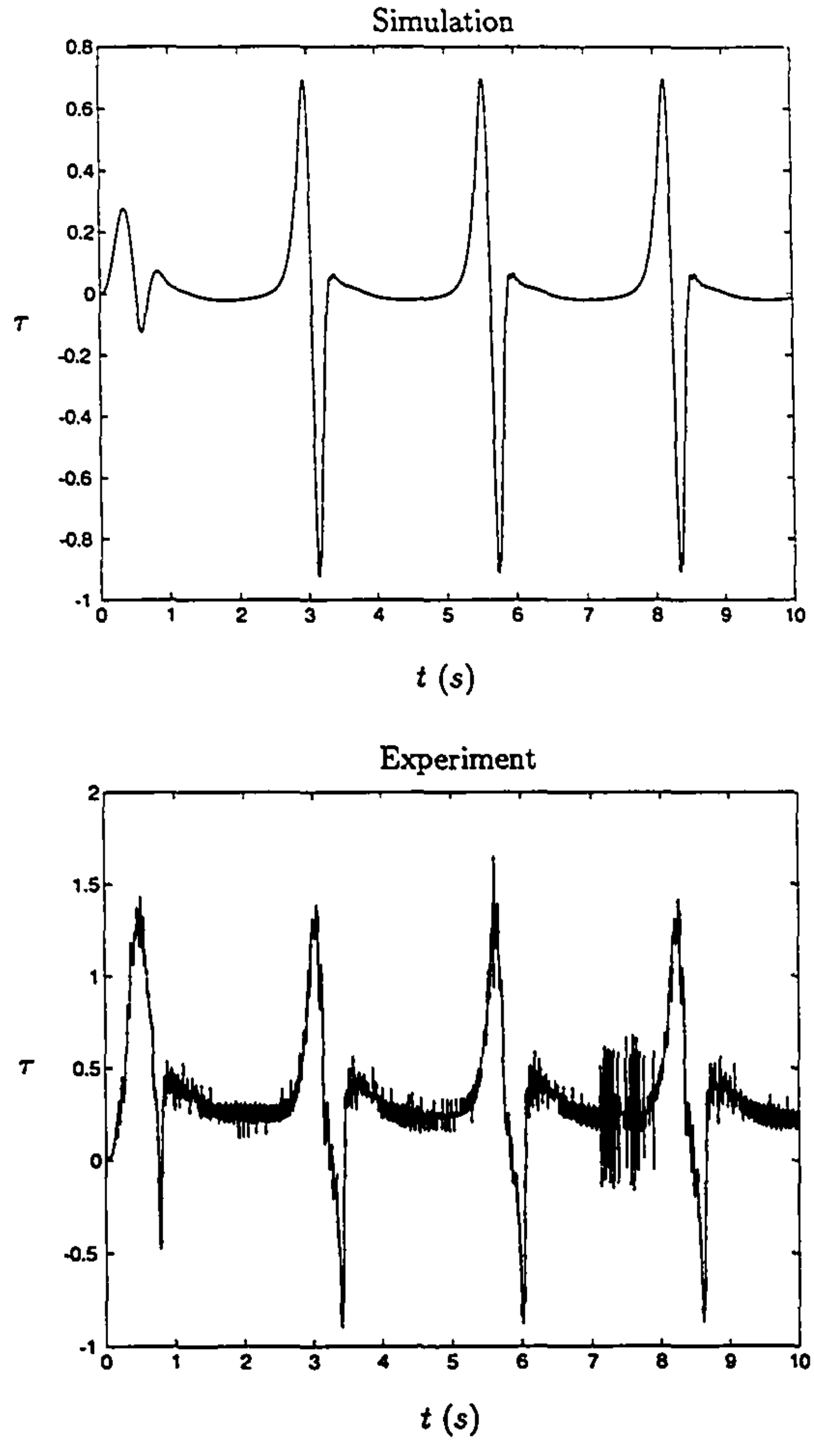

Figure 7.4: Optimum torque profiles of the four-bar mechanism [N-m]

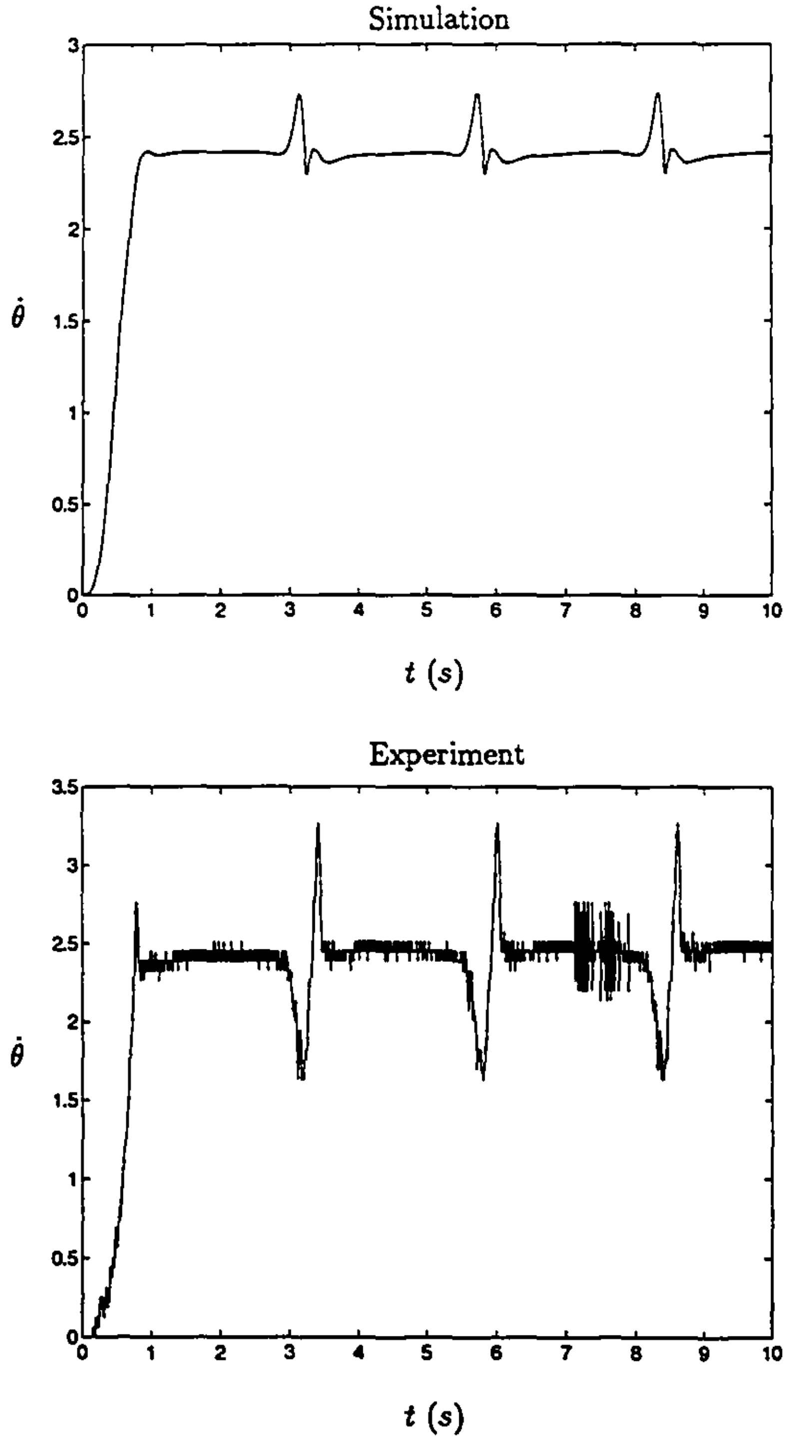

Figure 7.5: Angular speed of the input link [rad/s]

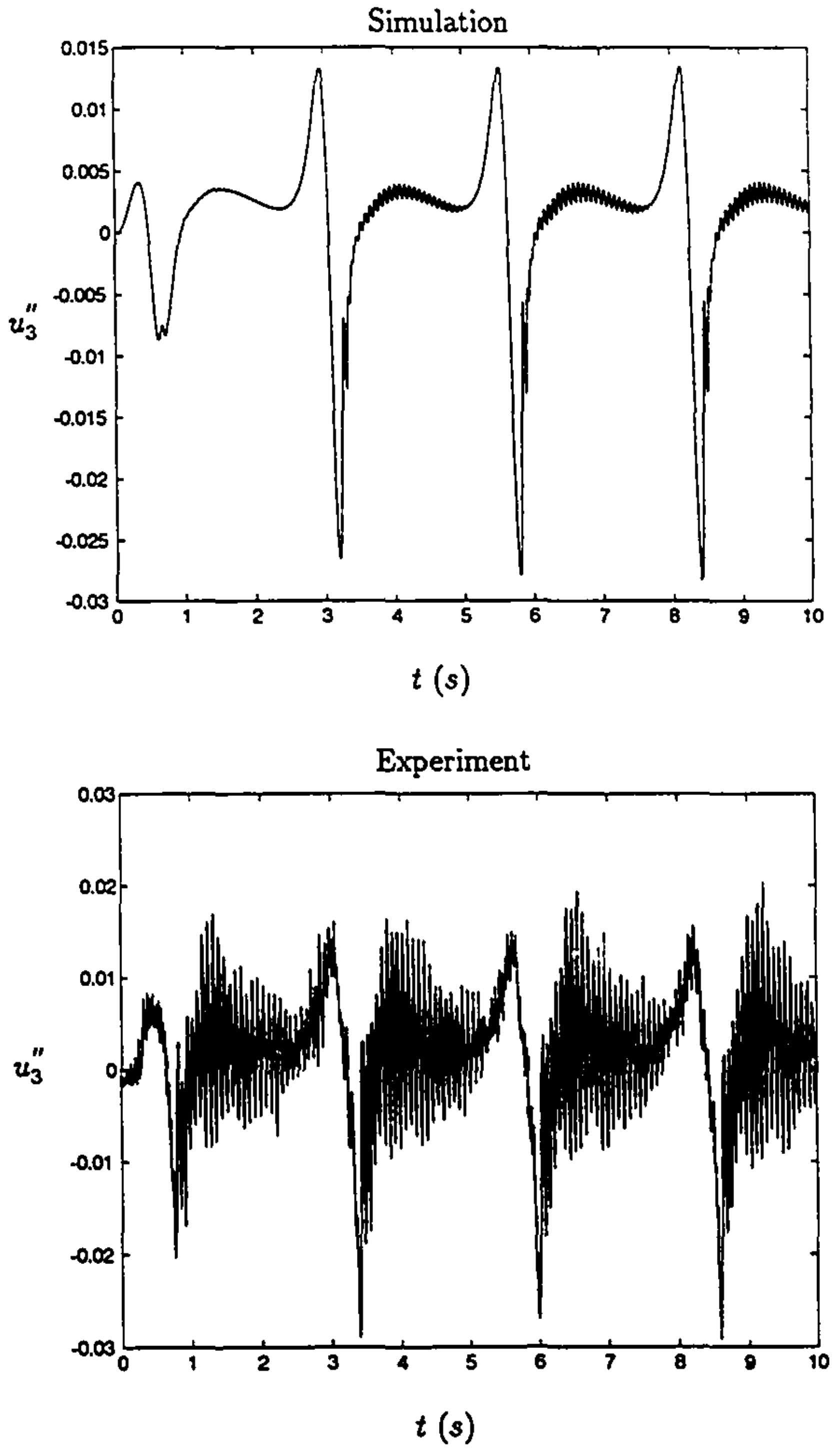

Figure 7.6: Curvature value measured at the midspan of the coupler link [m^{-1}]

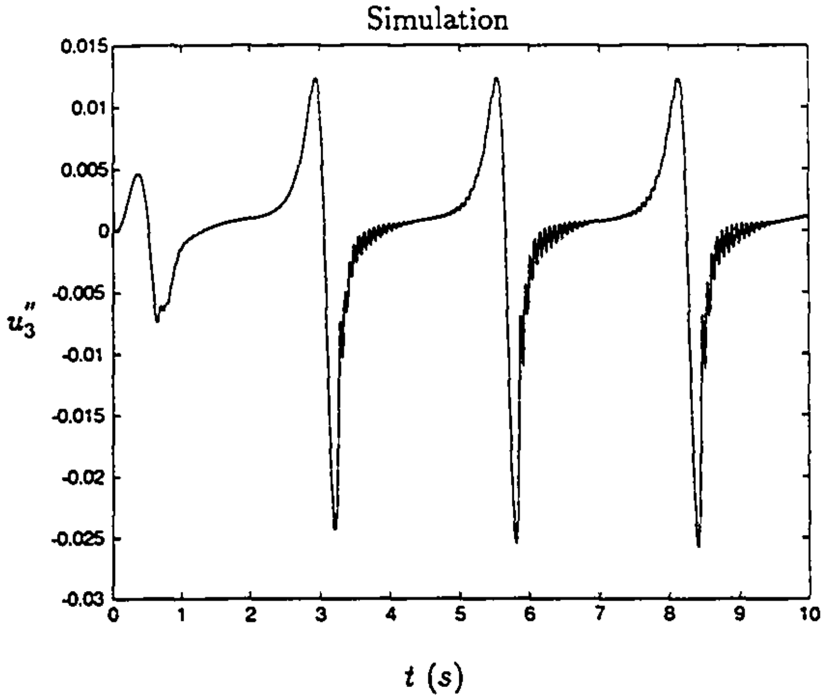

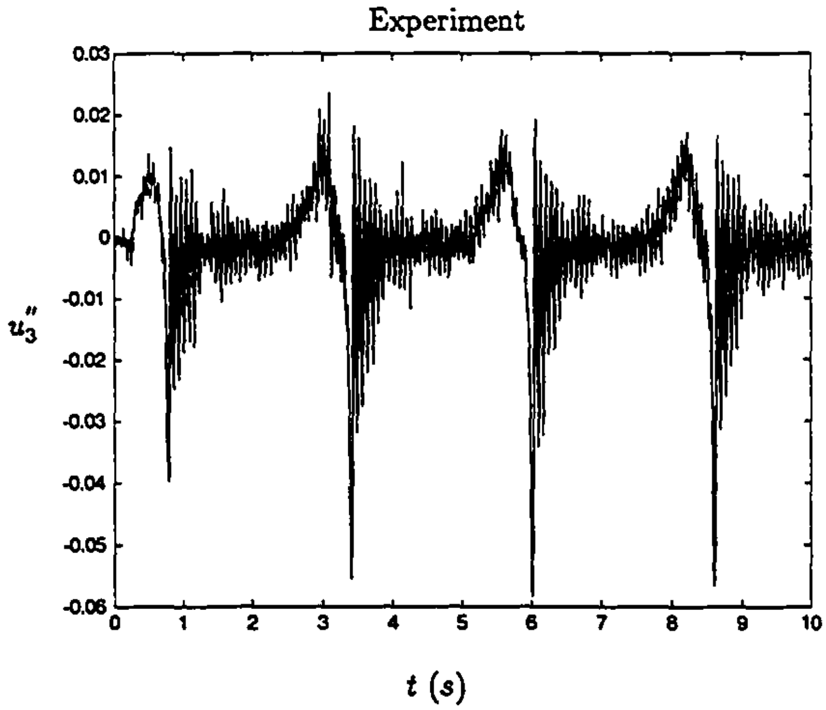

Figure 7.7: Curvature value measured at the midspan of the output link [m^{-1}]

7.4.2 Rotating Flexible Beam

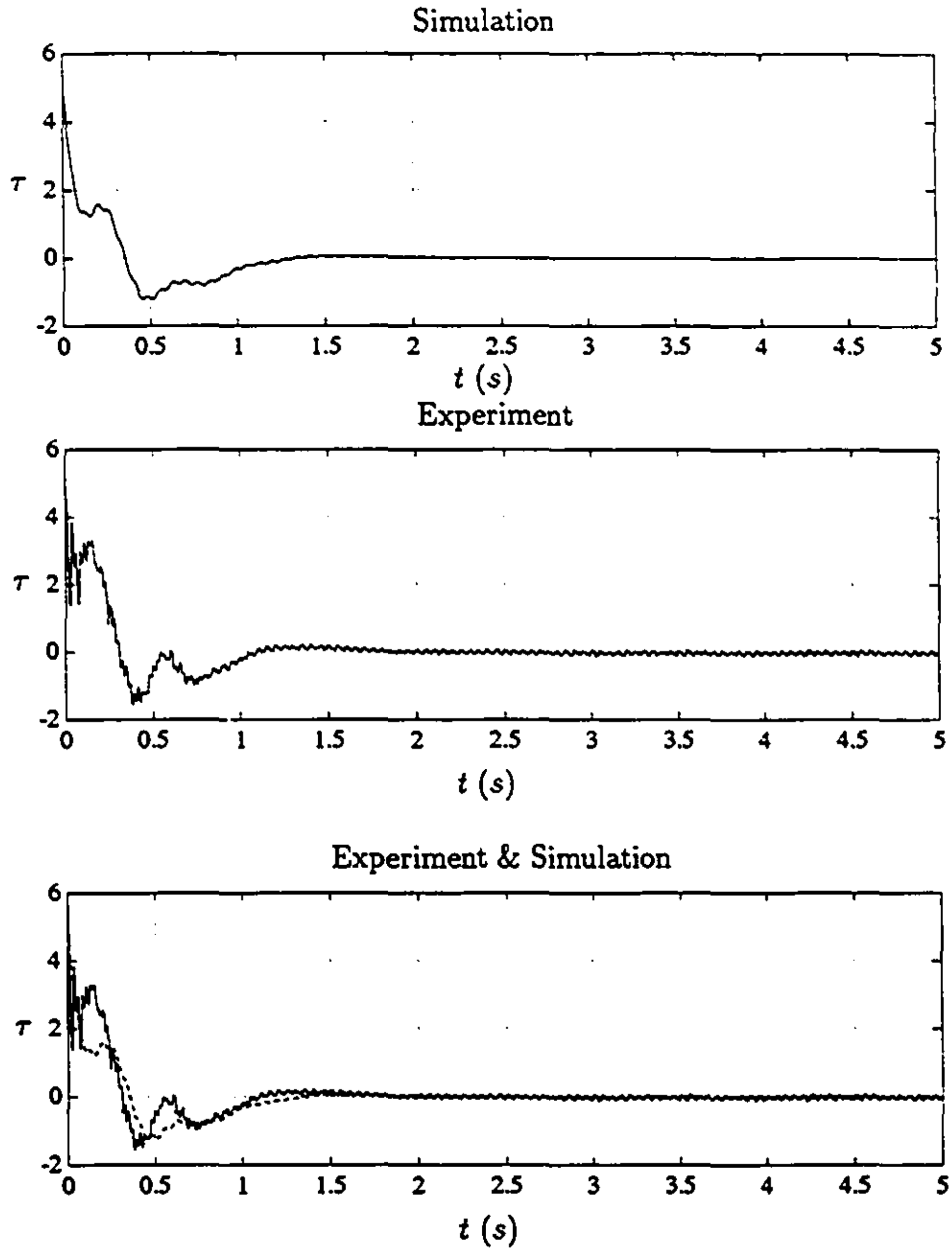

Figure 7.8: Optimum torque profiles for the rotating flexible beam

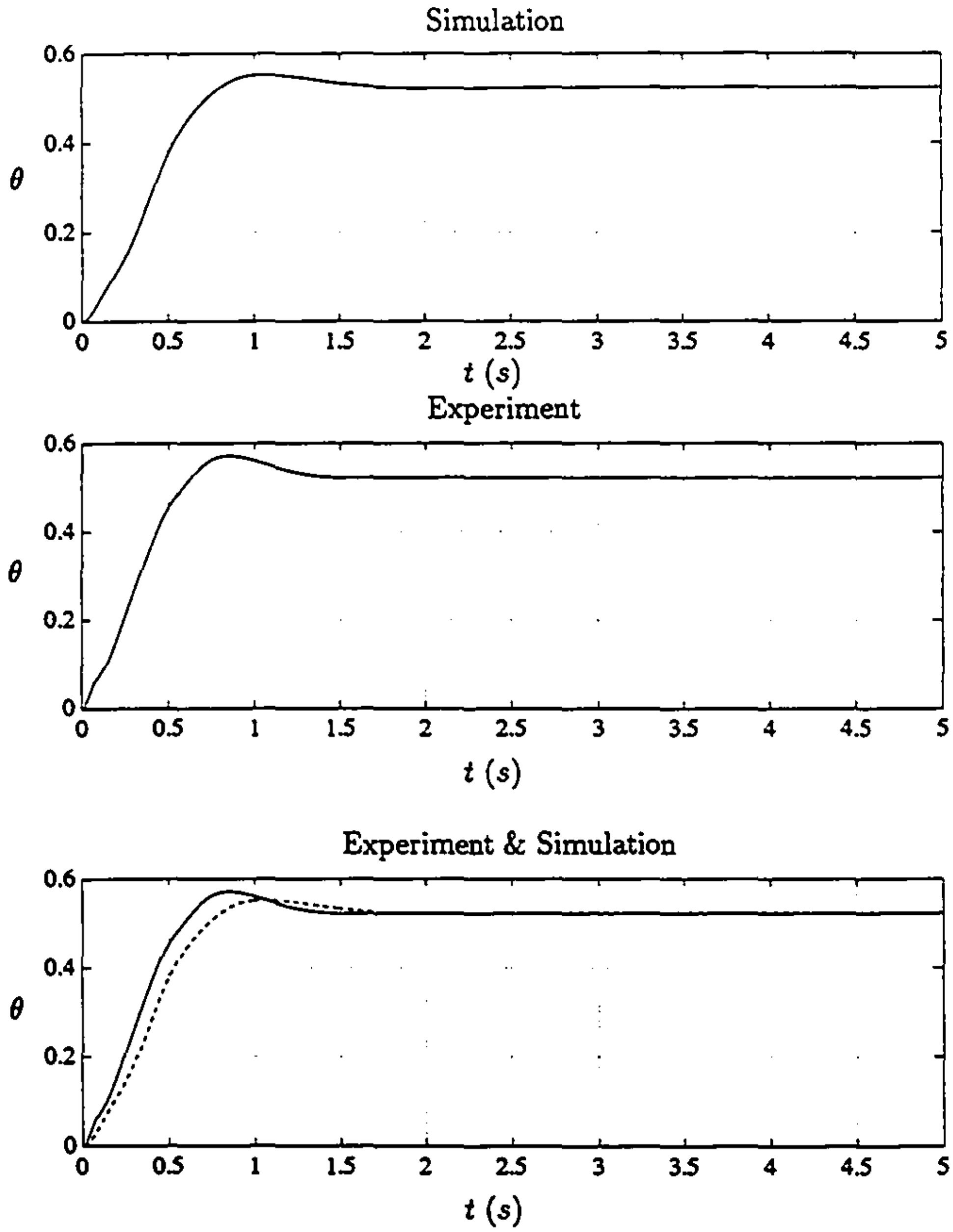

Figure 7.9: Hub rotational angle [rad]

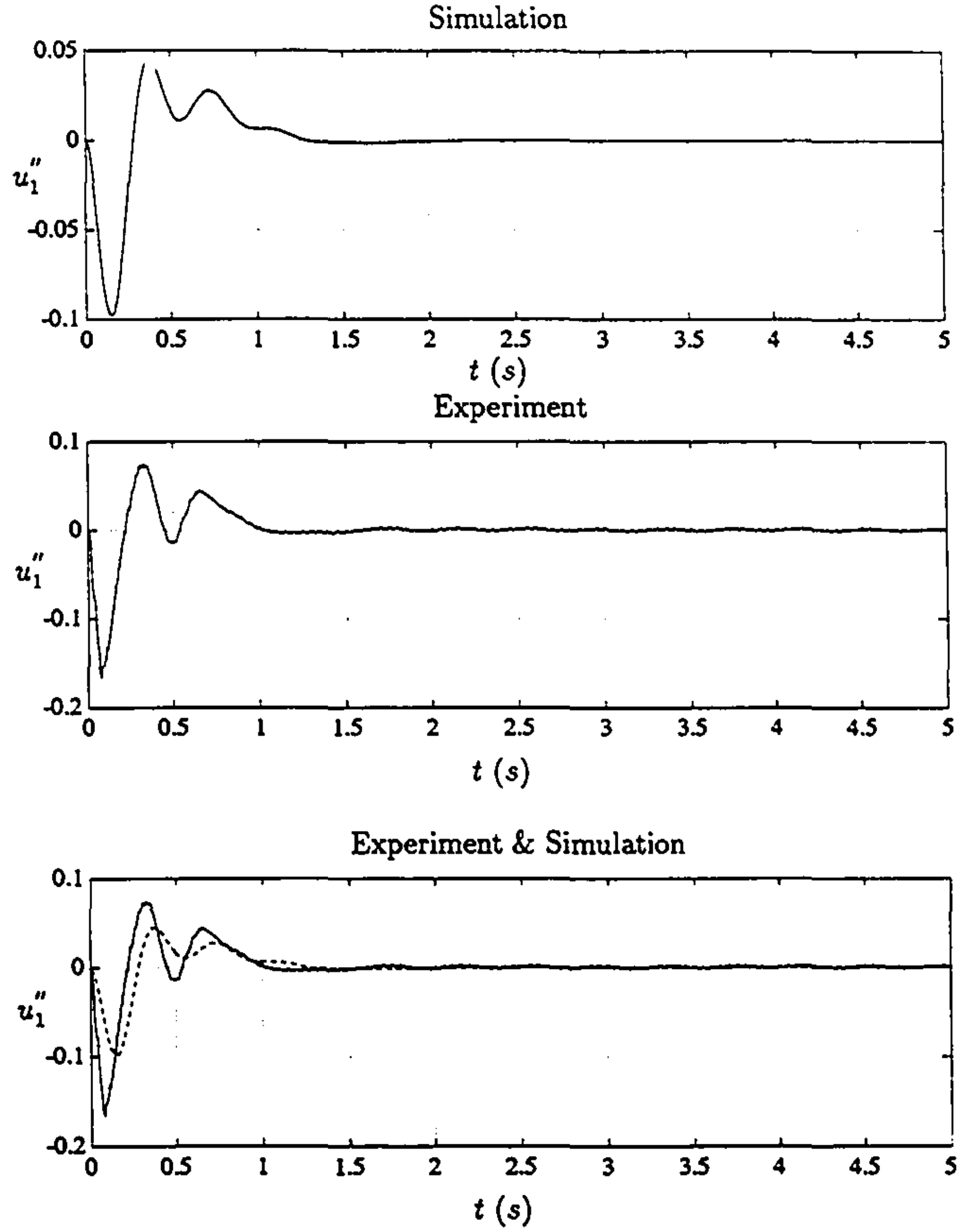

Figure 7.10: Curvature measured at the root of the beam [m^{-1}]

7.5 Discussion

7.5.1 Effects of the Singularities

The mechanism is supposed to provide a constant input angular speed after a certain settling-time period, if the controller works properly. However, the angular speed undergoes a doublet-type of disturbance periodically where the input torque exhibits the same type of fluctuations (Fig. 7.4 and Fig. 7.5). Furthermore, those fluctuations occur in the neighbourhood of the singular configurations of the mechanism. It is thus of practical importance to investigate how the singularities influence the system response coupled with a rapid inertia change.

In order to simplify the singularity analysis, a rigid-body four-bar linkage is considered. It should be noted that the overall motion of the flexible four-bar mechanism is expressed as the superposition of the rigid-body and elastic motions using the equivalent rigid-link system (ERLS). The singularity configurations of the flexible mechanism are then perturbed from those of the corresponding rigid-body mechanism. Hence, the singularity configurations of the flexible mechanism can be inferred from the rigid-body case.

The relation between the input and output speeds of the corresponding rigid-body mechanism is then written as

$$\mathbf{h}\dot{\theta}_2 + \mathbf{J}\dot{\boldsymbol{\theta}} = \mathbf{0} \tag{7.1}$$

where $\boldsymbol{\theta} \equiv [\theta_3 \ \ \theta_4]^T$. Moreover $\mathbf{h}$ is a 2-dimensional vector and $\mathbf{J}$ is a 2×2 Jacobian matrix. A detailed description of the foregoing vector and matrix can be found in (Saha and Angeles, 1991). The singularity of the mechanism occurs when

$$\det(\mathbf{J}) = 0 \tag{7.2}$$

This corresponds to configurations in which the input link is at a dead point. Since in this case the nullspace of $\mathbf{J}$ is not trivial, there exist nonzero output vectors $\dot{\boldsymbol{\theta}}$ (Gosselin and Angeles, 1990). Then, eq.(7.1) holds if and only if the angular speed of the input link becomes zero. Consequently, the angular speed of the input link tends to approach zero at dead points.

When the said mechanism undergoes its full motion cycle, it attains two configurations in which the input link is at dead points (Fig. 7.12). For the sake of convenience, these configurations are further classified depending on how the input link is aligned with the coupler link, namely, type A and B, as shown in Figs. 7.12 and 7.13, respectively.

To illustrate the effects of these singularities in detail, simulations are undertaken using the inverse dynamics of the corresponding rigid-body mechanism, but not using the proposed control scheme. The simulation procedure is given as follows: 1) a desired trajectory at the actuated joints is specified; 2) the torque required to drive the rigid mechanism through the trajectory is computed using inverse dynamics; 3) the torque is then applied to the flexible mechanism. The desired trajectory for the experiment is also used in this case.

It can be seen that the angular speed of the input link closely matches the desired one until the input link approaches the singular configuration of type A from the initial configuration, and then undergoes a steep rising in its response in the neighbourhood of the singularity. This results in a large overshoot in the transient period. Moreover, the signal becomes oscillatory after passing the singular configuration. This behaviour is coupled with an inertia change which was observed in the torque profile obtained using the corresponding rigid-body model.

In contrast to the first singular configuration, the angular speed decreases drastically toward zero until the corresponding input torque begins to increase near the configuration of type B. This corresponds to the anticipated result based on the singularity analysis. But it should be recognized that there is no inertia change observed in the neighbourhood of the singular configuration of type B. This implies that the input angular speed tends to approach zero, if there is no external excitation, across the neighbourhood of the singular configurations.

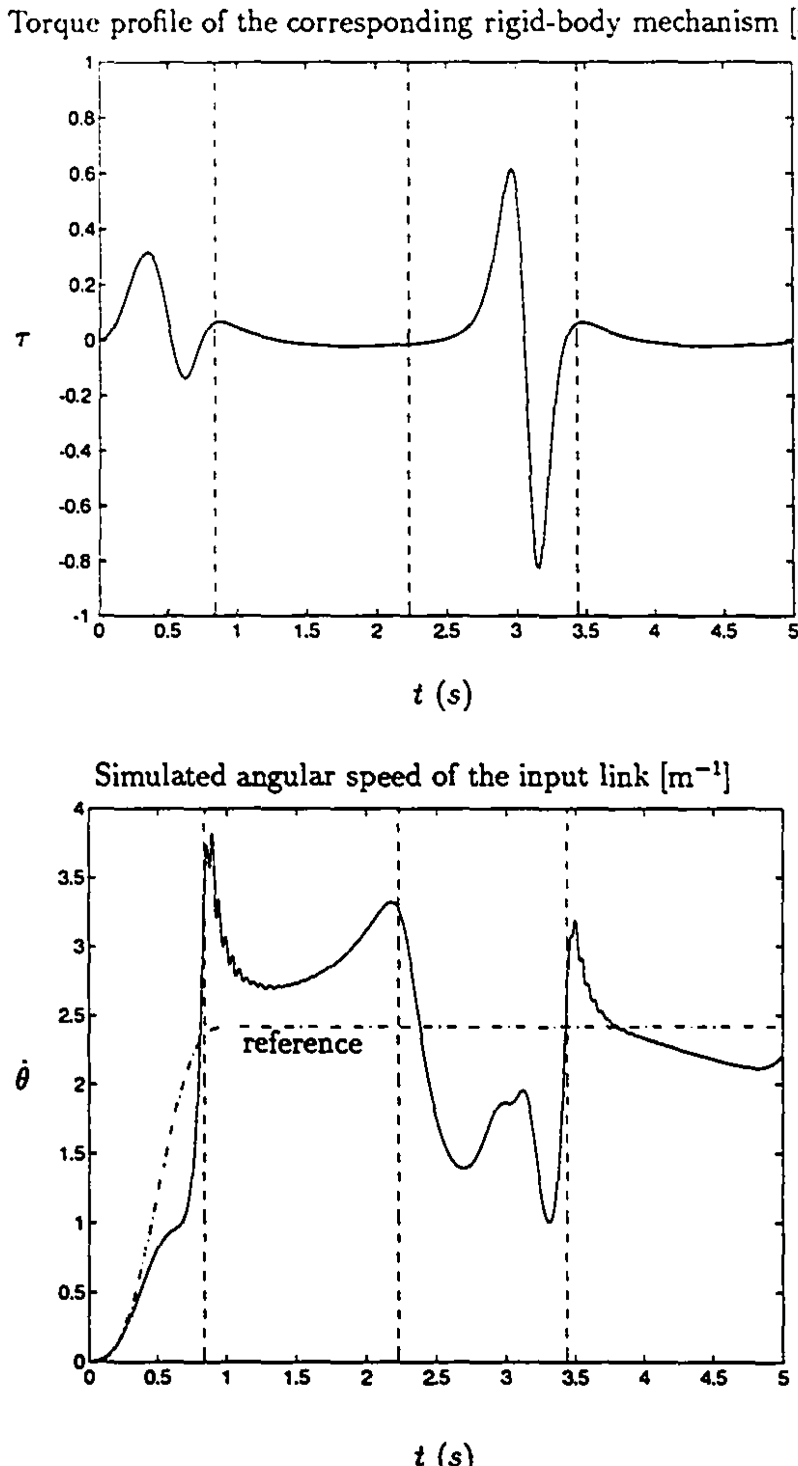

Figure 7.11: Simulated angular speed of the input link with the torque obtained for the corresponding rigid-body mechanism (the dashed lines indicate the places where the input link is at the singular configuration)

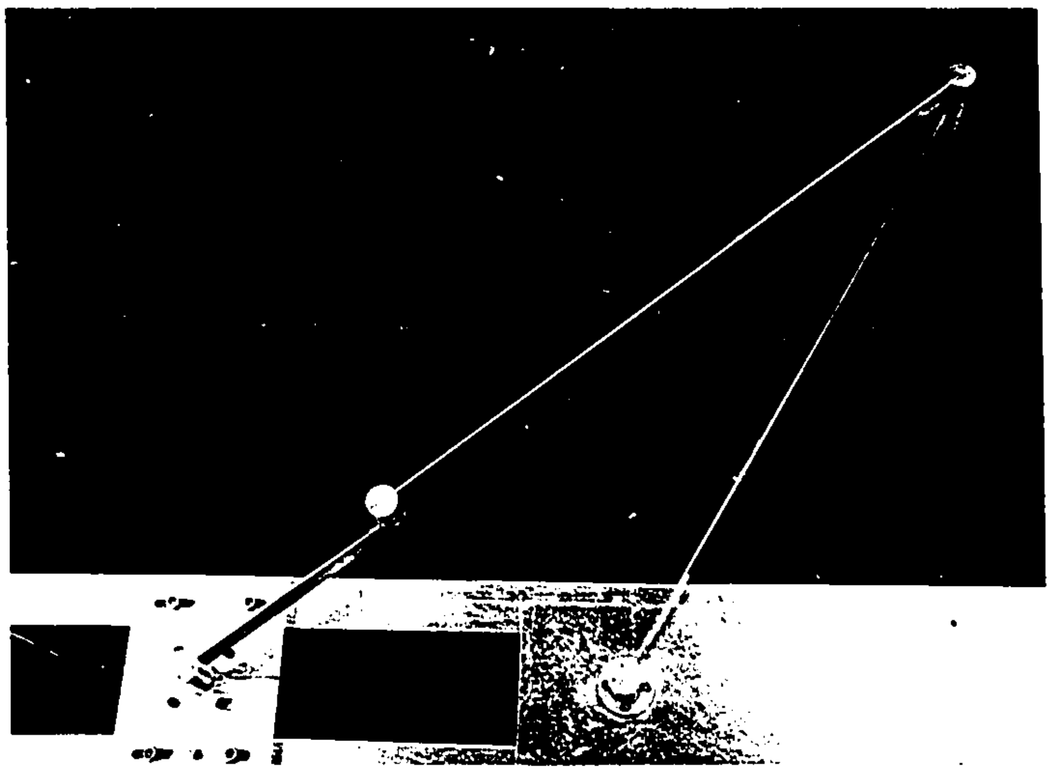

Figure 7.12: Singular configuration of type A

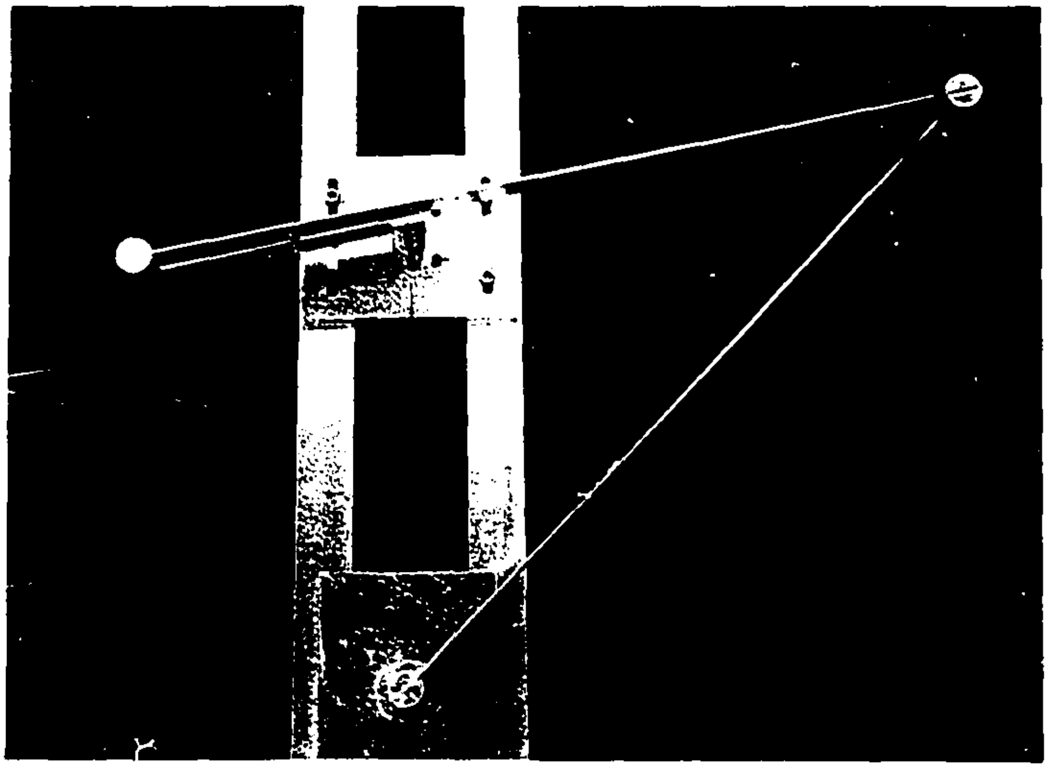

Figure 7.13: Singular configuration of type B

What can be concluded from the foregoing discussion is that care must be taken in the simulation of a flexible mechanical system containing singularities. The open-loop simulation using the inverse dynamics of the corresponding rigid-body model may give rise to results that are quite different from those expected from the rigid-body system. It is thus very dangerous to anticipate the system response of the flexible mechanical system based on the response of the rigid-body system.

7.5.2 Rigid-body Motion Control with a PID Controller

Is it really worth considering link flexibilities in modelling and designing a control scheme for a mechanical system with structurally flexible members? Does the performance of such a control scheme justify the cost required to include the said link flexibilities? To answer these fundamental questions, we resort to a simple PID control scheme. The objective of the control scheme is to achieve trajectory tracking associated with the rigid-body motion. This control scheme is applied to the prototype four-bar flexible mechanism. Control parameters are chosen using the Ziegler-Nichols rule in which the desired rigid-body motion of the input-link is used as a reference.

A key observation made in this experiment is that the performance of the PID controller is proportional to the sampling rate, namely, the performance improves as the sampling rate increases. Comparable results can then be obtained using a relatively higher sampling rate of 1000 Hz.

As for the rigid-body motion, the angular speed of the input link is obtained as shown in Fig. 7.14. It can be seen that the raw signal itself is heavily contaminated with higher-frequency noise arising from an indirect measurement of the angular speed; a finite-difference method is used to estimate the angular velocity instead of a tachometer. Unlike results obtained using the proposed control scheme where the Kalman filter does in some way the role of a low-pass filter, the PID control scheme is very sensitive to such a measurement noise. Moreover, the signal undergoes periodic disturbances resulting from a backlash in the DC motor. Such disturbances are much greater than in the case when the proposed control scheme is used. It should be noted that these disturbances must be distinguished from the doublet-type of disturbance that occurs due to the rapid inertia change coupled with the singularity of the mechanism. This can be readily recognized due to the differences in period. To see the case of using a low-pass filter combined with the PID control scheme, a fourth-order Butterworth digital filter with a cut-off frequency of 0.01 [rad/s] is used to take off the noise.

The result after filtering shows that the notches appearing in the response are much smaller than those obtained using the proposed control scheme (Fig. 7.14). However, the link deflection of the coupler and output links are almost ten times larger than those obtained using the proposed control scheme (Fig. 7.15). Since the PID control scheme is only concerned with the rigid-body motion, such results for the elastic motion are not difficult to anticipate. After all, the suppression of the link vibrations can be achieved after compromising the performance of the rigid-body motion. The proposed control scheme is indeed a compromise between rigid-body trajectory tracking and the suppression of the link vibration. This can further be verified by testing the proposed control scheme under various ranges of operating speeds, while maintaining the same control variables. This can be achieved by simply adjusting the amplitude of the desired angular speed of the input link. Examining the experimental results show that the magnitudes of the notches appearing in the rigid-body response become larger as the operating speed increases (Fig. 7.16). Since higher operating speeds inevitably give rise to larger inertial forces, the controller requires the more adjustment in the rigid-body motion to prevent from degrading the elastic motion. In other words, the proposed control scheme is able to optimize the rigid-body motion and the elastic motion in the manner that is described in the quadratic cost function.

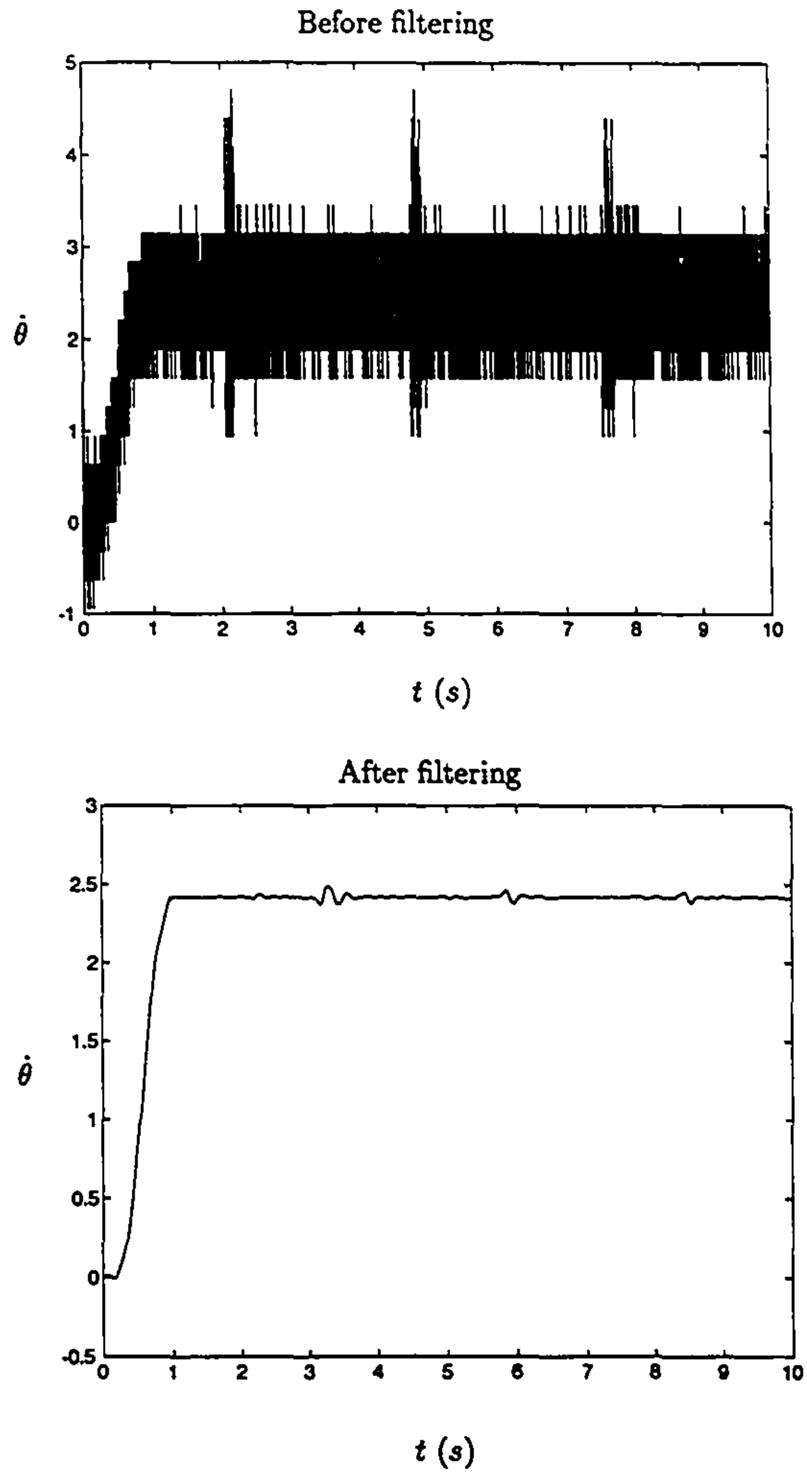

Figure 7.14: Angular speed of the input link when using the PID controller without considering link flexibilities [rad/s]

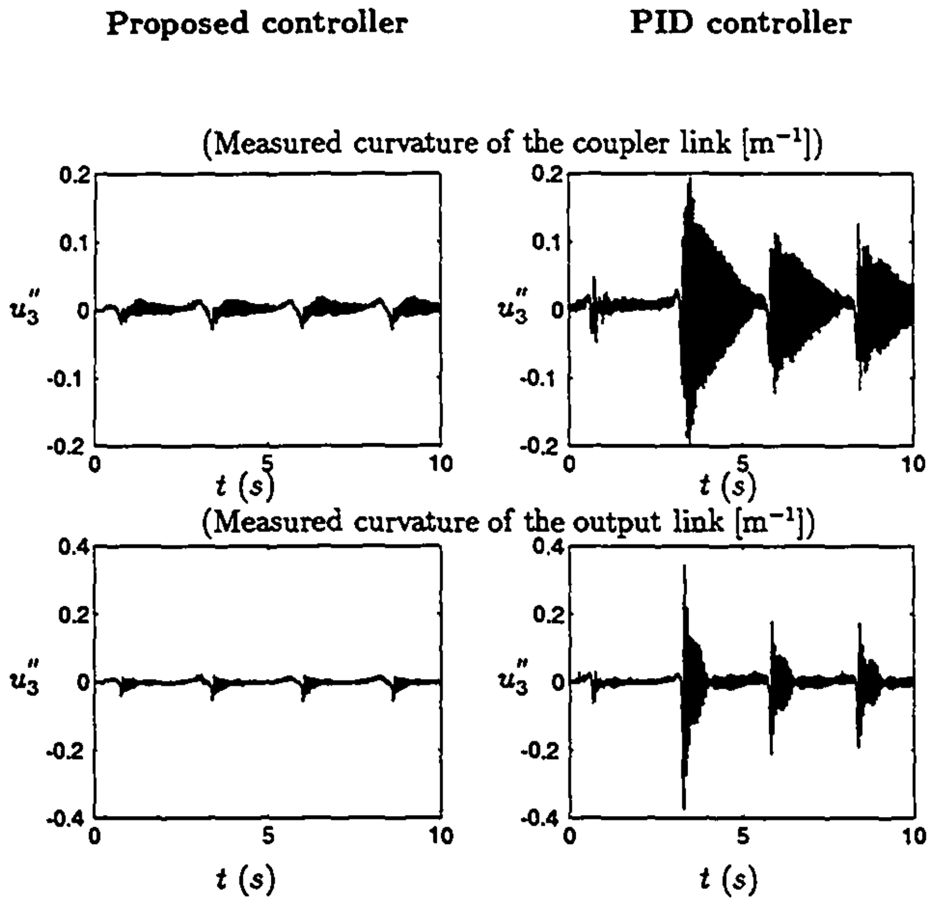

Figure 7.15: Comparison between the results obtained using the proposed and the PID controllers (Sub-plots in the left-hand side column are the link deflections obtained using the proposed control scheme, while sub-plots in the right-hand side column are those obtained using the PID controller)

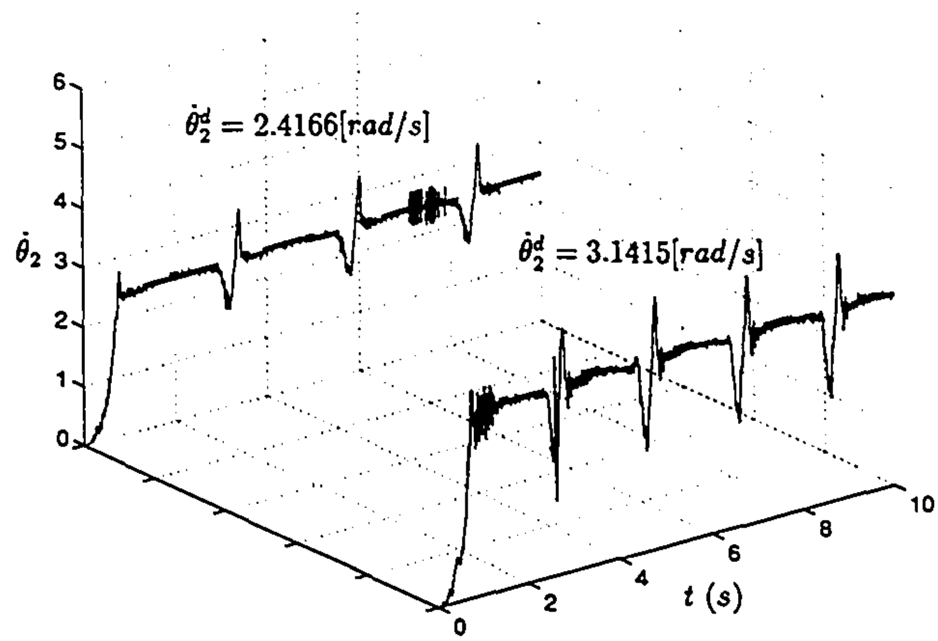

Figure 7.16: Angular speeds of the input link under different operating speeds

7.5.3 Discussions of the Experimental Results

Flexible Four-Bar Mechanism

The singular configurations coupled with the rapid inertia changes affect the system dynamics greatly. It is thus necessary to consider the consequences at the design stage of the control scheme. This can be achieved through an interactive study connecting the simulation and experimental results. For example, the angular speed of the input link, in the neighbourhood of the singular configuration and consecutive rapid inertia change, can be ameliorated by virtue of simulation and experiment.

Since the effects of the singular configurations and inertia changes appear in the form of doublet-type disturbances, we focus on the capability of attenuating these disturbance in designing the LQG compensator. In simulation, the disturbances that appear on the angular speed of the input link can be reduced by varying the associated penalizing factors in the weighting matrices. These simulation results are then compared with the experimental results. This interaction continues until satisfactory results are achieved.

However, such disturbances cannot be reduced as much as those anticipated in the simulation (Fig. 7.5). The experimental results reveal that these disturbances are always accompanied by sudden changes in the actual torque profile (Fig. 7.4). It should be recognized that such regions are vulnerable to the hysteresis of the DC motor because the direction of the torque changes rapidly. Moreover, the friction that acts on the gear-train of the DC motor becomes most active during these transients.

Although exact matches between the simulation and the experiment are not achieved, the proposed control scheme in fact does trajectory tracking while rejecting the disturbances. Moreover, the transverse vibrations of the flexible members are successfully suppressed by virtue of the proposed control scheme. It can be observed that the presence of periodic disturbance not only distorts rigid-body responses such as joint variables, but also excites the higher modes of the flexible links (Figs. 7.6 and 7.7). Hence, the resulting vibration signals—curvatures measured at the midspan of the coupler and output links—are much noisier than the simulation results. Yet they are not visible due to their small amplitudes. Given the desired angular speed of the input link (2.4166 [rad/s]), the mechanism behaves like a rigid-body system. Almost no vibrations can be seen.

The proposed controller is very successful in dealing with these noisy signals even without low-pass filters. This implies that the couplings between the rigid-body and elastic motions are well considered in the model. Furthermore, the nonlinearity arising from the kinematic coupling between the consecutive links and constraint due to loop closing can be effectively managed by the use of the NOC filter in real-time.

Taken as a whole, the two control objectives, i.e., trajectory tracking and suppression of vibrations, are successfully achieved using the proposed control scheme, which

Table 7.2: Material specification of the beam used in experiments

number of nodal points(n)	5
material	Aluminum
mass density (kg/m^3)	2712
Young's modulus (GPa)	71.0
length (m)	1
thickness of the beam (m)	0.003
cross-sectional area (m^2)	0.0762×0.0032
moment of inertia of the hub I_h (kg-m^2)	
moment of inertia of the unflexed rigid beam I_b (kg-m^2)	0.2232
structural damping coefficient	0.0095

is thus shown to be suitable for real-time control.

Rotating Flexible Beam

The experimental validation for the control of the rotating flexible beam whose material specifications are given in Table 7.2, has been completed by the application of a cubic spline modelling technique and an optimal control strategy (Figs. 7.8, 7.9 and 7.10). Using the Kalman filter, an investigation has also been conducted to assess the feasibility of using a reduced number of measurements at selected nodal points. The experimental results show that by taking only one strain measurement and a hub rotational angle measurement, the transverse vibrations can be suppressed and the end-tip can be made to follow a prescribed trajectory. In other words, the dynamic model based on cubic splines is completely observable and controllable (Cho, Angeles and Hori, 1991).

Chapter 8

Conclusions and Suggestions for Further Research

8.1 Conclusions

Two techniques have been integrated to obtain the equations of motion for a planar mechanism with a chain of flexible elements, namely, the natural orthogonal complement (NOC) coupled with Lagrange's equations and the cubic-spline discretization of the flexible elements, modelled as linearly elastic beams. The former allows the dynamic equations of the mechanical system to be formulated free of constraint forces, while the latter allows the elastic motions associated with structural members to be described with a finite number of generalized coordinates. The advantages thus offered can be summarized as follows:

- the mutual influence between the rigid-body motion and the elastic motion is considered in the kinematic and dynamic formulations.
- the minimal set of generalized coordinates, whose number is identical to the degree of freedom of the mechanism, is used in the dynamic formulation.
- the constraints are naturally incorporated into the equations of motion.

- the nonworking constraint forces thus introduced are eliminated by virtue of the NOC.
- the use of cubic splines allows a definition of the state-variable vector as the set of curvature values at the supporting points of the spline and their time-rates of change.

Taking a rotating flexible beam as an example, the mathematical models obtained using two different spatial discretization methods have been compared in terms of the robustness associated with the LQG compensator. The sensitivity to observation noise signals has been derived to study the observation spillover due to unmodelled residuals. Employing the stabilizing property of the LQ state feedback, the admissible bound on the stability margin due to modelling errors has been measured by varying the weighting matrices in the quadratic performance index. The compensator based on the cubic-spline model provided the following advantages over the normal-mode model in terms of sensitivity reduction and the robustness to nonlinear perturbations:

- lower sensitivity in a region around natural frequencies, when the same weighting matrices are selected
- use of a relatively lower feedback gain to obtain the same sensitivity
- better robustness in the presence of nonlinear perturbations.

In addition, Nyquist plots of the closed-loop transfer functions have been used to show that the cubic-spline model gives rise to the frequency response similar to a family of third-order systems, while that obtained using the normal-mode approach more closely resembles a higher-order oscillatory system. This implies that the closed-loop system for the cubic-spline case is in fact more robust with respect to higher-frequency uncertainties. It has been verified that the model obtained using the cubic-spline technique provides good stability properties against observation and control spillovers and is thus more amenable to an optimal control scheme, compared to the one using the normal-mode approach.

For the control of the four-bar flexible mechanism, a model-based control algorithm was proposed. This control algorithm consists of two parts, namely, the decoupling of the nonlinear equations of motion and the filtering of nonworking constraint forces. The former was achieved using the decoupled equations of motion, expressed in terms of extended generalized coordinates with which the motion of each separate link is defined. The latter was accomplished using the fact that the constraint forces thus introduced indeed lie in the nullspace of the transpose of the NOC. It should be noted that the NOC can be readily extracted from the reciprocity relationship between the independent generalized speeds and the constraint forces. This model-based control algorithm corresponds to those used in industrial robots, where each joint is controlled individually.

The discrete-time realization of the control scheme was achieved using the Euler operator, which is known to be numerically more robust than the shift operator. When using the Euler operator, the close connections between the continuous- and discrete-time results were established, i.e., the discrete-time results converge to the continuous-time counterparts as the sampling rate increases. Such connections found to be significant in the digital implementation of the NOC filter that rejects the constraint forces and, hence, obtains the applied torques. This is so because the performance of the continuous-time control system, i.e., prerequisite for the use of the NOC as a filter, can be ensured while using the discrete-time control system, which is unlikely the case when using the shift operator. Experimental studies were focused on the on-line capability of the NOC filter and showed a good performance with a relatively high sampling rate of 200 Hz. Moreover, bounds for the nonlinear perturbations were formulated in an effort to quantitatively measure the robustness of the discrete-time LQ state feedback associated with both the Euler and the shift operators. Simulations for the rotating flexible beam showed that the feedback obtained using the Euler operator is more robust against nonlinear perturbations.

The proposed control algorithm has been implemented on the prototype mechanism using strain gauges to identify the elastic motions of its flexible members, and the joint angle and its time-rate of change to infer the rigid-body motion. The control signal was then applied through the DC motor attached to the base joint. These studies have focused on the capability of two aspects of the control scheme: trajectory tracking and suppression of the vibration. Moreover, the effects of the singularities and the rapid inertia changes have been investigated in anticipation of exciting higher modes in flexible structures. Results showed that the proposed control scheme provides successful trajectory tracking while suppressing the vibration triggered by the doublet-type of disturbance. This disturbance is induced by the singularities of the mechanism coupled with the rapid inertia changes. It should be emphasised that the underlying control objectives were achieved even without using low-pass filters. This indicates that the proposed control scheme is robust against the control and observation spillovers.

8.2 Future Work

An imminent future work may be the design of a collocated control unit, consisting of an actuator and a sensor, both located at the same place, to achieve an active suppression of the structural vibration. The term "active" implies the structural vibration can be suppressed not by the external forces applied through the rigid-body motion, but by the forces supplied by a set of actuators distributed along the span of the structural member. For instance, piezoceramic strain actuators can be used in such a design, while the vibration can be directly measured with strain gauges at which control forces are applied (Fig. 8.1).

From this standpoint, cubic splines are a good candidate for a discrete model of the flexible structure. When using cubic splines, the set of state variables associated with the elastic motion is defined in terms of curvatures which are directly taken from the supporting points of the cubic splines. In fact, these quantities can be measured

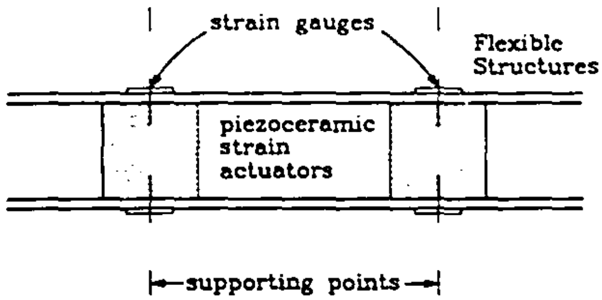

Figure 8.1: Conceptual design of a collocated control unit

with strain gauges and then used to obtain the counteracting forces, which are, in turn, proportional to the said strains. The practical gains thus obtained are not only the active suppression of the structural vibration, but also the increased bandwidth of the control system, which would be significantly limited when using noncollocated control.

Moreover, the proposed control scheme needs to be expanded to cover a general flexible spatial mechanical system possessing possibly several kinematic loops. This is because the decoupling of the nonlinear equations of motion is not so obvious as in the case of a planar mechanism. The Coriolis terms in the unconstrained equation of motion do not vanish in the spatial case, as they do in the planar case. The most promising results are expected using the computed-torque approach in conjunction with the NOC, so that the adaptation algorithm can be concentrated on the unknown terms associated with the said Coriolis terms.

Similarly, a hybrid control scheme can be used to substitute a computationally expensive computed-torque approach for spatial mechanical systems. As the name implies, this control system comprises two controllers, namely, position feedback for required rigid-body motions, and collocated control for active suppression of the structural vibrations. Since the latter provides self-suppression of the structural vibrations, trajectory tracking can be obtained using position feedback with, for instance, PD and PID controllers.

References

Amirouche, F. M. L., Jia, T. , and Ider, S. K., 1988, "Recursive Householder Transformation for Complex Dynamical Systems with Constraints", *ASME Journal of Applied Mechanics*, Vol. 55, No. 3, pp. 729–734.

Anderson, B. D. O. and Moore, J. B., 1971, *Linear Optimal Control*, Prentice-Hall, Inc., Englewood Cliffs.

Angeles, J. and Lee, S. K., 1988, "The Formulation of Dynamical Equations of Holonomic Mechanical Systems Using a Natural Orthogonal Complement", *ASME Journal of Applied Mechanics*, Vol. 55, pp. 243–244.

Angeles, J. and Lee, S. K., 1989, "The Modelling of Holonomic Mechanical Systems Using a Natural Orthogonal Complement", *Transactions of the CSME*, Vol. 13, No. 4, pp. 81–90.

Åström, K. J. and Wittenmark, B., 1990, *Computer-Controlled Systems*, Prentice-Hall, Inc., Englewood Cliffs.

Athans, M., 1971, "The Role and Use of the Stochastic Linear-Quadratic-Gaussian Problem in Control System Design", *IEEE Transactions on Automatic Control*, Vol. AC-16, No. 6, pp. 529–552.

Bahgat, B. M. and Willmert, K. D., 1976, "Finite Element Vibrational Analysis of Planar Mechanisms", *Mechanism and Machine Theory*, Vol. 11, pp. 47–71.

Balas, M. J., 1982, "Trends in Large Space Structure Control Theory: Fondest Hopes, Wildest Dreams", *IEEE Transactions on Automatic Control*, Vol. AC-27, No. 3, pp. 522–535.

Bélanger, P. R., 1990, *Control Systems I. Course Notes*, McGill University, Montréal, Canada.

Bayo, E., 1987, " A Finite-Element Approach to Control the End-Point Motion of a Single-Link Flexible Robot", *Journal of Robotic Systems*, Vol. 4, No. 1, pp. 63–75.

Bayo, E. and Serna, M. A., 1989, "Penalty Formulations for the Dynamics Analysis of Elastic Mechanisms", *ASME Journal of Mechanisms, Transmissions, and Automation in Design*, Vol. 111, pp. 321–327.

Book, W. J and Majette, M., 1983, "Controller Design for Flexible, Distributed Parameter Mechanical Arms Via Combined State Space and Frequency Domain Techniques", *ASME Journal of Dynamic Systems, Measurement, and Control*, Vol. 105, No. 4, pp. 245–254.

Brogan, W. L., 1991, *Modern Control Theory*, Prentice-Hall, Inc., Englewood Cliffs.

Bryson, A. E. and Ho, Y.-C., 1975, *Applied Optimal Control*, Hemisphere Publishing Co., New York.

Cannon, R. H. and Schmitz, E., 1984, "Initial Experiments on the End-Point Control of a Flexible One-Link Robot", *The International Journal cf a Robotics Research*, Vol. 3, No. 3, pp. 62–75.

Carusone, J. and D'Eleuterio, G. M. T., 1993, "Tracking Control for End-Effector Position and Orientation of Structurally Flexible Manipulators", *Journal of Robotic Systems*, Vol. 10, No. 6, pp. 847–870.

Carusone, J. and D'Eleuterio, G. M. T., 1993, "Experiments in End-Effector Tracking Control for Structurally Flexible Space Manipulators", *IEEE Transactions on Robotics and Automation*, Vol. 9, No. 5, pp. 553–560.

Chang, L.-W. and Hamilton, J. F., 1991, "Dynamics of Robotic Manipulators With

Flexible Links", *ASME Journal of Dynamic Systems, Measurement, and Control*, Vol. 113, No. 1, pp. 54–59.

Chen, C.-T., 1984, *Linear System Theory and Design*, Halt, Rinehart and Winston, Inc. New York.

Chen, C. and Zheng, Y. F., 1992, "Deformation Identification and Estimation of One-Dimensional Objects by Vision Sensors", *Journal of Robotic Systems*, Vol. 9, No. 5, pp. 595–612.

Cho, K. S., Angeles J. and Hori, N., 1991, "On the Controllability and Observability of Flexible Beams Under Rigid-Body Motions", *IECON' 91*, pp. 455–460, Kobe, Japan.

Cho, K. S., Angeles, J. and Hori, N., 1994, "A Robust Model for the Discretization of Flexible Links Based on Cubic Splines", *IUTAM Symposium on The Active Control of Vibration*, Bath, UK, pp. 225–232.

Cetinkunt, S. and Yu, W.-L., 1992, "Accuracy of Finite Dimensional Dynamic Models of Flexible Manipulators for Controller Design", *Journal of Robotic Systems*, Vol. 9, No. 3, pp. 327–350.

Comeau, A. R. and Hori, N., 1992, "Numerical Properties of the Euler Operator in Digital Control", *Industrial Automation Conference*, Montreal, Canada, pp. 27.9–27.13.

Craig, J. J., Hsu, P. and Sastry, S. S., 1986, "Adaptive Control of Mechanical Manipulators", *IEEE Int. Conf. on Robotics and Automation*, San Francisco, California, pp. 190–195.

Cyril, X., 1988, *Dynamics of Flexible-Link Manipulators*, Ph.D. dissertation, McGill University, Montréal, Canada.

Cyril, X., Angeles, J. and Misra, A. K., 1991, "Dynamics of Flexible Multibody Mechanical Systems", *Transactions of the CSME*, Vol. 15, No. 3, pp. 235–256.

Dancose, S., Angeles, J. and Hori, N., 1989, "Optimal vibration control of a rotating flexible beam", *ASME conference on Diagnostics, Vehicle Dynamics and Special Topics*, Montréal, Canada, pp. 259–264.

Darcovich, J., Angeles, J. and Misra, A. K., 1992, "Dynamics of single-loop mechanisms with flexible links", *Machine Vibration*, Vol. 1, No. 3. pp. 155–163.

Dierckx, P., 1993, *Curve and Surface Fitting with Splines*, Clarendon Press, Oxford-New York-Tokyo.

Doyle, J. C. and Stein, G., 1981, "Multivariable Feedback Design: Concepts for a Classical/Modern Synthesis", *IEEE Transactions on Automatic Control*, Vol. AC-26, No. 1, pp. 4–16.

D'Souza, A. K. and Garg, V. K., 1984, *Advanced Dynamics. Modeling and Analysis*, Prentice-Hall, Inc., Englewood Cliffs.

Franklin G. F. Powell J. D., and Workman M. L., 1990, *Digital Control of Dynamic Systems*, Addison-Wesley, Reading, Massachusetts.

Gear, W. C., 1971, *Numerical Initial Value Problems in Ordinary Differential Equations*, Prentice-Hall, Inc., Englewood Cliffs.

Giovagnoni, M., 1994, "A Numerical and Experimental Analysis of a Chain of Flexible Bodies", *ASME Journal of Dynamic Systems, Measurement, and Control*, Vol. 116, pp. 73–80.

Giovagnoni, M. and Rossi, A., 1989, "Transient Analysis of a Flexible Crank", *Mechanism Machine Theory*, Vol. 24, No. 4, pp. 231–243.

Gibson, J. S. and Adamian A., 1991, "Approximation Theory for Linear-Quadratic-Gaussian Optimal Control of Flexible Structure", *SIAM Journal of Control and Optimization*, Vol. 29, No. 1, pp. 1–37.

Gosselin, C. and Angeles, J., 1990, "Singularity Analysis of Closed-Loop Kinematic Chains", *IEEE Transactions on Robotics and Automation*, Vol. 6, No. 3, pp. 281–290.

Hori, N., Mori, T. and Nikiforuk, P. N., 1994, "Discrete-Time Models of Continuous-Time Systems", *Control and Dynamic Systems*, Vol. 66, pp. 1–45.

Hori, N., Nikiforuk, P. N. and Kanai, K., 1988, "On a Discrete-Time System Expressed in the Euler Operator", *Proc. of American Control Conference*, Atlanta, GA, pp. 873–878.

Hughes, P. C., 1980, "Model Identities for Elastic Bodies, With Application to Vehicle Dynamics and Control" *ASME Journal of Applied Mechanics*, Vol. 47, No. 1, pp. 177–184.

Hughes, P. C., 1987, "Space Structure Vibration Modes: How Many Exist? Which Ones Are Important?" *IEEE Control Systems Magazine*, Vol. 7, No. 1, pp. 22–28.

Ider, S. K. and Amirouche, F. M. L., 1988, "Coordinate Reduction in the Dynamics of Constrained Multibody Systems–A New Approach", *ASME Journal of Applied Mechanics*, Vol. 55, No. 4, pp. 899–904.

Kalman, R. E., 1964, "When Is a Linear Control System Optimal?", *Journal of Basic Engineering*, Vol. 86, pp. 51–60.

Kane, T. R., Ryan, R. R. and Banerjee, A. K., 1987, "Dynamics of a Cantilever Beam Attached to a Moving Base", *Journal of Guidance, Control and Dynamics*, Vol. 10, No. 2, pp. 139–151.

Li, G. and Gevers, M., 1993, "Comparative Study of Finite Wordlength Effects in Shift and Delta Operator Parameterization", *IEEE Transactions on Automatic Control*, Vol. AC-38, No. 5, pp. 803–807.

Meirovitch, L., 1967, *Analytical Methods in Vibrations*, The Macmillan Company, New York.

Middleton, R. H. and Goodwin, G. C., 1986, "Improved Finite Word Length Characteristics in Digital Control Using Delta Operators", *IEEE Transactions on Automatic Control*, Vol. AC-31, No. 11, pp. 1015–1021.

Middleton, R. H. and Goodwin, G. C., 1988, "Adaptive Computed Torque Control for Rigid Link Manipulators", *Syst. Control Lett.*, Vol. 10, pp. 9–16.

Middleton, R. H. and Goodwin, G. C., 1990, *Digital Control and Estimation. A Unified Approach*, Prentice Hall, New Jersey.

Midha, A., Erdman, A. G. and Frohrib, D. A., 1977, "An Approximate Method for the Dynamic Analysis of Elastic Linkages", *ASME Journal of Engineering for Industry*, Vol. 99, No. 2, pp. 449–455.

Naganathan, G. and Soni, A. H., 1988, "Nonlinear Modeling of Kinematic and Flexibility Effects in Manipulator Design", *ASME Journal of Mechanisms, Transmissions, and Automation in Design*, Vol. 110, pp. 243–254.

Nagarajan, S. and Turcic, D. A., 1990, "Lagrangian Formulation of the Equations of Motion for Elastic Mechanisms With Mutual Dependence Between Rigid Body and Elastic Motions. Part I: Element Level Equations", *ASME Journal of Dynamic Systems, Measurement, and Control*, Vol. 112, No. 2, pp. 203–214.

Nagarajan, S. and Turcic, D. A., 1990, "Lagrangian Formulation of the Equations of Motion for Elastic Mechanisms With Mutual Dependence Between Rigid Body and Elastic Motions. Part II: System Equations", *ASME Journal of Dynamic Systems, Measurement, and Control*, Vol. 112, No. 2, pp. 215–224.

Ortega, R. and Spong, M. W., 1989, "Adaptive Motion Control of Rigid Robots: a Tutorial", *Automatica*, Vol. 25, No. 6, pp. 877–888.

Patel, R. V., Toda, M. and Shidhar, B., 1977, "Robustness of Linear Quadratic State Feedback Designs in the Presence of System Uncertainty", *IEEE Transactions on Automatic Control*, Vol. AC-22, No. 6, pp. 945–949.

Perkins, W. R. and Cruz, J. B., 1965, "Feedback Properties of Linear Regulators, 1971, *IEEE Transactions on Automatic Control*, Vol. AC-16, No. 6, pp. 659–663.

Powell, J. D. and Katz, P., 1975, "Sample Rate Selection for Aircraft Digital Control", *AIAA Journal*, Vol. 13, No. 8, pp. 975–979.

Rogers, D. F. and Adams, J. A., 1976, *Mathematical Elements for Computer Graphics*, McGraw-Hill Inc., New York.

Sadler, J. P., and Sandor, G., N., 1973, "A Lumped Parameter Approach to Vibration and Stress Analysis of Elastic Linkages", *ASME Journal of Engineering for Industry*, Vol. 95, No. 2, pp. 549–556.

Saha, S. K. and Angeles, J., 1991, "The Formulation of Kinematic Constraints in Design-Oriented Machine Dynamics", *Proc. 1991 ASME Design Automation Conference. Advances in Design Automation*, Sept. 22–25, Miami, Vol. 2, pp. 115–122.

Salgado, M., Middleton, R. and Goodwin, G. C., 1988, "Connection Between Continuous and Discrete Riccati Equations with Applications to Kalman Filtering", *IEE Proceedings, Pt. D*, Vol. 135, No. 1, pp. 28–34.

Sakawa, Y., Matsuno, F., and Fukushima, S., 1985, "Modeling and Feedback Control of Flexible Arm", *Journal of Robotics System*, Vol. 2, No. 4, pp. 453–472.

Shabana, A. and Wehage, R. A., 1983, "Variable Degree-of-Freedom Component Mode Analysis of Inertia Variant Flexible Mechanical Systems", *ASME Journal of Mechanisms, Transmissions, and Automation in Design*, Vol. 105, No. 3, pp. 371–378.

Shamma, J. S. and Athans, M., 1992, "Gain Scheduling: Potential Hazards and Possible Remedies", *IEEE Control Systems Magazine*, Vol. 12, No. 3, pp. 101–107.

Singh, R. P. and Likins, P. W., 1985, "Singular Value Decomposition for Constrained Dynamical Systems", *ASME Journal of Applied Mechanics*, Vol. 52, No. 4, pp. 943–948.

Song, J. O. and Haug, E. J., 1980, "Dynamic Analysis of Planar Flexible Mechanisms", *Computer Methods in Applied Mechanics and Engineering*, Vol. 24, pp. 359–381.

Spong, M. W. and Ortega, R., 1990, "On Adaptive Inverse Dynamics Control of Rigid Robots", *IEEE Transactions on Automatic Control*, Vol. AC-35, No.1, pp. 92–95.

Strang, G., 1986, *Introduction to Applied Mathematics*, Wellesley-Cambridge Press, Massachusetts.

Timoshenko, S. and Young, D. H., 1955, *Vibration Problems in Engineering*, D. Van Nostrand Co., Princeton.

Turcic, D. A. and Midha, A., 1984, "Dynamic Analysis of Elastic Mechanism Systems. Part II: Experimental Results", *ASME Journal of Dynamic Systems, Measurement, and Control*, Vol. 106, pp. 255–260.

Van Loan, C. F., 1978, "Computing Integrals Involving the Matrix Exponential", *IEEE Transactions on Automatic Control*, Vol. AC–23, No. 3, pp. 395–405.

Vidyasagar, M., 1993, *Nonlinear Systems Analysis*, Prentice-Hall, Inc., Englewood Cliffs.

Wang D. and Vidyasagar, M., 1992, "Passive Control of a Stiff Flexible Link", *The International Journal of Robotics Research*, Vol. 11, No. 6, pp. 572–578.

Appendix A

Proof of Theorem 5.1

The bound for the nonlinear perturbations that guarantees stability of the closed-loop system can be obtained by considering a suitable Lyapunov function, namely,

$$V(\mathbf{x}) = \mathbf{x}^T \mathbf{S} \mathbf{x} \tag{A.1}$$

where $\mathbf{S}$ is the solution of eq.(5.25).

The time-rate of change is then given by

$$\dot{V}(\mathbf{x}) = \dot{\mathbf{x}}^T \mathbf{S} \mathbf{x} + \mathbf{x}^T \mathbf{S} \dot{\mathbf{x}} \tag{A.2}$$

Using eq.(5.21), the above expression becomes

$$\begin{aligned} \dot{V}(\mathbf{x}) &= \mathbf{x}^T \left(\mathbf{A}_c^T \mathbf{S} + \mathbf{S} \mathbf{A}_c \right) + 2\mathbf{g}^T \mathbf{S} \mathbf{x} & \text{(A.3)} \\ &= \mathbf{x}^T \left(\mathbf{A}^T \mathbf{S} + \mathbf{S} \mathbf{A} - \frac{1}{r} \mathbf{S} \mathbf{b} \mathbf{b}^T \mathbf{S} + \mathbf{Q} \right) \mathbf{x} & \text{(A.4)} \\ &\quad - \mathbf{x}^T \left(\mathbf{Q} + \frac{1}{r} \mathbf{S} \mathbf{b} \mathbf{b}^T \mathbf{S} \right) \mathbf{x} + 2\mathbf{g}^T \mathbf{S} \mathbf{x} \end{aligned}$$

Since the first quadratic form becomes zero by virtue of eq.(5.25), we obtain the following Lyapunov equation

$$\mathbf{A}_c^T \mathbf{S} + \mathbf{S} \mathbf{A}_c = -\mathbf{D} \tag{A.5}$$

where

$$\mathbf{D} = \mathbf{Q} + \frac{1}{r} \mathbf{S} \mathbf{b} \mathbf{b}^T \mathbf{S} \tag{A.6}$$

It should be noted that $\mathbf{D}$ is positive-definite due to the stabilizing characteristic of the LQ state feedback. Moreover, $\mathbf{S}$ is symmetric and positive-definite when $\mathbf{D}$ is symmetric and positive-definite, provided that $\mathbf{A}_c$ is asymptotically stable (Brogan, 1991). Then, the time derivative of eq.(A.1) becomes

$$\dot{V}(\mathbf{x}) = -\mathbf{x}^T\mathbf{D}\mathbf{x} + 2\mathbf{g}^T\mathbf{S}\mathbf{x} \tag{A.7}$$

If the closed-loop system is stable, $\dot{V}$ must be negative definite, which requires that

$$\dot{V} = -\mathbf{x}^T\mathbf{D}\mathbf{x} + 2\mathbf{g}^T\mathbf{S}\mathbf{x} < 0, \quad \forall \mathbf{x} \neq \mathbf{0} \tag{A.8}$$

For the preceding inequality to hold, the following condition has to be met,

$$\max_{\mathbf{g},\mathbf{x}\in R^{2n}} |\mathbf{g}^T\mathbf{S}\mathbf{x}| < \frac{1}{2} \min_{\mathbf{x}\in R^{2n}} (\mathbf{x}^T\mathbf{D}\mathbf{x}) \tag{A.9}$$

The left hand side of eq.(A.9) leads to

$$\begin{aligned} \max_{\mathbf{g},\mathbf{x}\in R^{2n}} |\mathbf{g}^T\mathbf{S}\mathbf{x}| &\leq \|\mathbf{g}\| \; \|\mathbf{S}\mathbf{x}\| \\ &\leq \|\mathbf{g}\| \; \|\mathbf{S}\|_s \|\mathbf{x}\| = \sigma_{\max}(\mathbf{S})\|\mathbf{g}\| \; \|\mathbf{x}\| \end{aligned} \tag{A.10}$$

where $\|\cdot\|_s$ denotes the matrix spectral norm, defined as

$$\|\mathbf{S}\|_s = \sigma_{\max}(\mathbf{S}) \tag{A.11}$$

and $\sigma_{\max}(\mathbf{S})$ is the largest singular value of $\mathbf{S}$. Consequently, eq.(A.10) becomes

$$\max_{\mathbf{g},\mathbf{x}\in R^{2n}} |\mathbf{g}^T\mathbf{S}\mathbf{x}| \leq \sigma_{\max}(\mathbf{S})\|\mathbf{g}\| \; \|\mathbf{x}\| \tag{A.12}$$

Moreover, the right-hand-side of eq.(A.9) satisfies

$$\min_{\mathbf{x}\in R^{2n}} (\mathbf{x}^T\mathbf{D}\mathbf{x}) \geq \sigma_{\min}(\mathbf{D})\|\mathbf{x}\|^2 \tag{A.13}$$

since $\mathbf{D}$ is symmetric positive definite (Chen, 1984), namely,

$$\sigma_{\min}(\mathbf{D})\|\mathbf{x}\|^2 \leq \mathbf{x}^T\mathbf{D}\mathbf{x} \leq \sigma_{\max}(\mathbf{D})\|\mathbf{x}\|^2 \tag{A.14}$$

where $\sigma_{\min}(\cdot)$ and $\sigma_{\max}(\cdot)$ denote the smallest and the largest singular values of $\mathbf{D}$, respectively.

Summing eqs.(A.10) and (A.13) leads to the bound for the nonlinear perturbation function $\mathbf{g}(\mathbf{x})$ such that the closed-loop system of eq. (5.21) remains stable in the presence of nonlinear perturbations, namely,

$$\frac{\|\mathbf{g}(\mathbf{x})\|}{\|\mathbf{x}\|} < \zeta \equiv \frac{\sigma_{\min}\mathbf{D}}{2\sigma_{\max}(\mathbf{S})} = \frac{1}{2\|\mathbf{D}^{-1}\|_s\|\mathbf{S}\|_s} \tag{A.15}$$

Appendix B

Proof of Theorem 6.1

The theorem can be proved by defining

$$V(\mathbf{x}(k)) = \mathbf{x}^T \mathbf{S}_q \mathbf{x} \tag{B.1}$$

where $\mathbf{S}_q$ is the solution of eq.(6.36). Taking the difference of the foregoing Lyapunov function produces

$$\Delta V = V(\mathbf{x}(k+1)) - V(\mathbf{x}(k)) \tag{B.2}$$

Substitution of eq.(6.25) into eq.(B.2) leads to

$$\begin{aligned} \Delta V &= \mathbf{x}^T \left(\mathbf{\Phi}_q^T \mathbf{S}_q \mathbf{\Phi}_q - \mathbf{S}_q \right) \mathbf{x}^T + 2\mathbf{g}^T \mathbf{\Phi}_q \mathbf{x} + \mathbf{g}^T \mathbf{S}_q \mathbf{g}_q \\ &= -\mathbf{x}^T \mathbf{D}_q \mathbf{x} + 2\mathbf{g}^T \mathbf{S}_q \mathbf{\Phi}_q \mathbf{x} + \mathbf{g}^T \mathbf{S}_q \mathbf{g} \end{aligned} \tag{B.3}$$

where

$$\mathbf{\Phi}_q^T \mathbf{S}_q \mathbf{\Phi}_q - \mathbf{S}_q = -\mathbf{D}_q \tag{B.4}$$

Moreover, $\mathbf{D}_q$ is positive-definite due to the stabilizing characteristic of the LQ state feedback. It should be realized that eq.(B.4), for the given positive-definite $\mathbf{D}_q$, has a unique solution for $\mathbf{S}_q$ and this $\mathbf{S}_q$ is positive definite, provided that the closed-loop system is asymptotically stable (Vidyasagar, 1993).

The stability condition of the closed-loop system requires

$$\Delta V = -\mathbf{x}^T\mathbf{D}_q\mathbf{x} + 2\mathbf{g}^T\mathbf{S}_q\mathbf{\Phi}_q\mathbf{x} + \mathbf{g}^T\mathbf{S}_q\mathbf{g} < 0, \quad (\forall \mathbf{x} \neq \mathbf{0}) \tag{B.5}$$

To satisfy the foregoing inequality, the following condition has to be met:

$$\max_{\mathbf{g},\mathbf{x}\in R^{2n}} |2\mathbf{g}^T\mathbf{S}_q\mathbf{\Phi}_q\mathbf{x} + \mathbf{g}^T\mathbf{S}_q\mathbf{g}| < \min_{\mathbf{x}\in R^{2n}} \left(\mathbf{x}^T\mathbf{D}_q\mathbf{x}\right) \tag{B.6}$$

From the left-hand side of eq.(B.6),

$$\begin{aligned}\max_{\mathbf{g},\mathbf{x}\in R^{2n}} |2\mathbf{g}^T\mathbf{S}_q\mathbf{\Phi}_q\mathbf{x} + \mathbf{g}^T\mathbf{S}_q\mathbf{g}| &\leq 2\|\mathbf{g}^T\|\ \|\mathbf{S}_q\|\ \|\mathbf{\Phi}_q\mathbf{x}\| + \mathbf{g}^T\mathbf{S}_q\mathbf{g} \\ &\leq 2\|\mathbf{g}^T\|\ \|\mathbf{S}_q\|_s\|\mathbf{\Phi}_q\|_s\|\mathbf{x}\| + \sigma_{max}(\mathbf{S}_q)\|\mathbf{g}\|^2 \\ &\leq 2\sigma_{max}(\mathbf{S}_q)\|\mathbf{g}^T\|\ \|\mathbf{x}\| + \sigma_{max}(\mathbf{S}_q)\|\mathbf{g}\|^2\end{aligned} \tag{B.7}$$

The preceding derivation requires that all the eigenvalues of $\mathbf{\Phi}_q$ have a magnitude less than 1. This is true if the closed-loop system given in eq.(6.37) is stable. Hence, the largest eigenvalue of $\mathbf{\Phi}_q$, which is also the spectral norm of $\|\mathbf{\Phi}_q\|_s$, has magnitude less than 1.

In light of eq.(A.14), the right hand side of eq.(B.6) must hold, namely,

$$\min_{\mathbf{x}\in R^{2n}} \left(\mathbf{x}^T\mathbf{D}_q\mathbf{x}\right) \geq \sigma_{min}(\mathbf{D}_q)\|\mathbf{x}\|^2 \tag{B.8}$$

Assembling eq.(B.8) and eq.(B.8) leads to

$$\sigma_{max}(\mathbf{D}_q)\|\mathbf{g}\|^2 + 2\sigma_{max}(\mathbf{S}_q)\|\mathbf{g}^T\|\ \|\mathbf{x}\| - \sigma_{min}(\mathbf{S}_q)\|\mathbf{x}\|^2 < 0 \tag{B.9}$$

Since $\|\cdot\|$ is always greater than zero by definition, there is only one solution that satisfies eq.(B.9), namely,

$$\frac{\|\mathbf{g}(\mathbf{x})\|}{\|\mathbf{x}\|} < -1 + \sqrt{1+\kappa} \tag{B.10}$$

where

$$\kappa \equiv \frac{\sigma_{min}(\mathbf{D}_q)}{2\ \sigma_{max}(\mathbf{S}_q)} \tag{B.11}$$

Appendix C

Proof of Theorem 6.2

A Lyapunov function candidate is selected as

$$V = \mathbf{x}^T(k)\mathbf{S}_\epsilon\mathbf{x}(k) \tag{C.1}$$

where $\mathbf{S}_\epsilon$ is the solution of eq.(6.49). The difference rate of the Lyapunov function is performed using the Euler operator, i.e.,

$$\varepsilon V = \varepsilon\mathbf{x}^T\mathbf{S}_\epsilon\mathbf{x}(k) + \mathbf{x}^T(k)\mathbf{S}_\epsilon\varepsilon\mathbf{x}(k) + T\left(\varepsilon\mathbf{x}(k)\right)^T\left(\varepsilon\mathbf{x}(k)\right) \tag{C.2}$$

Upon substituting eq.(6.42) into the foregoing equation, we obtain

$$\varepsilon V = -\mathbf{x}^T\left(\mathbf{D}_\epsilon\right)\mathbf{x} + 2\mathbf{g}^T\mathbf{S}_\epsilon\left(\mathbf{1} + T\mathbf{\Phi}_\epsilon\right)\mathbf{x} + T\mathbf{g}^T\mathbf{S}_\epsilon\mathbf{g} \tag{C.3}$$

where

$$-\mathbf{D}_\epsilon \equiv \mathbf{\Phi}_\epsilon^T\mathbf{S}_\epsilon + \mathbf{S}_\epsilon\mathbf{\Phi}_\epsilon^T + T\mathbf{\Phi}_\epsilon^T\mathbf{S}_\epsilon\mathbf{\Phi}_\epsilon \tag{C.4}$$

Notice that $\mathbf{D}_\epsilon$ is positive-definite due to the stabilizing characteristic of the LQ state feedback. Moreover, there exists a unique solution for $\mathbf{S}_\epsilon$ which satisfies eq.(C.4). Furthermore, $\mathbf{S}_\epsilon$ is positive-definite if the closed-loop system given in eq.(6.42) is stable (Middleton and Goodwin, 1990).

For the nonlinear vector function $\mathbf{g}$, the bound that keeps the closed-loop system asymptotically stable, can then be obtained from the relation given below

$$\varepsilon V = -\mathbf{x}^T\mathbf{D}_\epsilon\mathbf{x} + 2\mathbf{g}\mathbf{S}_\epsilon\left(\mathbf{1} + T\mathbf{\Phi}_\epsilon\right)\mathbf{x} + T\mathbf{g}^T\mathbf{S}_\epsilon\mathbf{g} < 0 \tag{C.5}$$

Since $\mathbf{\Phi}_q = \mathbf{1} + T\mathbf{\Phi}_\epsilon$, it follows that

$$2\mathbf{g}\mathbf{S}_\epsilon\mathbf{\Phi}_q\mathbf{x} + T\mathbf{g}^T\mathbf{S}_\epsilon\mathbf{g} < \mathbf{x}^T\mathbf{D}_\epsilon\mathbf{x} \tag{C.6}$$

In order to satisfy the preceding equality, the following relation should be satisfied

$$\max_{\mathbf{g},\mathbf{x}\in R^{2n}} |2\mathbf{g}^T\mathbf{S}_\epsilon\mathbf{\Phi}_q\mathbf{x} + T\mathbf{g}^T\mathbf{S}_\epsilon\mathbf{g}| < \min_{\mathbf{x}\in R^{2n}} \left(\mathbf{x}^T\mathbf{D}_\epsilon\mathbf{x}\right) \tag{C.7}$$

Considering that eigenvalues of $\mathbf{\Phi}_q$ have magnitude less than unity, the left hand side of eq.(C.7) satisfies

$$\begin{aligned}\max_{\mathbf{g},\mathbf{x}\in R^{2n}} |2\mathbf{g}^T\mathbf{S}_\epsilon\mathbf{\Phi}_q\mathbf{x} + T\mathbf{g}^T\mathbf{S}_\epsilon\mathbf{g}| &\leq 2\|\mathbf{S}_\epsilon\|\ \|\mathbf{g}\|\ \|\mathbf{x}\| + T\mathbf{g}^T\mathbf{S}_\epsilon\mathbf{g} \\ &\leq 2\sigma_{max}(\mathbf{S}_\epsilon)\|\mathbf{g}\|\ \|\mathbf{x}\| + T\sigma_{max}(\mathbf{S}_\epsilon)\|\mathbf{g}\|^2\end{aligned} \tag{C.8}$$

Since $\mathbf{D}_\epsilon$ is symmetric and positive-definite, the right hand side of eq.(C.7) satisfies

$$\min_{\mathbf{x}\in R^{2n}} \left(\mathbf{x}^T\mathbf{D}_\epsilon\mathbf{x}\right) \geq \sigma_{min}(\mathbf{D}_\epsilon)\|\mathbf{x}\|^2 \tag{C.9}$$

Summing eq.(C.9) and eq.(C.9), we obtain

$$\|\mathbf{g}\|^2 + \frac{2}{T}\|\mathbf{x}\|\ \|\mathbf{g}\| - \frac{1}{T}\kappa\|\mathbf{x}\|^2 < 0 \tag{C.10}$$

where

$$\kappa \equiv \frac{\sigma_{min}(\mathbf{D}_\epsilon)}{\sigma_{max}(\mathbf{S}_\epsilon)} > 0 \tag{C.11}$$

Since $\|\mathbf{g}\| > 0$ if $\mathbf{g} \neq \mathbf{0}$, the bound on $\|\mathbf{g}\|$ that satisfies eq.(C.10) is obtained as

$$\frac{\|\mathbf{g}(\mathbf{x})\|}{\|\mathbf{x}\|} < \frac{1}{T}\left(-1 + \sqrt{(1+T\kappa)}\right) \tag{C.12}$$